

Copyright  
by  
Chang Min Jung  
2015

**The Dissertation Committee for Chang Min Jung Certifies that this is the approved version of the following dissertation:**

**Measurement of Fluid Properties in Organic-Rich Shales**

**Committee:**

---

Mukul M. Sharma, Supervisor

---

Martin E. Chenevert, Co- Supervisor

---

Eric van Oort

---

Matthew Balhoff

---

Chadi El Mohtar

**Measurement of Fluid Properties in Organic-Rich Shales**

**by**

**Chang Min Jung, B.S.; M.S.**

**Dissertation**

Presented to the Faculty of the Graduate School of

The University of Texas at Austin

in Partial Fulfillment

of the Requirements

for the Degree of

**Doctor of Philosophy**

**The University of Texas at Austin**

**December 2015**

## **Dedication**

To my grandmother for her inspiration and blessings.

To my parents for their prayer and support.

To my wife and daughter for their love and sacrifices.

## **Acknowledgements**

I would like to express my deepest gratitude to my supervising professor, Dr. Mukul Sharma for his continuous guidance and support throughout all these years. His effort with enthusiasm was great inspirations to me, and his experience and suggestion deepened my understanding on various aspects of petroleum engineering. It has been a great honor and truly enjoyable experience to work under his supervision. I also would like to acknowledge Dr. Martin E. Chenevert as my co-advisor for his warm-hearted guidance and sincere advice. His supervision over the last 5 years truly guided me to a right path, and encouraged me, especially during the difficult process of research. I acknowledge my deep appreciations to Dr. Eric van Oort, Dr. Matthew Balhoff, and Dr. Chadi El Mohtar for valuable advices, guidance, and serving as my committee members.

I am very grateful for being given the opportunity to study at the University of Texas at Austin and indebted to all those who have contributed to my development during my graduate study here. Administrative support from Jin Lee was essential to make all the work happen. Rod Russell offered great help for engineering knowledge and building the experimental setups and procuring equipment. The experimental support from Rui Zhang, Junhao Zhou and Peng Zhang were crucial for conducting experiments. I owe many thanks to the Department of Energy and RPSEA (Research Partnership to Secure Energy for America) for their financial support, as well as the numerous companies sponsoring the Joint Industry Project on Hydraulic Fracturing and Sand Control at UT Austin.

I would like to thank my colleagues in our research group who through their sincere suggestions and fruitful discussions shaped this dissertation in so many ways. In

particular, I would like to thank Ben, Weiwei, Pratik, Mac, JP, Evan, Kyunghaeng, Jongsoo, Dongkeun, Sahil, Hisanao, Amit, Ripu, Samarth, Karn including all who I have not mentioned here explicitly.

I also would like to thank all of my friends for making the journey enjoyable: Heesong, Dohoon, Doohyun, Hoonyoung, Hyungjoo, Hunjoo, Hojung, Kwangjin, Sanghyon, Sunghyun, Bongjun, Yongdo, Ijung, and Beomhee.

Finally, I want to thank my beloved wife, Ah Young Lee for her support and encouragement along this journey. All of my work would be impossible without her presence. My parents and parents-in-law were a real support, and my children, Claire and Heemang, were the pillar of hope for me. I really appreciate what I have received and I really enjoyed during my study at The University of Texas.

# **Measurement of Fluid Properties in Organic-Rich Shales**

Chang Min Jung, Ph.D.

The University of Texas at Austin, 2015

Supervisors: Mukul M. Sharma and Martin E. Chenevert

The primary objective of this study is to develop and improve water-based drilling fluids and fracturing fluids for organic rich shale reservoirs by using nanoparticles and to gain fundamental insight into water and oil flow in shales. This dissertation presents results for several shale formations in the US, namely the Barnett shale, the Eagle Ford shale, the Utica shale, and the Bakken shale. The research discussed here presents new methods for studying the interaction between various fluids and organic-rich shale and the development of proper methods to measure apparent and relative permeability of shale.

First of all, we show how the petrophysical properties of shales are changed when they are poorly preserved. Experiments were performed to measure important petrophysical properties such as porosity, density, weight change, hardness, wave velocity and permeability before and after shale samples dried-out. The large differences in shale properties between preserved and un-preserved samples as reported herein, clearly indicate that shales should be preserved at the well site and tested with a standard procedure ensuring minimum alteration of fluids from the shale. Failure to follow a standard procedure leads to measurements that do not reflect the “true” or in-situ properties of the shale. Instead, the measurements can be a factor of 2 or 3 different from the “true” value. The shale handling, preservation and measurement techniques and

procedures presented here can be used as a standard protocol for studying organic rich shales.

Next, we discuss how fracturing fluid can change the petrophysical properties of shale. Among the various petrophysical properties, the fluid permeability is chosen to determine the effect of the fracturing fluid on the shale. Experimental procedures are presented to suggest how to measure the shale permeability. To measure the fluid permeability, the Pressure Penetration Technique (PPT) was developed and used. The reference permeability with sea water brine was measured and then fracturing fluid was injected into the shale. The brine permeability was re-measured to see the effect of exposure to the fracturing fluid, and experimental data show the permeability change due to fracturing fluid plugging the shale.

Next, we focus on the development of a Water Based Mud (WBM) system for organic-rich shale. Drilling through a shale formation can result in borehole instability problems, and this is known to add substantial costs to the operation. This is because conventional drilling fluids tend to interact with clay minerals in shales, and the mechanical properties of rock are changed by clay swelling. To reduce the interaction between water-based muds and shales, we need to reduce water invasion into the shale. The addition of nanoparticle additives to water-based drilling fluids can significantly reduce the invasion. We report results for shale permeability and pressure penetration through shales using different fluids: brine, base mud and nanoparticle based muds. To better define the effect of nanoparticles, we used different concentrations of nanoparticles in the mud. From the large reduction in permeability and the pressure response results, we clearly show that nanoparticles act as good shale inhibitors to ensure wellbore stability during drilling.



Experimental studies used to measure the relative permeability of shale. Such measurements have never been done before. Due to the extremely low permeability of shale, it is very difficult to measure the relative permeability of shale directly. We propose a method of relative permeability measurement using NMR (Nuclear Magnetic Resonance) spectroscopy to measure fluid saturations and a RPC (relative permeability measurements under a confining pressure) set-up to conduct the displacement. RPC set-up is a newly developed forced injection set-up using the unsteady-state method. The in-situ fluid saturation was successfully measured with NMR, and the set-up was also useful for measuring the relative permeability of shale. It yielded continuous results from the Bakken shale tests.

## Table of Contents

List of Tables .....	xiii
List of Figures .....	xv
Chapter 1: Introduction .....	1
1.1 Introduction.....	1
1.2 Motivation for Research .....	9
1.2.1 Wellbore Instability and Petrophysical Properties of Shale .....	9
1.2.2 Characterization Protocol for Organic-Rich Shale .....	10
1.3 Research Objectives.....	10
1.4 Structure of the dissertation .....	11
Chapter 2: Background and Literature Review .....	14
2.1 Shale Swelling and Inhibitors .....	14
2.2 Laboratory Measurement of Effective and Relative Permeability .....	17
2.3 Relative Permeability and Wettability .....	21
Chapter 3: The Impact of Shale Preservation on the Petrophysical Properties .....	25
3.1 Introduction.....	25
3.2 experimental Procedures .....	27
3.3 Basic Shale Property Measurements.....	28
3.3.1 Native Shale Water Activity .....	28
3.3.2 Fluid Content of Shale Cores.....	31
3.3.3 Mineralogy Measurement .....	31
3.4 Sample Preparation .....	32
3.4.1 Sample for Monitoring the Weight, Hardness and Velocity.....	32
3.4.2 Sample for Monitoring the Permeability .....	33
3.5 Effect of Preservation on Mechanical Properties of shale .....	34
3.5.1 Change in Density and Porosity.....	34
3.5.2 Change in Sample Weight .....	35
3.5.3 Brinell Hardness Test.....	35

3.5.4 Wave Velocity Measurement.....	37
3.6 Effect of Preservation on Fluid Sensitivity .....	39
3.6.1 Swelling Behavior of Eagle Ford Shale.....	39
3.6.2 Brinell Hardness Test.....	40
3.6.3 Wave Velocity Measurements .....	41
3.6.4 Permeability Measurement: Pressure Penetration Method .....	44
3.6.5 Permeability Measurement: GRI Method.....	47
3.7 Conclusions.....	51
Chapter 4: Interaction of Fracturing Fluids with Organic-Rich Shales .....	53
4.1 Introduction.....	53
4.2 Experimental methods and transient Pressure model .....	54
4.2.1 Experimental Set-up: Pressure Penetration Technique.....	54
4.2.2 Transient Pressure Model for Unsteady State Flow .....	57
4.2.3 Leakage Test after the Permeability Measurement.....	62
4.2.4 Sample Preparation .....	63
4.3 Experimental Results .....	66
4.3 conclusions.....	74
Chapter 5: High-Performance Water-Based Mud Using Nanoparticles.....	76
5.1 Introduction and Past Work .....	76
5.2 Experimental Procedures .....	78
5.2.1 The Properties of Shales: Mineralogy and Water Activity.....	79
5.2.2 The Properties of Water Based Mud and Nano Mud.....	80
5.2.3 PPT Test and Darcy Flow Test .....	81
5.2.3 Permeability Measurement: Detailed Procedures .....	83
5.3 Experimental Results .....	86
5.3.1 Texas Gas Shale Results .....	86
5.3.2 Eagle Ford Shale Results .....	95
5.3.3 Barnett Shale Results .....	101
5.4 Conclusions.....	108

Chapter 6: Relative Permeability Measurement of Organic-Rich Shale .....	113
6.1 Introduction.....	113
6.2 Sample Preparation .....	115
6.2.1 Mineralogy Measurement .....	115
6.2.2 Sample dimensions .....	116
6.3 Experimental Methods .....	116
6.3.1 Fluid Content and Porosity Measurement using NMR.....	117
6.3.2 Outflow Measurement Using RPC Set-up.....	121
6.3.3 Experimental Procedures .....	124
6.3.4 Relative Permeability Calculation using JBN Method .....	129
6.4 Experimental results.....	133
6.5 Conclusions and Future work .....	144
Chapter 7: Conclusions and Future Work.....	147
7.1 Conclusions.....	147
7.2 Recommendations for Future Work.....	149
References.....	152

## List of Tables

Table 1.1:	Technically recoverable shale oil and shale gas resources .....	2
Table 1.2:	Top 10 countries with technically recoverable reservoirs .....	2
Table 2.1	Clay Stabilizers (Swelling Inhibitors).....	16
Table 2.2	Rules of Thumbs for Determining Wettability .....	24
Table 3.1:	Original fluid content of Eagle Ford shale sample. ....	31
Table 3.2:	Mineralogy of Eagle Ford shale.....	32
Table 3.3:	Physical properties of Eagle Ford shale.....	34
Table 3.4:	Type D scale specification. ....	36
Table 3.5:	Brinell hardness change due to the drying process.....	37
Table 3.6:	Wave velocity change due to the drying process.....	38
Table 3.7:	Young’s modulus and Poisson’s ratio results. ....	39
Table 3.8:	Brinell hardness change before and after swelling. ....	40
Table 3.9:	Changes in Young’s modulus and Poisson’s ratio.....	43
Table 3.10:	Summary of mechanical properties for Eagle Ford shale.....	51
Table 3.11:	Summary of fluid sensitivity test results for Eagle Ford shale .....	52
Table 4.1:	XRD mineralogy test results, Utica shales. ....	63
Table 4.2:	Summary of Utica shale test results.....	74
Table 5.1:	XRD mineralogy test result of shales. ....	79
Table 5.2:	The Composition of Base Mud.....	80
Table 5.3:	Mud properties for the base mud and the nano-particle muds.....	81
Table 5.3:	Texas Gas Shale (TGS) permeability results. ....	87
Table 5.4:	Eagle Ford shale permeability results. ....	96
Table 5.5:	The properties of surfactant, StimOII® FBA M.....	102

Table 5.6:	Barnett shale permeability results.....	102
Table 6.1:	Bakken shale mineralogy results .....	116
Table 6.2:	Calculation sheet of the first water-flood results, EBS-1. ....	134
Table 6.3:	In-situ fluid saturation change of the first water-flood, EBS-1. ....	135
Table 6.4:	In-situ fluid saturation change of the second water-flood, EBS-1...	139
Table 6.5:	In-situ fluid saturation change of the first water-flood, EBS-2. ....	141
Table 6.6:	In-situ fluid saturation change of the second water-flood, EBS-2...	143

## List of Figures

Figure 1.1:	Basins with assessed shale oil and shale gas formations.....	1
Figure 1.2:	Texas Barnett Shale Map.....	4
Figure 1.3:	Texas Barnett Shale Total Natural Gas Production.....	5
Figure 1.4:	Texas Barnett Shale Oil Production.....	5
Figure 1.5:	Eagle Ford shale Map.....	6
Figure 1.6:	Utica shale Map.....	7
Figure 1.7:	Bakken shale Map.....	8
Figure 2.1:	Octahedral and tetrahedral layers in clays.....	15
Figure 2.2:	Schematic drawing of core holder and centrifuge equipment.....	18
Figure 2.4:	Pressure profile using oscillating pulse method.....	19
Figure 2.5:	Pulse decay test for Lower Huron shale core.....	20
Figure 2.6:	Steady-state oil/water relative permeabilities measurment.....	22
Figure 2.7:	Water displacing oil from a pore during a waterflood.....	23
Figure 2.8:	Typical oil/water relative permeability curves.....	23
Figure 3.1:	Comparison of crushed rock porosity values.....	26
Figure 3.2:	Test procedure to study the effect of shale preservation.....	27
Figure 3.3:	Native water activity measurement results of Eagle Ford shale.....	29
Figure 3.4:	Desiccators for measuring water activity of shale.....	30
Figure 3.5:	Shale samples on a plate in desiccators.....	30
Figure 3.6:	Sample dimension for weight, hardness measurement.....	32
Figure 3.7:	Disk type sample used for PPT tests.....	34
Figure 3.8:	Weight change due to the drying process.....	35
Figure 3.9:	Durometer and scales for Brinell hardness test.....	36

Figure 3.10: P and S wave transducers and oscilloscope. ....	38
Figure 3.11: Weight change of the dry sample and the preserved sample .....	40
Figure 3.12: Brinell hardness of shale before and after immersion .....	41
Figure 3.13: Brinell hardness of shale before and after immersion .....	42
Figure 3.14: Young's modulus and Poisson's ratio change. ....	44
Figure 3.15: Pressure penetration test set-up.....	45
Figure 3.16: A schematic diagram of the main cell assembly.....	46
Figure 3.17: Brine permeability results for a preserved Eagle Ford shale .....	47
Figure 3.18: Brine permeability results for a unpreserved Eagle Ford. ....	47
Figure 3.19: Schematic of apparatus used for GRI permeability .....	49
Figure 3.20: Nitrogen permeability results of dried-out sample .....	50
Figure 4.1: Schematic of pressure penetration test and compressibility. ....	55
Figure 4.2: Pressure penetration test set-up.....	56
Figure 4.3: Brine compressibility test result and compressibility .....	58
Figure 4.4: Open and closed system volume, and hold-up volume.....	60
Figure 4.5: Displacement vs. pressure build up for open and closed cases.....	60
Figure 4.6: Downstream pressure build-up test result.....	61
Figure 4.7: Graphical slope interpretation of dimensionless pressure vs time....	62
Figure 4.8: Leakage test to monitor the rate of leakage from the test cell. ....	63
Figure 4.9: Oil-cooled saw and prepared rectangular shale core samples. ....	64
Figure 4.10: Epoxy resin encapsulating the shale core. ....	65
Figure 4.11: Sliced disk sample and a desiccator containing saturated salt.....	65
Figure 4.12: Original water activity results, Utica shale. ....	66
Figure 4.13: Brine permeability measurement, HUT-10 sample. ....	67
Figure 4.14: Viscosity measurement versus increasing shear rate. ....	68



Figure 4.15: Initial slick water permeability measurement, HUT-10 sample. ....	68
Figure 4.16: Additional brine permeability measurement, HUT-10 sample. ....	69
Figure 4.17: Initial brine permeability measurement, HUT-12 sample. ....	70
Figure 4.18: Initial slick water permeability measurement, HUT-12 sample. ....	71
Figure 4.19: Another slick water permeability after 10 hours of injection. ....	71
Figure 4.20: Initial brine permeability measurement, HUT-16 sample. ....	72
Figure 4.21: Initial slick water permeability measurement, HUT-16 sample. ....	73
Figure 4.22: Another slick water permeability after 10 hours of injection. ....	73
Figure 5.1: SEM image of Texas gas shale. ....	78
Figure 5.2: The water activity measurement of Eagle Ford and Barnett. ....	79
Figure 5.3: Pressure Penetration Technique test set-up. ....	82
Figure 5.4: Picture of the PPT set-up inside an oven. ....	82
Figure 5.5: Modification of the PPT set-up for Darcy flow test. ....	83
Figure 5.6: Brine permeability results of Texas Gas Shale (TGS 10). ....	88
Figure 5.7: Base mud permeability and following brine permeability. ....	88
Figure 5.8: Brine permeability results of Texas Gas Shale (TGS 7). ....	89
Figure 5.9: 30 ppb nano mud permeability of Texas Gas Shale (TGS 7). ....	90
Figure 5.10: Brine permeability results of Texas Gas Shale (TGS 9). ....	90
Figure 5.11: 10 ppb nano mud permeability, Texas Gas Shale (TGS 9). ....	91
Figure 5.12: Brine permeability of TGS 24 using Darcy flow test. ....	92
Figure 5.13: 10 ppb nano mud permeability results of TGS 24. ....	92
Figure 5.14: Brine permeability results of Texas Gas Shale (TGS 24). ....	93
Figure 5.15: Brine permeability measurement of TGSB 2 using a Darcy test. ....	94
Figure 5.16: 10 % nanoparticle solution permeability of TGSB 2. ....	95
Figure 5.17: Brine permeability measurement of Eagle Ford Shale. ....	97

Figure 5.18: 10 ppb nano mud permeability results of Eagle Ford Shale. ....	97
Figure 5.19: Brine permeability measurement of Eagle Ford Shale .....	98
Figure 5.20: Base mud permeability and 10 ppb nano mud permeability.....	99
Figure 5.21: Brine permeability results of Eagle Ford Shale (WGSB 6).....	99
Figure 5.22: Brine permeability results of WGSB 6 using the Darcy test. ....	100
Figure 5.23: 10 ppb nano-mud permeability results of WGSB 6.....	100
Figure 5.24: Brine permeability results of Eagle Ford Shale (WGSB 6).....	101
Figure 5.25: Brine permeability results of Barnett Shale (PBS 1). ....	103
Figure 5.26: 3% surfactant solution permeability results of PBS 1. ....	104
Figure 5.27: Base mud permeability results of Barnett Shale (PBS 1). ....	104
Figure 5.28: Base mud permeability results with increased pressure .....	105
Figure 5.29: 10 ppb nano mud permeability results of PBS 1.....	106
Figure 5.30: Brine permeability results of PBS 2 using Darcy flow test. ....	107
Figure 5.31: 1% surfactant solution permeability of PBS 2 using Darcy test...107	
Figure 5.32: 10% nanoparticle solution permeability results of PBS 2. ....	108
Figure 6.1: ED-XRF handheld device.....	115
Figure 6.2: Sample dimensions for relative permeability measurements.....	116
Figure 6.3: NMR core analyzer.....	118
Figure 6.4: Bakken shale sample - T <sub>2</sub> Distribution Chart. ....	118
Figure 6.5: T <sub>1</sub> vs. T <sub>2</sub> plot, and T <sub>1</sub> /T <sub>2</sub> ratio vs. T <sub>2</sub> plot.....	119
Figure 6.6: T <sub>2</sub> distribution chart change due to the MnCl <sub>2</sub> flushing.....	120
Figure 6.7: T <sub>2</sub> distribution change after decane injection.....	121
Figure 6.8: A schematic of the RPT set-up. ....	123
Figure 6.9: Photograph of the RPT set-up in the laboratory. ....	124
Figure 6.10: Time-lapse video capture program, VideoVelocity.....	126

Figure 6.11: Collected oil and water at the water-flooding experiment.....	127
Figure 6.12: Original experimental data, first water-flood, Bakken Shale. ....	128
Figure 6.13: Smoothed experimental data, first water-flood.....	129
Figure 6.14: Curve fit of the $N_{pD}$ vs. $\ln(W_i)$ example. ....	130
Figure 6.15: Example curve fit of $\ln 1WiIr$ vs. $\ln 1Wi$ . ....	132
Figure 6.16: Relative permeability curve, first water-flood, EBS-1. ....	136
Figure 6.17: Relative permeability comparison with Brooks-Corey equation. ....	137
Figure 6.18: Original experimental data of the second waterflood (EBS-1).....	138
Figure 6.19: Smoothed data of the second water-flood, EBS-1. ....	138
Figure 6.20: Relative permeability curve, second water-flood, EBS-1.....	139
Figure 6.21: Original experimental data of the first water-flood, EBS-2.....	140
Figure 6.22: Smoothed experimental data of the first water-flood, EBS-2.....	140
Figure 6.23: Relative permeability curve, first water-flood, EBS-2. ....	141
Figure 6.24: Original experimental data of the second water-flood, EBS-2. ....	142
Figure 6.25: Smoothed experimental data of the second water-flood, EBS-2. ....	142
Figure 6.26: Relative permeability curve, second water-flood, EBS-2.....	144
Figure 6.27: Relative permeability curve, first water-flooding, EBS-1 and 2. ....	145
Figure 6.28: Relative permeability curve, 1st and 2nd water-flooding, EBS-2. ....	145

# Chapter 1: Introduction

## 1.1 INTRODUCTION

Oil and natural gas production from shale formations has become the fastest growing energy source in the United States and it also impacts significantly on the global energy system. According to the recent report of U.S. Energy Information Administration (EIA), shale oil and gas resources provided 29 percent of total U.S. crude oil production and 40 percent of total U.S. natural gas production in 2012. Moreover, 345 billion barrels of oil and 7,299 trillion cubic feet of gas are technically recoverable from the shale / tight oil and shale gas in the world (using current technology without considering economic profitability) (Table 1.1).

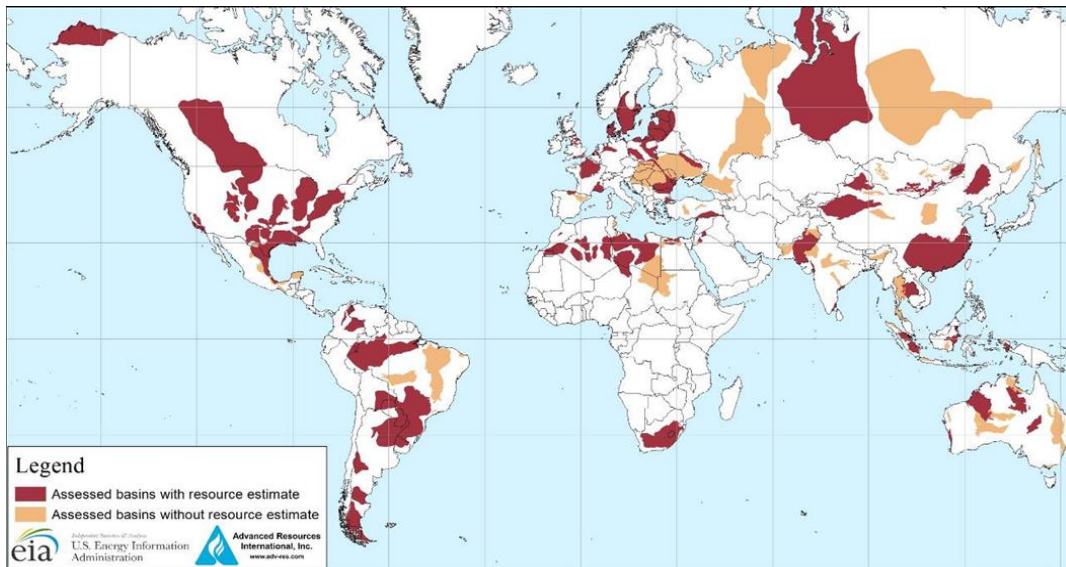


Figure 1.1: Basins with assessed shale oil and shale gas formations. (U.S. basins from U.S. Energy Information Administration and United States Geological Survey; other basins from Advanced Resources International (ARI) based on data from various published studies).

Table 1.1: Technically recoverable shale oil and shale gas resources in the context of total world resources (EIA, Today in Energy, January 2, 2014)

<b>Outside the United States</b>	<b>Crude oil (billion bbl)</b>	<b>Wet natural gas (Tcf)</b>
Shale oil and shale gas	287	6,634
Non-shale	2,847	13,814
Total	3,134	20,451
Increase in total resources due to inclusion of shale oil and shale gas	10%	48%
Shale as a percent of total	9%	32%
<b>United States</b>		
Shale / tight oil and shale gas	58	665
Non-shale	164	1,766
Total	223	2,431
Increase in total resources due to inclusion of shale oil and shale gas	35%	38%
Shale as a percent of total	26%	27%
<b>Total World</b>		
Shale / tight oil and shale gas	345	7,299
Non-shale	3,012	15,583
Total	3,357	22,882
Increase in total resources due to inclusion of shale oil and shale gas	11%	47%
Shale as a percent of total	10%	32%

Table 1.2: Top 10 countries with technically recoverable shale oil / shale gas reservoirs (EIA, Today in Energy, January 2, 2014)

Rank	Country	Shale oil (billion bbl)	Rank	Country	Shale gas (Tcf)
1	Russia	75	1	China	1,115
2	U.S.	58	2	Argentina	802
3	China	32	3	Algeria	707
4	Argentina	27	4	U.S.	665
5	Libya	26	5	Canada	573
6	Australia	18	6	Mexico	545
7	Venezuela	13	7	Australia	437
8	Mexico	13	8	South Africa	390
9	Pakistan	9	9	Russia	285
10	Canada	9	10	Brazil	245
World Total		345	World Total		7,299

Among the 41 countries, the U.S. is ranked second and Canada is ranked 10th for shale oil reserves and US is ranked fourth and Canada is ranked fifth for shale gas reserves (Tables 1.2). Currently, only the U.S. and Canada are producing shale oil and shale gas in commercial quantities. Poland, Argentina, Australia, China, England and Mexico have just begun to study the potential of their shale formations and have drilled primary production wells to investigate the performance of their formations.

However, the economic feasibility of shale resources is very oil price dependent. A shale well costs more than a conventional well because of the additional costs of multi-stage fracturing, but it may produce less hydrocarbons. For this reason, it is very important to understand shale formations and their characteristics. In this dissertation, we will present results for several shale formations in the US, namely the Barnett shale, the Eagle Ford shale, the Utica shale, and the Bakken shale.

The Barnett shale play is one of the largest onshore natural gas fields in the US. This major play sits within the Fort Worth Basin in Northeast Texas. The formation covers 5,000 square miles, and more than 16,000 wells have been drilled since the 1990s, and approximately 13 Tcf of natural gas has been produced during 20 years of production (Browning et al., 2013). The EIA estimated that there are 43 Tcf of recoverable gas reserves.

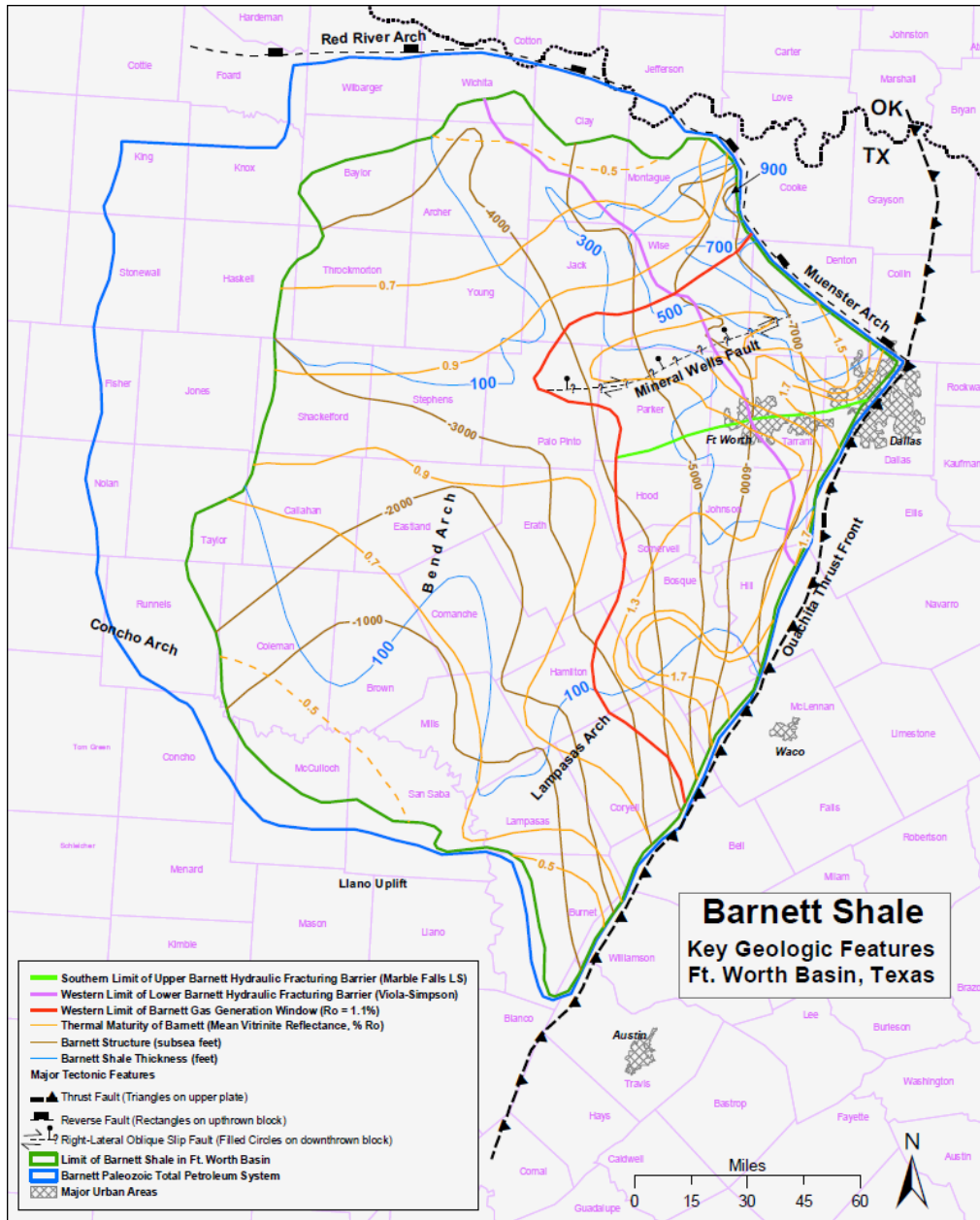


Figure 1.2: Texas Barnett Shale Map. (US EIA, Barnett Shale, ShaleUSA1, 2008)

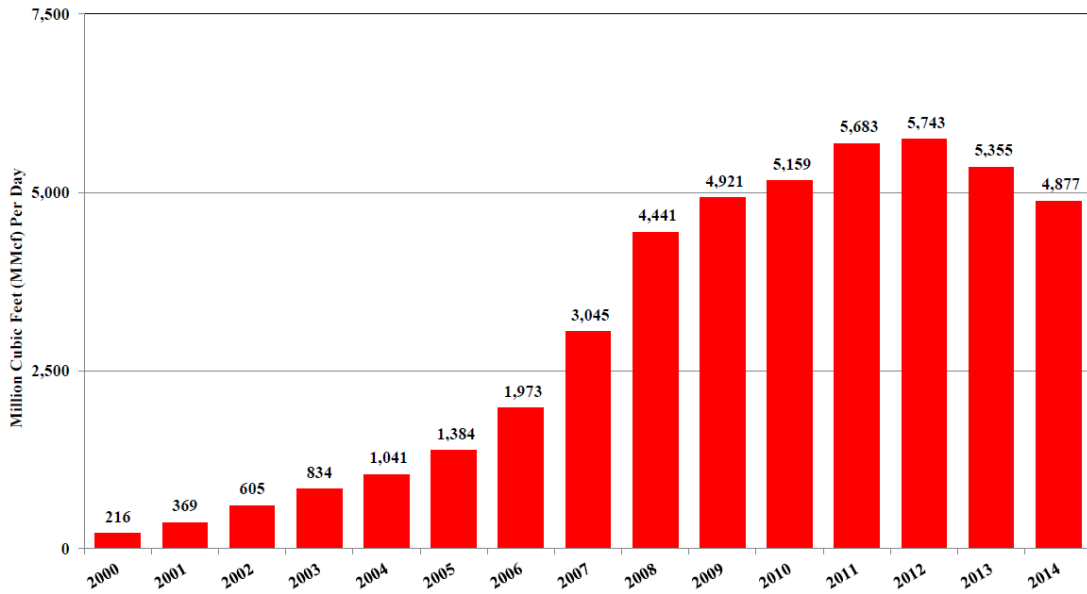


Figure 1.3: Texas Barnett Shale Total Natural Gas Production (Texas Railroad Commission Production Data Query System (PDQ), 2015).

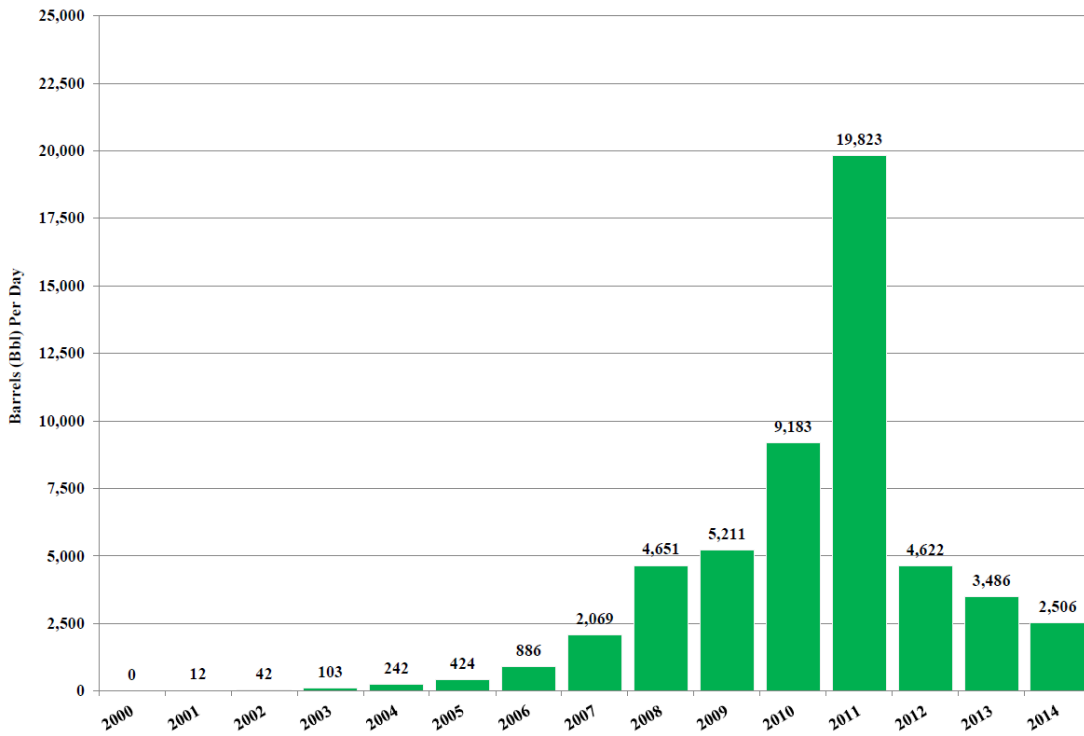


Figure 1.4: Texas Barnett Shale Oil Production (Texas Railroad Commission Production Data Query System (PDQ), 2015).



The Eagle Ford shale formation is located in south Texas, and it consists of organic-rich, calcareous mudrock with mineralogy ranging from 40-90% carbonate minerals, 15-30% clay, and 15-20% silica. The average gross thickness is 350 feet, and oil and gas are produced from depths of between 4,000 and 14,000 feet. The total organic carbon content (TOC) ranges from 2-12%, API gravity is between 28-62°, and porosity is 8-12%. The Eagle Ford is also a very active shale play. EIA estimates the technically recoverable resource at 21 Tcf (US EIA, 2014).

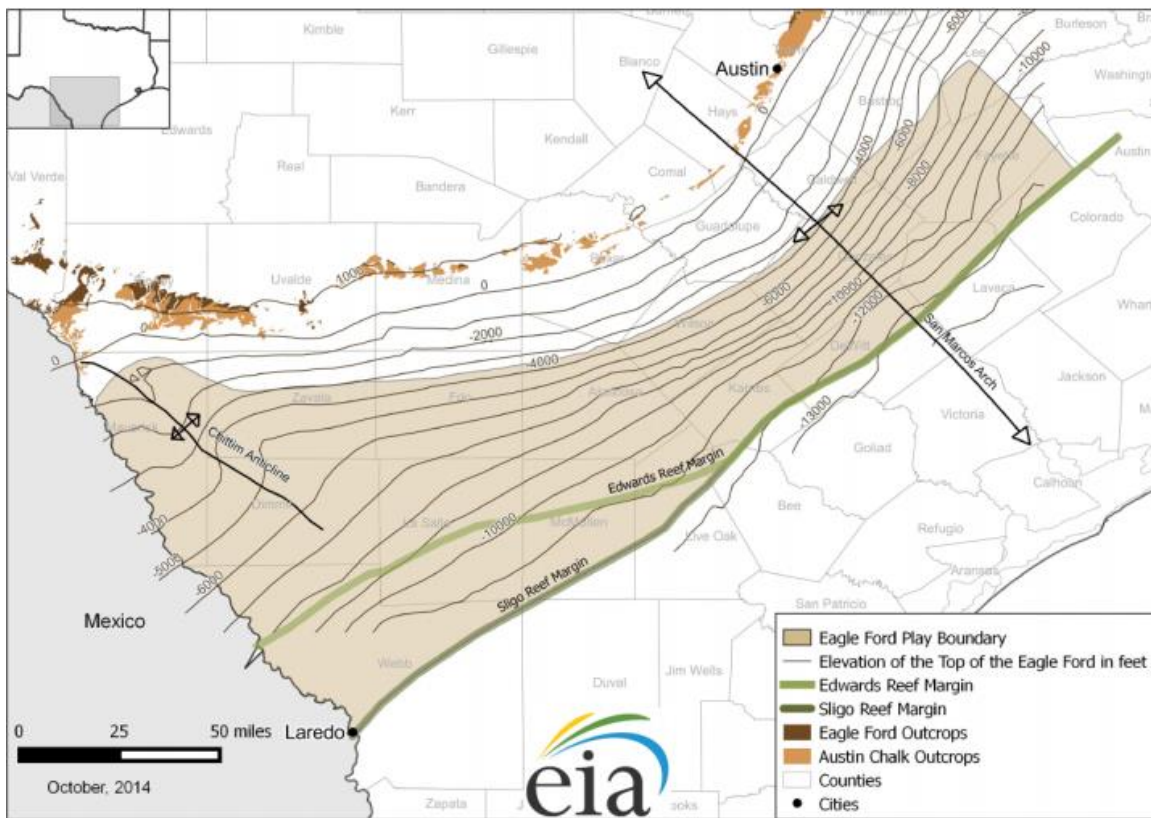


Figure 1.5: Eagle Ford shale Map (U.S. Energy Information Administration, DrillingInfo, Inc., Texas Natural Resources Information, U.S. Geological Survey, Texas Bureau of Economic Geology).

The Utica shale is an Ordovician age natural gas-containing rock formation, and it is located below the Marcellus shale. Both the Utica and the Marcellus shale are part of the Appalachian Basin. The formation extends from eastern Ohio to western New York, and is one of the oldest producing petroleum provinces in the U.S. Currently, the Utica shale is actively developed in eastern Ohio. It contains about 38 trillion cubic feet of technically recoverable natural gas according to the U. S. Geological Survey (Schenk et al., 2012, USGS).

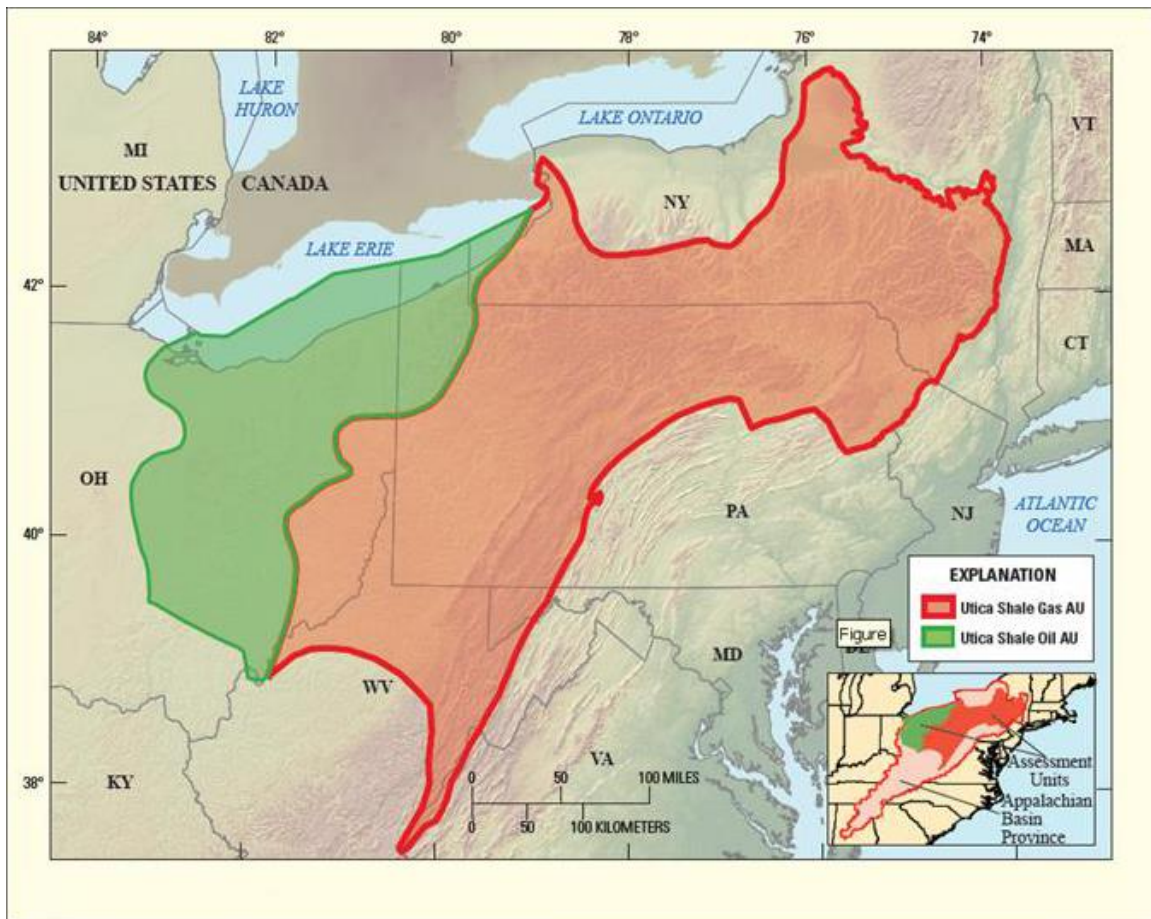


Figure 1.6: Utica shale Map (Schenk et al., 2012, USGS).

The Bakken shale is located within the Williston Basin in Montana and North Dakota. This play contains 3.59 billion barrels of technically recoverable oil, spread out over approximately 6,522 square miles, making it one the largest oilfields in the US. The Bakken shale depth ranges from 4,500 to 7,500 feet, with an average thickness of 22 feet (US EIA, 2011).

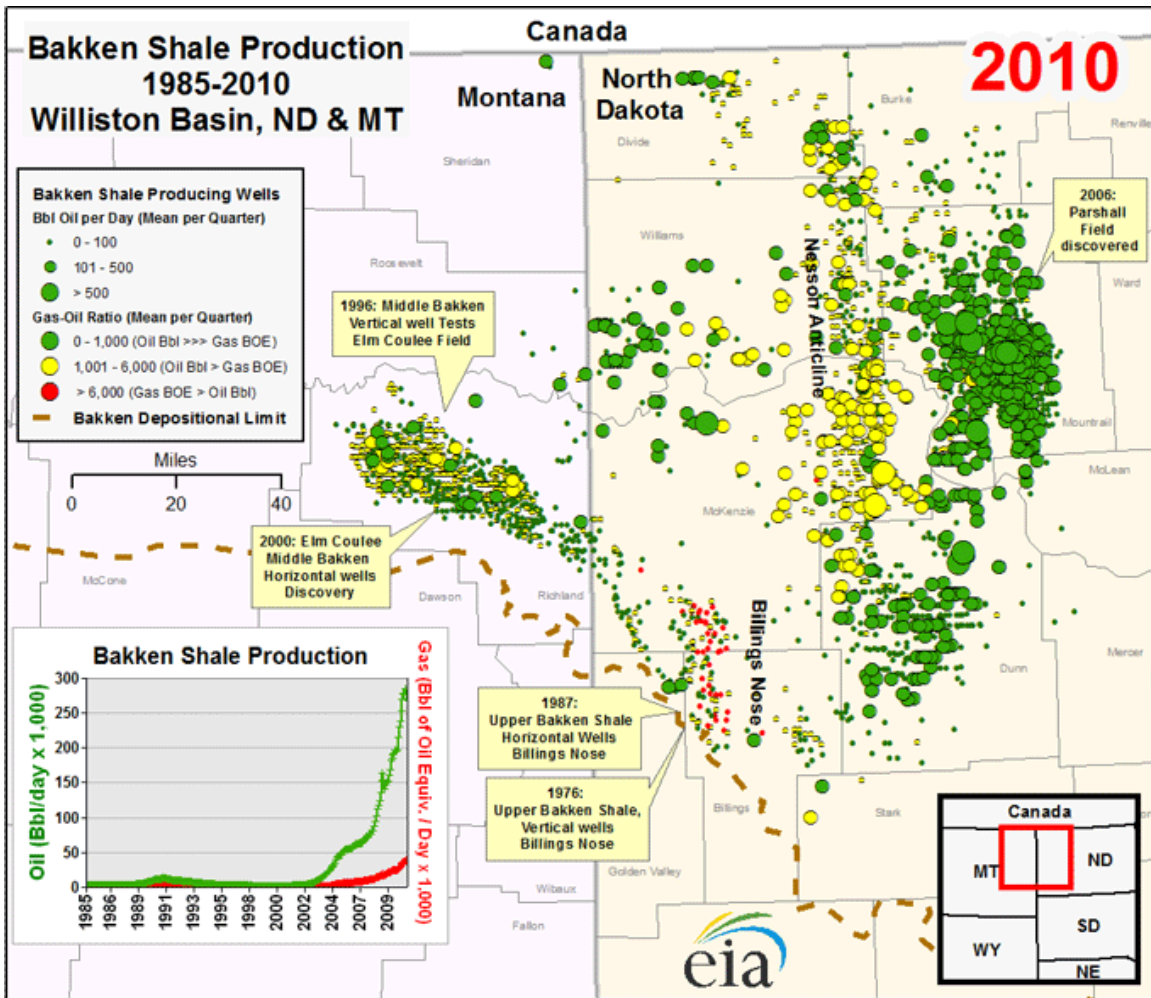


Figure 1.7: Bakken shale Map (U.S. Energy Information Administration, based on data from HPDI, LLC).

## **1.2 MOTIVATION FOR RESEARCH**

### **1.2.1 Wellbore Instability Problems and the Effect of Fluid Interaction on the Petrophysical Properties of Shale**

Drilling through a shale layer often results in borehole instability problems, and this increases drilling cost and operation time. There are several basic factors to be considered for wellbore instability problems in shales: shale lithology, the presence of natural fractures in shale, induced fractures in a brittle shale, and shale hydration failure (Bol et al., 1994). Each of these factors controls the mud weight and the mud design.

To avoid borehole instability problems, drilling mud design is one of the most important factors that needs to be considered. Generally, drilling design includes specifying the mud weight based on the pore pressure, the in-situ stresses, and the well geometry and orientation. The mud weight should lie between the collapse and fracture pressures. The orientation of the well should consider the in-situ stresses and the mechanical properties of the rock that control the mud weight window.

Another important factor, especially for shale, is the potential interaction of clay minerals and the drilling fluid. Many shale reservoirs contain relatively high clay contents, and the water from drilling mud can interact with the clay. Clay easily adsorbs the water and it can be hydrated and weakened, causing hole-collapse and wellbore weakening.

This problem also needs to be considered when designing a fracturing fluid. Shales can be a very water sensitive, i.e. it interacts with water and chemicals in the fluid, and the interaction affects the petrophysical properties. The effect of fluid additives on the properties of organic-rich shale is a very important and interesting subject. Very little work has been done in this area and it is the focus of our work in this dissertation.

### **1.2.2 Characterization Protocol for Organic-Rich Shale**

The petrophysical properties of shales such as mineralogy, permeability, porosity and fluid saturation are important for the successful recovery of hydrocarbon from shales. These parameters are commonly derived from routine and special core analysis (SCAL). For conventional reservoir rock, well-established protocols exist. On the other hand, characterization of unconventional rocks is much more challenging because of their extremely low permeability and complex pore microstructure and brittle characteristics.

In many cases, the measurements of porosity, permeability, and capillary entry pressure require a drying process or crushing process to extract in-situ fluid from a core. However, shales are very water sensitive, i.e. if it loses or gains water from the atmosphere, its inner structure is changed, and the original petrophysical properties are not maintained. In addition, crushed sample tests do not represent the properties of the intact shale, and the test results vary based on the crushed grain size and the crushing procedures. Due to these reasons, the experimental protocol used should not involve drying and crushing in order to measure a shale's in-situ properties.

### **1.3 RESEARCH OBJECTIVES**

The primary objective of this study is to develop and improve water-based drilling fluids and fracturing fluids for organic rich shale reservoirs by using nanoparticles and to investigate fluid flow mechanisms in shales. The objectives can be more specifically written down as follows:

- i. To establish a characterization protocol for organic rich shale;

- ii. To develop low-cost and high-performance water-based muds for organic rich shale, based on using nanoparticle additives;
- iii. To investigate the effect of fracturing fluid content on shale flow properties;
- iv. To gain fundamental insight into water and oil flow in shales.

The primary tasks of the proposed research can be broken down as follows:

- i. Characterize the shale properties of Barnett shale, Texas Gas shale, Eagle Ford shale, Utica shale and Bakken shale in terms of mineralogy, original water activity, porosity, density and fluid saturation.
- ii. Investigate the pore structure of the shale and relate it to the measured properties.
- iii. Measure the liquid permeability of organic rich shale with brine, slick water, mud, and mud with nanoparticles, and show how their permeability is affected by fluid properties.
- iv. Measure in-situ fluid saturation with NMR and measure the shale relative permeability with decane and brine.

#### **1.4 STRUCTURE OF THE DISSERTATION**

The research discussed here presents new methods for studying the interaction between various fluids and organic-rich shale and the development of proper methods to measure apparent and relative permeability of shale. The research is divided into the following chapters:

In **Chapter 2 of the dissertation**, a background and literature review on drilling and fracturing fluid for shale and permeability measurement techniques are discussed from an experimental perspective.

In **Chapter 3**, we show how the petrophysical properties of shales are changed when they are poorly preserved. Experiments were performed to measure several properties such as porosity, density, weight change, hardness, wave velocity and permeability before and after shale samples dried-out. Results are presented to show that there are huge differences between two cases due to the drying process, and proper core preservation and handling methods are suggested.

**Chapter 4** discusses how a fracturing fluid can potentially change the petrophysical properties of shale. Among the petrophysical properties, the fluid permeability is chosen to determine the effect of the fracturing fluid on the shale. The reference permeability with sea water brine was measured and then fracturing fluid was injected into the shale. The brine permeability was re-measured to see the effect of exposure to the fracturing fluid. To measure the fluid permeability, the Pressure Penetration Technique (PPT) was developed and used.

**Chapter 5** focuses on the development of a Water Based Mud (WBM) system for an organic rich shale. Nanoparticles are introduced to block the pore throats of shale and prevent fluid loss into the shale. Texas gas shale, Eagle Ford shale and Barnett shale samples were studied to determine if the nano-particles resulted in inhibitive muds.

**Chapter 6** presents experimental studies used to measure the relative permeability of shale. Such measurements have never been done before. Due to the

extremely low permeability of shale, it is very difficult to measure the relative permeability of shale directly. We propose a method of relative permeability measurement using NMR to measure fluid saturations and a forced injection set-up to conduct the displacement. The in-situ fluid saturation was successfully measured with NMR, and the permeability was measured using a core holder and video monitoring system for oil and water outflow rates.

Finally, **Chapter 7** summarizes the findings and the conclusions. In addition, the future work for this topic is recommended.



## Chapter 2: Background and Literature Review

### 2.1 SHALE SWELLING AND INHIBITORS

Shale is the most common rock encountered when drilling a well. Shales contain a significant proportion of clays which are well known for their swelling tendency and structural instability due to water adsorption. Due to this characteristic, shales have been a significant problem for the petroleum industry and have led to additional costs for drilling and well completion of water sensitive shale formations (Wong, 2001).

Clays have a crystalline layered structure (Coulombe, 2007). Each layer consists of octahedral sheets of  $\text{Al}^{3+}$ ,  $\text{Mg}^{2+}$ , or  $\text{Fe}^{3+}$  oxides and tetrahedral sheets of  $\text{Si}^{4+}$  oxides (Auerbach, 2007). If a clay mineral contains one tetrahedral and one octahedral sheet, it is known as a 1:1 clay. If it contains two tetrahedral sheets and one central octahedral sheet, it is called a 2:1 clay (Fink, 2011).

Smectites are 2:1 clays that are susceptible to swelling and are very commonly encountered in drilling (Anderson et al., 2010). The structure of smectite, one octahedral sheet sandwiched between two tetrahedral sheets that share oxygen atoms (Figure 2.1), results in poor hydrogen bonding between layers. This Hoffman structure (Hoffmann, 1962) shows that the unit layers are stacked with oxygen atoms facing each other. The distance between unit layers is called c-spacing (Fink, 2011). As water enters the space between the layers, the clay expands the c-spacing increases, discontinuously at first and (up to 3-4 water molecule diameters) and continuously thereafter.

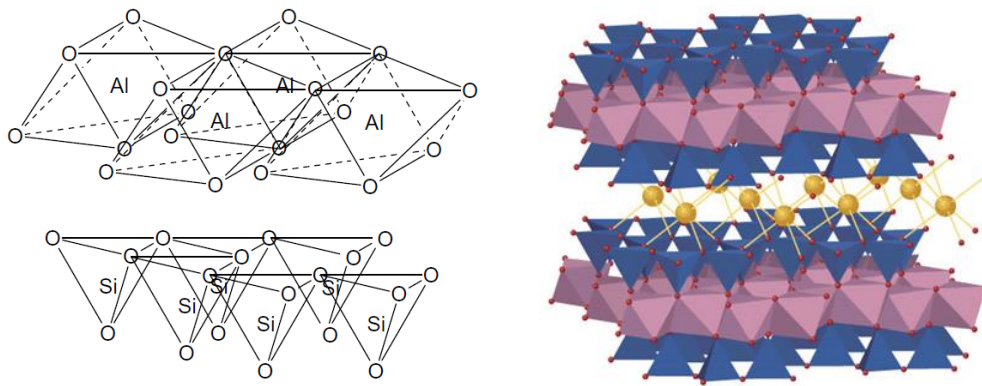


Figure 2.1: Octahedral and tetrahedral layers in clays (Murray, 2007) and Hoffmann structure (Coulombe, 2007).

Many 2:1 clays swell through a series of different mechanisms. At small interlayer spacing, crystalline swelling dominates, in which water molecules adsorb on the crystal surface, one water layer at a time resulting in discontinuous jumps in the c-spacing (the spacing between jumps being equal to the diameter of the water molecule). At larger c-spacing, when clays come into contact with water containing ions, the exchangeable cations in the clay lattice can be substituted with others. However, the lattice charge must be compensated for by the interlayer cations (Fink, 2011). This hydration and dehydration of ions results as they move in and out of the interlayer region results in hydration swelling.

Finally, at even larger c-spacing, osmotic swelling, dominated by electrostatic and van-der Waals interactions takes over. If the concentration of cations between the unit layers is higher than the concentration of cations in the surrounding water, water is osmotically drawn in and ions are expelled and the clay expands (Patel et al., 2007).

To solve this swelling problem, the use of proper drilling mud chemistry is a key solution. Current industry tendency for drilling mud focuses on improving the compatibility of water-based muds (WBM) or to use sustainable oil-based muds (OBM)

(Khodjaa et al., 2010). In the case of OBM and synthetic-based muds (SBM), if mud weight and invert emulsion salinity are properly established, clay swelling is not a big issue. However, WBM has much more problems due to its adverse interactions with clay even though it is an attractive alternative from an environmental point-of-view (van Oort, 2003).

To prevent swelling of shales during drilling, various kinds of swelling inhibitors have been developed. Table 2.1 shows a list of swelling inhibitors and some reference papers where they are discussed in more detail.

Table 2.1 Clay Stabilizers (Swelling Inhibitors)

Additive	References
Polymer lattices	Stowe et al. (2002)
Partially hydrolyzed polyvinylacetatea	Kubena Jr., et al. (1993)
Polyacrylamide	Zaitoun and Berton (1990)
Copolymer of anionic and cationic monomers	Aviles-Alcantara et al. (2000)
Partially hydrolyzed acrylamide-acrylate copolymer, potassium chloride, and poly-anionic cellulose (PAC)	Halliday and Thielen (1987)
Aluminum/guanidine complexes with cationic starches and poly-alkylene glycols	Branch (1988)
Hydroxy-aldehydes or hydroxy-ketones	Westerkamp et al. (1991)
Polyols and alkaline salt	Hale and van Oort (1997)
Tetra-methyl ammonium chloride and methyl chloride quaternary salt of poly-ethylene amine	Aften and Gabel (1992, 1994)
Pyruvic aldehyde and a tri-amine	Crenshaw et al. (2002)
Copolymer of styrene and substituted maleic anhydride (MA)	Smith and Balson (2000)
Quaternary tri-hydroxy alkyl amine	Patel and McLaurine (1993)

The cations which are located in the interlayer region can be freely exchanged. The cation exchange capacity of the clay mineral is a measure of the interlayer cation concentration (Blachier et al., 2009) and is related to the amount of swelling. Usually cations with high valence are more strongly adsorbed than ions with low valence. The higher valence ions are also able to reduce the negative charge on the clay surface and the electrostatic repulsion between the clay platelets and thereby reduce swelling. Thus, an appropriate ion exchange reaction may be helpful in clay stabilization (Anderson et al., 2010). Most cationic clay stabilizers contain polyvalent cations that can adsorb irreversibly to the clay surface.

Sensoy et al. (2009), Cai et al. (2012) and Ji et al (2012) introduced surface-modified silica nanoparticles as a physical shale inhibitor. Instead of exchanging cations to reduce swelling, nanoparticles act by plugging the pores and micro-fractures in shales and prevent water invasion into the shale. By decreasing the amount of water invasion into shale, shale swelling can be minimized.

## **2.2 LABORATORY MEASUREMENT OF EFFECTIVE AND RELATIVE PERMEABILITY**

The steady-state measurement is the most reliable measurement technique for obtaining the effective and relative permeability of a core sample. The pressure drops and the saturation of fluids can be measured directly during the measurement, and the governing equation is Darcy's law which can be used to obtain the permeability. The relative permeability curve is obtained by increasing the injection rate of one phase stepwise. However, the steady state method is time-consuming. It takes several hours or even days even days get the equilibrium saturation level. Due to the long test times, it is

It is not possible to use this method for extremely low permeability rocks such as shales (Honarpour and Mahmood, 1988) since the time needed would be several months.

The unsteady-state method is a much quicker method than the steady-state method. The Buckley-Leverett equation is the basic equation used to analyze the linear displacement of fluids, and the Johnson-Bossler-Naumann (JBN), Welge, and Jones-Roszelle methods are the most common methods used to calculate the relative permeability using the following information: saturation levels, capillary pressure, fluid viscosity, and flow rates (Honarpour et al., 1986).

The centrifuge technique is a variation of the unsteady-state method, and it uses relatively small cores. The core needs to be first saturated with brine using a core saturation cell. Then the cores are spun with known angular speed and centrifugal force, and the production of fluid is measured as a function of time. The production vs time data can be used to infer the relative permeability (van Spronson, 1982). Even though, the centrifuge method is simple and faster method than steady-state, it has many limitations such as the capillary end effect. In addition, there is no relative permeability data for the displacing fluid (Honarpour and Mahmood, 1988).

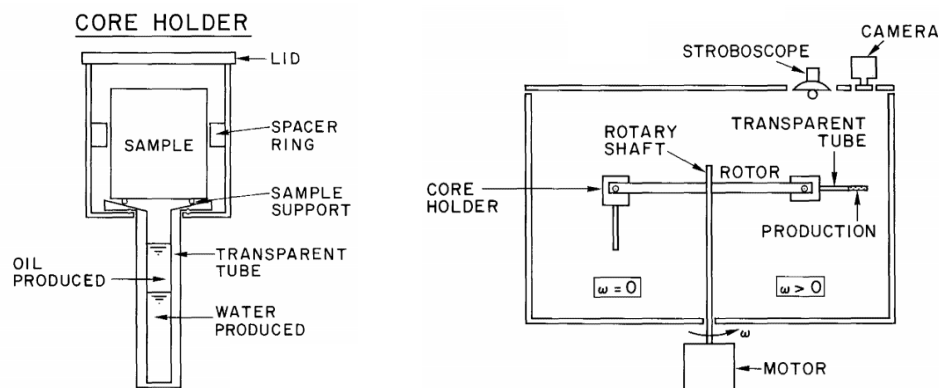


Figure 2.2: Schematic drawing of core holder and experimental set-up of centrifuge equipment (van Spronson, 1982).

Rudd (1966) introduced the pressure decay measurement which is now a widely used technique. The pressure cell is filled with compressed gas, and the core sample is sealed in the sample cell which has blanks of known volume (Figure 2.3). It measures the time interval between the initial pressure and the attained equilibrium pressure, and it is proportional to permeability. It takes only few seconds for normal permeability core and several minutes for dense carbonate core. This method is attractive for its short test time and straight forward operation, and it represents the permeability of inhomogeneous formation well because it use a whole core technique instead of core plugs.

There are three versions of the pressure decay method available: the oscillating pulse method (Fisher and Paterson, 1992), the pulse decay method (Jones, 1997), and the GRI method (Tinni et al, 2012). The oscillating pulse method calibrates permeability using a pressure wave which has constant amplitude and frequency. The shift of amplitude and phase is used to compute permeability. Figure 2.4 shows the pressure response for a single pulse test. The time lag between each pulse, the time at proceeding point, and the delay time of the pressure response are taken to calibrate the permeability (El-Khatib, 2013).

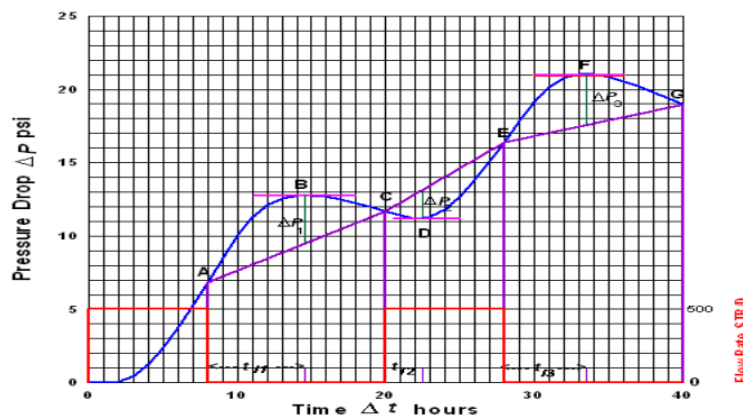


Figure 2.4: Pressure profile using oscillating pulse method (El-Khatib, 2013).

The pulse decay method introduces a pressure pulse at the end of core, and measures the transient pressure decay over time to estimate permeability. Figure 2.5 shows the pressure behavior for a lower Huron shale plug.. Helium and methane were used as the filling gas, and core plugs and crushed core chips were used to measure the permeability (Luffel et al., 1993).

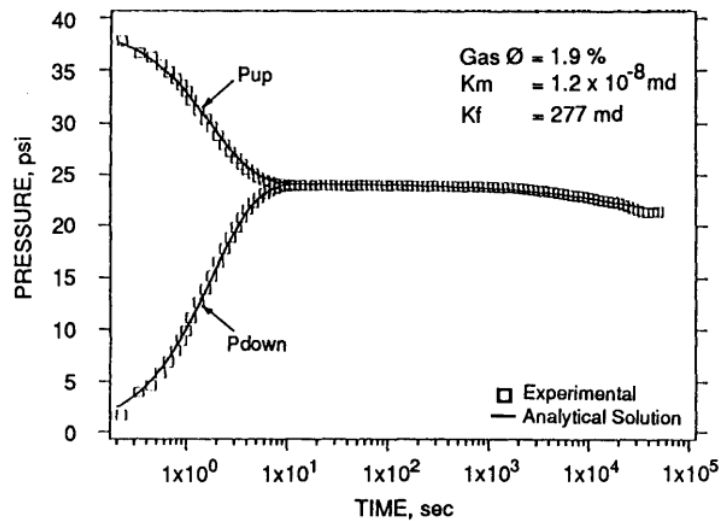


Figure 2.5: Pulse decay test for Lower Huron shale core (Luffel et al., 1993).

The Gas Research Institute (GRI) method uses crushed core sample to measure the matrix permeability. The benefit of a crushed sample is that it eliminates the effect of induced fractures and cracks (Tinni et al, 2012). A more detailed discussion of the GRI method is provided in Chapter 3.

The above methods measure the single phase or the effective permeability to a given phase. When the relative permeability curve is measured, accurate saturation determination is very critical. There are two approaches to measuring the fluid saturation; measure the average saturation value by measuring the volume of cumulative injection and production. The biggest weakness of the method is the significant errors that are

introduced if the pore volume of the core sample is too small. To reduce the errors a closed-loop system is often used. Gravimetric and extraction methods which get saturation by a weight change measurement are also used. X-ray absorption, nuclear magnetic resonance (NMR), gamma ray attenuation, neutron scattering, sonic methods, electrical resistivity, and computerized tomography (CT) have been used successfully to measure the in-situ saturation of cores. These techniques offer great accuracy and reliability compared to the fluid volume measurement techniques (Honarpour and Mahmood, 1988). In this dissertation, an NMR method is used to calibrate the fluid saturation of cores.

### **2.3 RELATIVE PERMEABILITY AND WETTABILITY**

Relative permeability represents the ability of a fluid to flow in the core when more than one fluid is present. The pore geometry, fluid distribution, saturation history, and wettability affect this flow property. Wettability is a major factor that controls the flow and spatial distribution of in-situ fluids (Anderson, 1987).

Figure 2.6 shows the relative permeability curves of preferentially oil wet and water wet rocks. Wettability affects the end-point water permeability at irreducible oil saturation, oil and water relative permeability at each saturation point, and also the cross-over point at which oil and water relative permeability are equal. For oil-wet cores, the maximum water permeability is high (about 70%), but it is small (about 30%) for a water-wet core. The cross-over point is about 65% for an oil wet rock and 35% for a water-wet rock. The water relative permeability for an oil-wet rock is higher than for a water-wet rock, and the oil relative permeability of oil-wet rock is lower than for a water-wet rock for all saturations (Anderson, 1987).



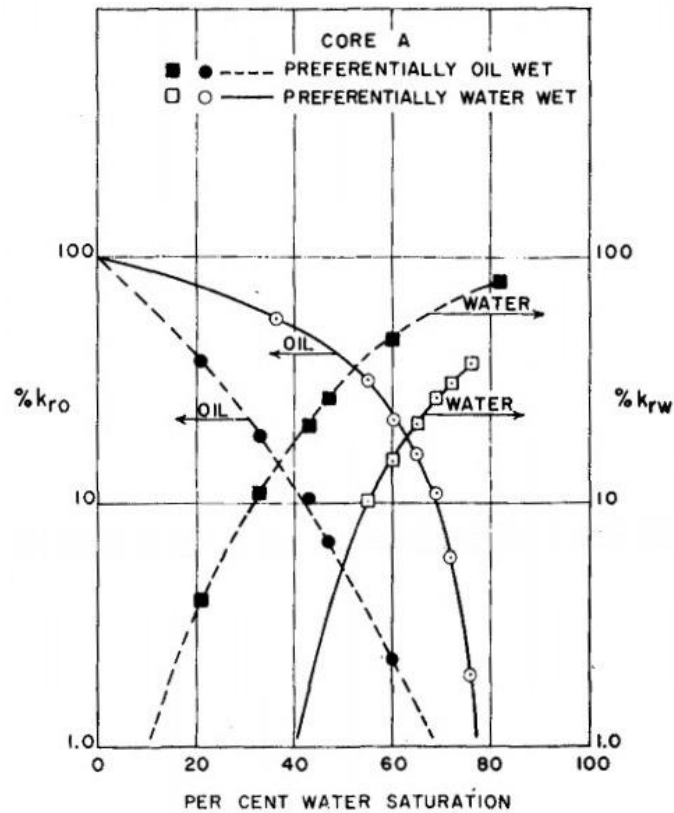


Figure 2.6: Steady-state oil/water relative permeabilities measured with heptane and brine in water- and oil-wet synthetic Alundum core (Jennings, 1957).

The differences in relative permeability with wettability are caused by the differences in the fluid distribution. Figure 2.7 shows the fluid distribution of water-wet and oil-wet rocks, and how the change of distribution occurs during water-flooding. The reason for this distribution difference is that water-flooding is an imbibition process for a water-wet rock, but it is a drainage process for oil-wet rock. For strongly water wet-cores, oil is located at the big pores and water is located at the small pores. Water in the small pores has little effect on the flow of oil, so the relative permeability of oil is relatively high. In contrast, the flow of water is limited by the oil in the large pores, so the relative permeability of water is relatively low. For strongly oil-wet cores, the fluid distribution

the relative permeability of water is relatively high and the relative permeability oil is relatively low due to the blocking by residual water in the large pores (Raza et al, 1971).

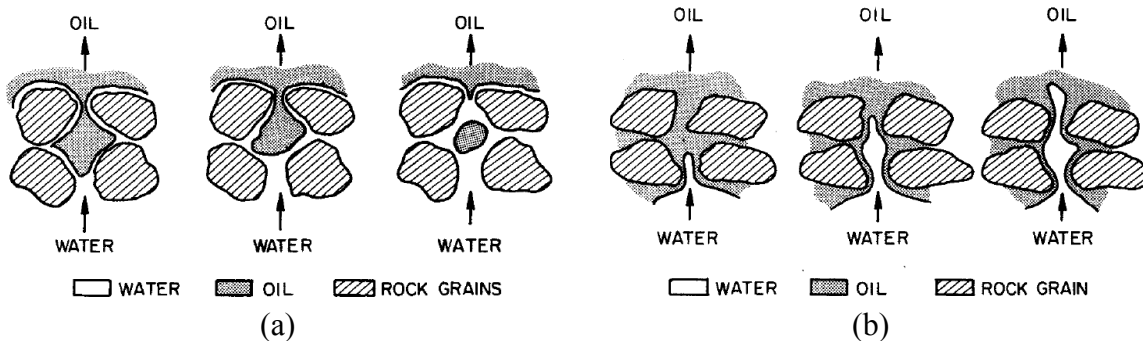


Figure 2.7: Water displacing oil from a pore during a waterflood: (a) strongly water-wet rock, (b) strongly oil-wet rock. (Raza et al, 1971)

Figure 2.8 and Table 2.2 show some rules of thumb relating wettability and relative permeability. As can be seen in Figure 2.4 the cross-over point is greater than 50% in a strongly water-wet rock, and it is smaller than 50% in a strongly oil-wet rock. The other comments made earlier about end-point relative permeabilities and residual saturations are also evident in the figures (Anderson, 1987).

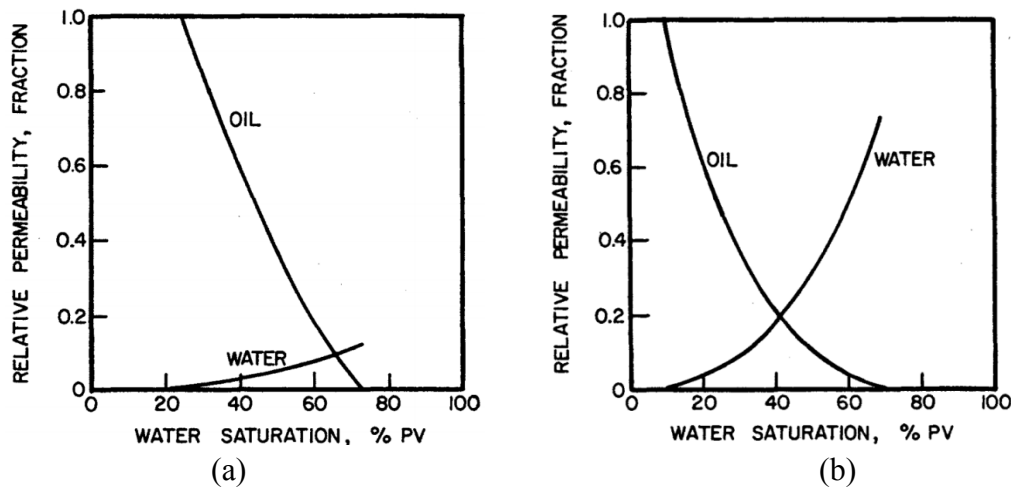


Figure 2.8: Typical oil/water relative permeability curves, water saturation increasing. Based on the effective permeability to oil at the reservoir interstitial water saturation: (a) strongly water-wet rock, (b) strongly oil-wet rock. (Craig, 1971)

Table 2.2 Rules of Thumbs for Determining Wettability (Craig, 1971)

<b>Contents</b>	<b>Water-Wet</b>	<b>Oil-Wet</b>
Interstitial Water Saturation	Usually greater than 20 to 25% PV	Generally less than 15% PV.
Saturation at which oil and water relative permeabilities are equal	Greater than 50% water saturation	Less than 50% water saturation
Relative permeability to water at the maximum water saturation	Generally less than 30%	Greater than 50% and approaching 100%

## **Chapter 3: The Impact of Shale Preservation on the Petrophysical Properties of Organic-Rich Shales**

### **3.1 INTRODUCTION**

In recent years, shale oil and gas has played an important role in hydrocarbon production in the US. Due to horizontal drilling and hydraulic fracturing, shale plays have received more interest from companies and governments. The development of shale reservoirs is highly dependent on petrophysical parameters. Reservoir properties such as lithology, porosity, permeability, and fluid saturation are important for evaluating storage capability and deliverability (Shebl et al. 2013).

For a conventional reservoir, well-established protocols exist for core analysis and log analysis. However, there is no standard for measuring the petrophysical properties of shale, and the procedures vary substantially from one lab to another (Passey et al. 2010; Civan et al. 2012; Kumar et al. 2012). Passey et al. (2010) sent their shale samples to three commercial laboratories for measurement of porosity and permeability. They observed that there were significant disparities in both porosity and permeability results (Figure 3.1). They concluded that this was because there was no standard protocol to handle shale samples (Passey et al., 2010).

Quite often, shale permeability and mechanical property data measurements are obtained from shales that are not preserved, as these shales are easier to obtain (Kumar et al. 2012). Sometimes tests are performed on reconstituted and compacted samples that are made from drill- chips (Chenevert et al. 1989; Passey et al. 2010).

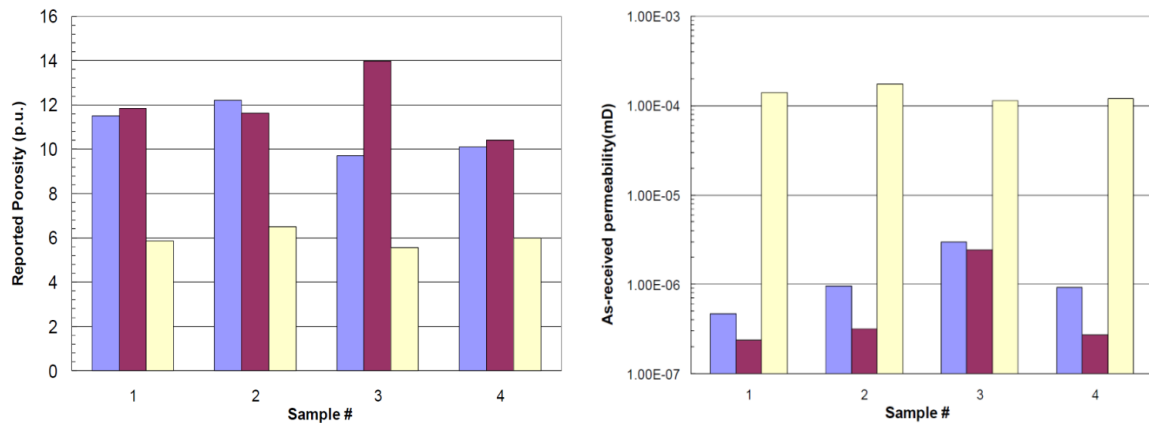


Figure 3.1: a) Comparison of crushed rock porosity values from three different commercial laboratories. b) As-received permeability values reported by the same commercial laboratories on splits from the same samples (Passey et al., 2010).

However, shale is very sensitive to water, so the properties of shale will be changed if it is poorly preserved (Weaver et al. 2012). In this chapter, a series of experiments were performed on hydrocarbon bearing shales that determine the following petrophysical properties: mineralogy, native shale water activity, original fluid content, Brinell hardness change under swelling, sonic velocities change under swelling, and fluid permeability. As an example of an organic rich shale, Eagle Ford shale which is one of the most active shale plays in the US is chosen. In south Texas, more than 1000 wells were drilled during 2008 to 2011 (Tian et al. 2013). Large and consistent differences are observed in the shale's measured properties if the shale is not properly preserved.

In this chapter, the measurements on well preserved and dried out shale samples were first compared. The large differences observed highlight the significance of high quality preservation techniques. A methodology to preserve and prepare shales for petrophysical measurements is presented.

### 3.2 EXPERIMENTAL PROCEDURES

The test procedures used to highlight the effect of shale preservation are shown in Figure 3.2. Before starting the main study, the shale's petrophysical properties of original or native water activity, fluid content and mineralogy were measured. After that, different size samples were prepared to use for the mechanical property and permeability tests.

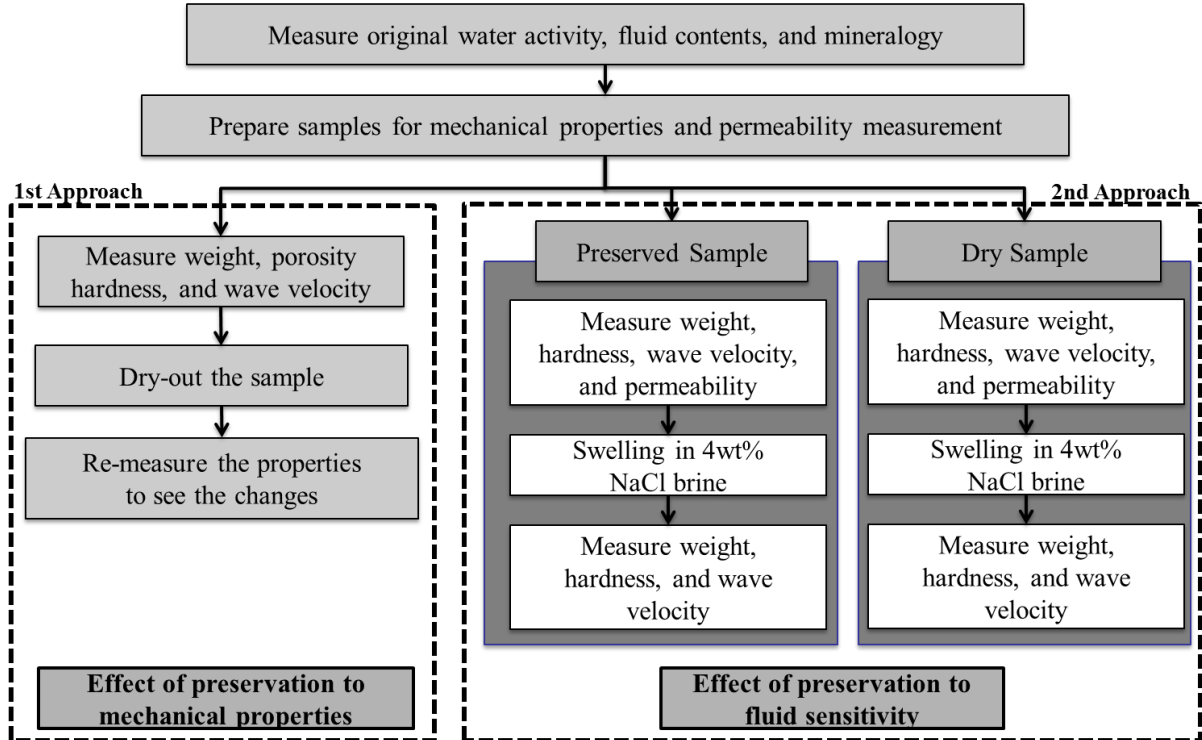


Figure 3.2: Test procedure to study the effect of shale preservation.

Two different approaches were used to monitor the effect of preservation on the mechanical properties and fluid sensitivity of shale. The first approach was to measure the change in mechanical properties when the sample was dried out. In this approach, the same sample was used from the start to the end. The original sample's weight, porosity, hardness, and wave velocity were measured. It was then placed into an oven at 80C and

dried out for two days to evaporate the in-situ fluid from the sample. After the drying process, all properties were measured again.

The second approach was to observe the change in fluid sensitivity of the shale due to poor preservation. Two similar samples were prepared from the same core with the same formation depth and similar mineralogy. One sample was tested in its original condition, and the other sample was dried in the oven for two days to represent a poorly preserved sample. Both samples were tested using the same procedures. The original weight, hardness, wave velocity and permeability were measured. After that, the samples were soaked in a 4 weight percent sodium chloride solution for one day. Then the altered weight, hardness and wave velocity were measured again. The change in the petrophysical properties of the two samples was then recorded.

### **3.3 BASIC SHALE PROPERTY MEASUREMENTS**

#### **3.3.1 Native Shale Water Activity**

The original water activity of shale was determined using an adsorption isotherm test. To conduct this test, several small pieces of shale were used. The sample surfaces were cleaned with hexane, their initial weight measured, and then they were placed in desiccators. Each desiccator has a different water activity from 0.35 to 0.98. As the sample weight reached equilibrium, the weight change was graphed, and then the original water activity of the shale sample was estimated using the method shown below.

Figure 3.3 is the weight change graph of the preserved Eagle Ford shale samples. Since each sample had a slightly different weight, the weight change was calculated as a percentage of the original weight. If the weight was not changed for a given water activity, that value is the original water activity of the shale. In Figure 3.3, the sample

weight does not change at an interpolated water activity of 0.72, which means that the original water activity of the shale sample is 0.72. With the native shale water activity established, the shale samples were kept in desiccators with this original water activity. The shale sample can be maintained at a preserved status without losing or gaining water from the surrounding air using this method (Chenevert et al. 2001). If the water activity of the shale sample is less than 0.5 which is the average humidity at an indoor laboratory, the sample is considered to be an unpreserved sample.

In our shale testing lab, several desiccators that contain saturated salts were used to maintain constant relative humidity (Figure 3.4). The shale samples were placed on plates above the saturated salt solution (Figure 3.5). As an example the following materials were used to achieve different relative water activity: Sodium tartrate (0.92), NaCl (0.755),  $\text{Ca}(\text{NO}_3)_2 \cdot 4\text{H}_2\text{O}$  (0.51), and  $\text{MgCl}_2 \cdot 6\text{H}_2\text{O}$  (0.33) (Winston and Bates, 1960). This range of water activity ensures that a broad range of water activities is tested.

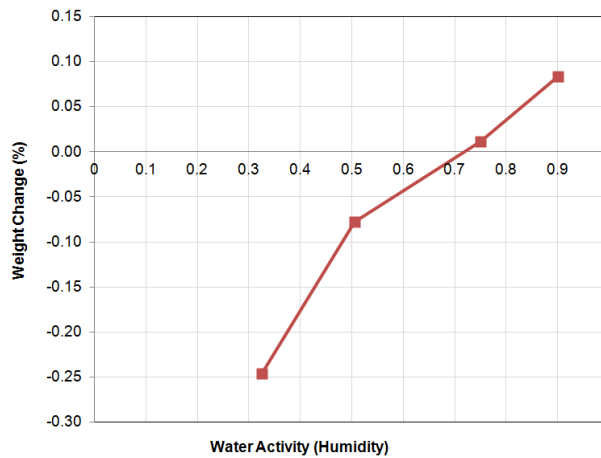


Figure 3.3: Native water activity measurement results of Eagle Ford shale.





Figure 3.4: Desiccators for measuring water activity of shale.



Figure 3.5: Shale samples on a plate in desiccators (Zhou et al. 2013).

### 3.3.2 Fluid Content of Shale Cores

The Gas Research Institute (GRI) method of shale sample analysis was used to measure the original fluid content and the physical properties of Eagle Ford shale samples. The test was performed by Weatherford laboratory in Houston. The shale sample was crushed into small particles from 0.5 to 0.85 mm in diameter in order to more quickly remove the pore liquid by distillation-extraction. This test provided fluid saturations, density, and porosity information. Table 3.1 shows the original fluid content of the Eagle Ford shale samples.

Table 3.1: Original fluid content of Eagle Ford shale sample.

<b>Fluid Saturation</b>	<b>Water Saturation</b>	<b>Oil Saturation</b>	<b>Gas Saturation</b>	<b>Totals</b>
% of Pore Volume	42.1	20.5	37.4	100

### 3.3.3 Mineralogy Measurement

X-ray diffraction (XRD) was performed to determine the mineralogy of the Eagle Ford shale. The crystalline structure, which is unique to each mineral, was determined using X-ray diffraction (Breedon and Shipman, 2004). Among the minerals present in shales, the percentage composition of quartz, calcite and clay were the primary targets because these minerals are the primary constituents of shale and are directly related to shale mechanical properties and shale's sensitivity when it interacts with water-based fluids (Zhou et al. 2013). Table 3.2 lists the Eagle Ford shale mineralogy. It contains twenty-two weight percent illite and sixty weight percent calcite. Total clay weight percentage is 25%, so the sample has a medium clay content as compared to other shales. Samples with higher clay content are expected to show even more of a difference between preserved and unpreserved samples.

Table 3.2: Mineralogy of Eagle Ford shale (weight %, X-ray diffraction method).

Clays			Carbonates		Other minerals					Totals			
Chlorite	Illite	Smectite	Calcite	Dolomite	Quartz	K-spar	Plag.	Pyrite	Zeolite	Barite	Clays	Carb.	Other
2	22	1	60	1	8	1	4	1	0	0	25	61	14

Smectite includes mixed layer clays with illite layers.

### 3.4 SAMPLE PREPARATION

#### 3.4.1 Sample for Monitoring the Change of Weight, Hardness and Wave Velocity

Shale specimens were prepared by cutting them into a 1 inch cubes (Figure 3.6). There are some clear advantages in using test samples that do not require coring. Often preserved shales are difficult to core as the rotation of the coring bit shears the sample apart and core recovery can be poor (particularly in high clay content samples). Rectangular samples are much easier to prepare as they can be cut with a straight precision saw cut. Rectangular or cubic samples also allow us to make measurements parallel and perpendicular to the bedding planes simultaneously and on the same sample. Since preserved shale samples are difficult to obtain it is important to minimize shale sample usage.

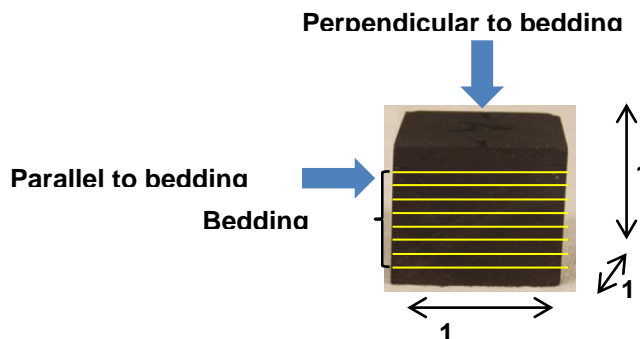


Figure 3.6: Sample dimension for weight, hardness and wave velocity measurement.

Samples that had been stored in mineral oil were washed with hexane. To see the effect of preservation, dried-out samples were required to compare with well-preserved samples. Several samples were placed into a lab oven and kept at 200°F for two days to extract the fluid from the sample. They were then cooled at room temperature. Even though this baking process did not extract all the fluid from inside the sample, it was enough to simulate the condition of a poorly preserved shale sample. All of the following tests were performed with preserved and dried-out samples for comparison.

Finally, it is important to state the importance of proper coring and core preservation procedures in the field. All cores taken from the well must be preserved and sealed in wax or plastic with minimum exposure to the atmosphere. These procedures are well established in the industry and should be used when a specific request is made of the service provider. When the core needs to be slabbed, the larger portion should be stored under mineral oil to preserve its water content.

#### **3.4.2 Sample for Monitoring the Change of Brine and Gas permeability**

Disk type samples were prepared for fluid permeability measurements. These samples were specially designed for the PPT (Pressure Penetration Technique) test set-up. Figure 3.7 shows a photograph of a test specimen. It is 2.5 inch in diameter and 0.25 inch thick. The center of the sample is shale (black in color in the picture). The dimension of the shale part is 1.25 inch square. Epoxy resin occupies the area outside the shale (yellow color). This type of sample enables us to measure the shale's permeability without changing the original composition or water content of the shale by preparing and storing the samples at the shale's native water activity.

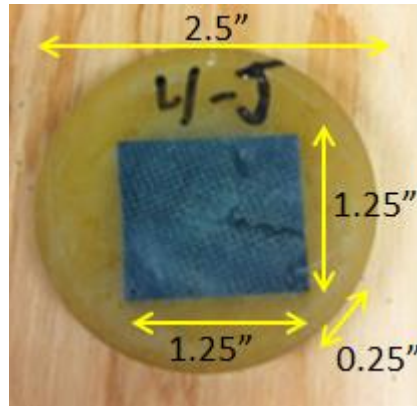


Figure 3.7: Disk type sample used for PPT tests.

### 3.5 EFFECT OF PRESERVATION ON MECHANICAL PROPERTIES OF SHALE

#### 3.5.1 Change in Density and Porosity

To show the changes of density and porosity caused by poor preservation, the physical properties for shale samples were measured when the shale was both well preserved and when it was dried out. There was not much difference in density results. Bulk density decreased slightly, and grain density increased. However, the gas filled porosity, as measured by the gas expansion method, increased from 1.8 to 4.9, which is 2.7 times bigger than the original value (Table 3.3). This shows that the drying process changes the original pore structure and increases the accessible pore space.

Table 3.3: Physical properties of Eagle Ford shale.

Preserved			Dried (Unpreserved)		
Bulk Density	Grain Density	Gas Filled Porosity	Bulk Density	Grain Density	Helium Porosity
2.55 gm/cc	2.60 gm/cc	1.8% of BV	2.53 gm/cc	2.65 gm/cc	4.9% of BV

### 3.5.2 Change in Sample Weight

To show the changes of weight due to the drying process, the sample weight was measured before and after the oven drying procedure. The original sample weight was 27.7g and it was reduced to 24.5g. The sample weight was decreased by 11.54% due to the drying process (Figure 3.8). Because no solid material was detached from the sample during this drying process, the weight difference was solely caused by the evaporation of in-situ fluids. Both water and oil inside the sample escaped due to the drying process, and it affected other properties which were measured within this study.

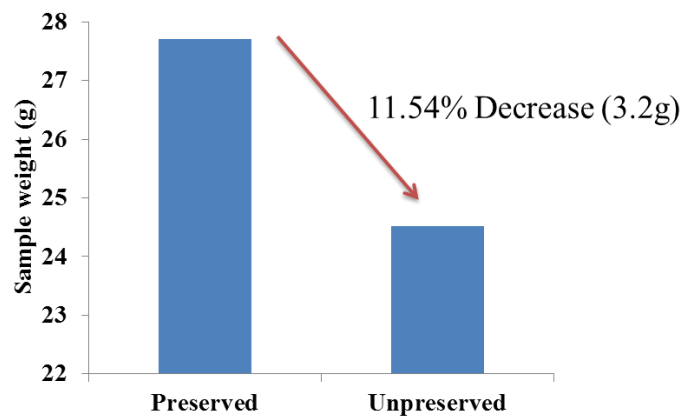


Figure 3.8: Weight change due to the drying process.

### 3.5.3 Brinell Hardness Test


The Brinell hardness test is designed to measure the hardness of a material and it is widely used in material science. The resistance of the rock to indentation has a direct correlation to rock tensile strength. The Brinell hardness test was performed by applying a measured load to an indenter that is in contact with the sample. The MS-1 multi-scale durometer by Rex Gauge (Figure 3.9) were used to measure the Brinell hardness of the

shale samples. The durometer is equipped with an adaptor for different hardness ranges. The type D scale was used to measure our sample shale’s hardness. The type D scale is the hardest scale and is designed for hard rubber and plastics (Table 3.4).



Figure 3.9: Durometer and scales for Brinell hardness test.

Table 3.4: Type D scale specification.

Indenter type	Indenter shape	Main Spring
Sharp Cone Point 30° included Angle		4536 GM, 10Lb

Before and after the drying process, Brinell hardness was measured both perpendicular and parallel to the direction of the bedding planes. Multiple readings were taken on the same surface and averaged. The average reading was then converted to the Brinell scale. The original hardness was between 309 and 316, and it decreased to between 278 and 273, a decrease of around 10% based on the original value. (Table 3.5)

Note that the unit of hardness is HBS 10/3000 (H is for hardness, B is for Brinell and S is for the steel indenter). The hardness was measured with a steel ball with a 10 mm diameter that applied a 3000 kg force on the sample. The Brinell hardness was read from the reading of the durometer.

Table 3.5: Brinell hardness change due to the drying process.

Condition	Perpendicular to bedding plane	Parallel to bedding plane
Preserved	309 (HBS 10/3000)	316 (HBS 10/3000)
Unpreserved	278 (HBS 10/3000)	273 (HBS 10/3000)
Difference	-10%	-13%

Sample hardness is widely connected to various petrophysical studies such as proppant embedment, fracture conductivity, and fluid sensitivity. If a poorly preserved sample is used for such studies, the initial hardness would be different than that for a preserved sample, and it may show different interactions with the fluid that is being tested (changes in hardness would be different).

### 3.5.4 Wave Velocity Measurement

The dynamic elastic moduli of the rock were measured. The wave velocity measurements are directly related to the dynamic elastic rock properties. P-wave transit time data are useful in identifying lithology, porosity, and pore fluids (Bumb et al. 1988). Both p and s wave velocities were measured with a pulse transmission set-up (Figure 3.10), and they were measured both perpendicular and parallel to the bedding planes by Junhao Zhou. Results are shown in Table 3.6.



Table 3.6: Wave velocity change due to the drying process.

Condition	Perpendicular to bedding plane		Parallel to bedding plane	
	$v_p$	$v_s$	$v_p$	$v_s$
Preserved	12873	6962	15340	6230
Unpreserved	10660	6822	14673	6532
Difference	-18%	-2%	-4%	+5%

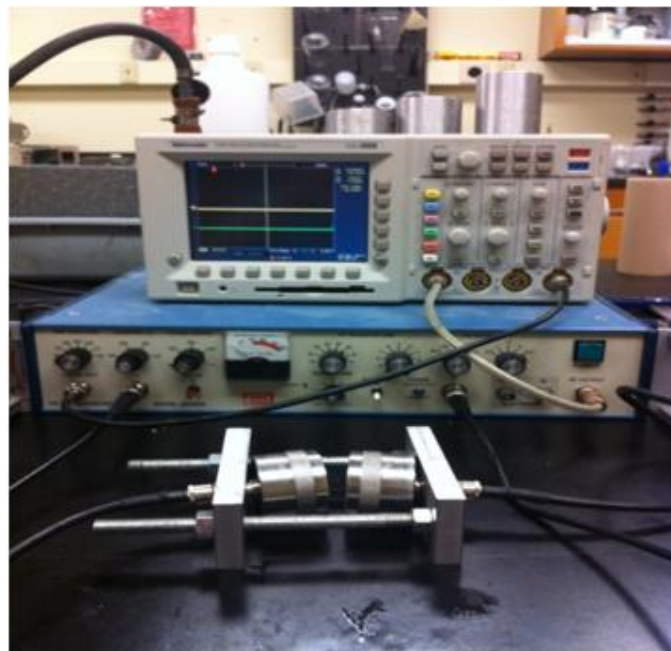


Figure 3.10: P and S wave transducers and oscilloscope to monitor the travel time.

From the data on wave velocities, the dynamic Young's modulus and Poisson's ratios were calculated using the following equations. Results are shown in Table 3.7. Both measurements are important factors for predicting the in-situ shale stresses. The p and s wave velocities are related to the elastic moduli as follows:

$$E = \frac{v_s^2 \rho \left[ 3 \left( \frac{v_p}{v_s} \right)^2 - 4 \right]}{\left[ \left( \frac{v_p}{v_s} \right)^2 - 1 \right]}, \quad \nu = \frac{1 \left[ \left( \frac{v_p}{v_s} \right)^2 - 2 \right]}{2 \left[ \left( \frac{v_p}{v_s} \right)^2 - 1 \right]}$$

Where, E is Young's modulus,  $\nu$  is Poisson's ratio,  $\rho$  is density of the shale,  $v_p$  is the p-wave velocity and  $v_s$  is the s-wave velocity.

Table 3.7: Young's modulus and Poisson's ratio results.

Condition	Young's Modulus (psi)	Poisson's ratio
Preserved	4.62E+06	0.293
Unpreserved	3.96E+06	0.153
Difference	-14%	-48%

The decrease in Young's modulus shows that the shale sample stiffness increased due to the drying process. The decrease of Poisson's ratio means the dried sample should show less lateral expansion when compressed compared to the original sample. The large change in the Poisson's ratio also implies that any in-situ stress estimates based on this Poisson's ratio would be grossly incorrect.

### 3.6 EFFECT OF PRESERVATION ON FLUID SENSITIVITY

#### 3.6.1 Swelling Behavior of Eagle Ford Shale

Because this sample of Eagle Ford shale had a low clay content, it was expected to display moderate sensitivity to water. To see how swelling affects the characteristics of the shale, the following tests were done before and after swelling of a sample that had been immersed into a 4wt% NaCl solution: a hardness test, a weight change measurement, and a wave velocity measurement.

The weight of the shale samples were measured before and after immersion into the sea water during the swelling tests. As shown in Figure 3.11, the weight change of the dried-out sample after 24 hours of immersion is about four times larger than the change of the preserved sample, meaning the dried-out sample absorbed much more liquid than the preserved sample.

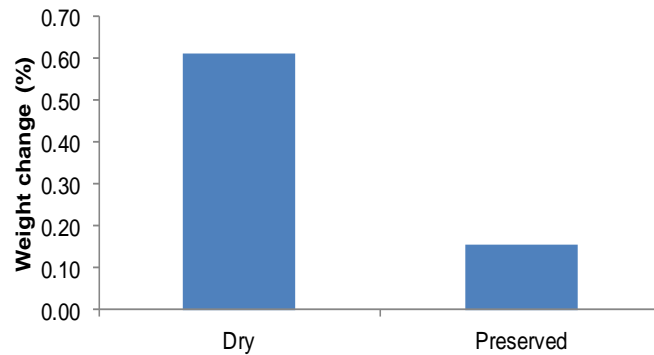


Figure 3.11: Weight change of the dry sample and the preserved sample before and after swelling with 4 wt% NaCl brine.

### 3.6.2 Brinell Hardness Test

For the purpose of investigating the fluid sensitivity of shales, the Brinell hardness was measured before and after the shales came into contact with the 4wt% NaCl solution, in both directions, parallel and perpendicular to bedding. Table 3.8 and Figure 3.12 show the change in Brinell hardness after the Eagle Ford shales were exposed to the brine.

Table 3.8: Brinell hardness change before and after swelling.

Condition	Perpendicular to bedding plane			Parallel to bedding plane		
	Before swelling	After swelling	$\Delta$ Hardness	Before swelling	After swelling	$\Delta$ Hardness
Dry	332.63	316.00	-5%	336.33	316.00	-6%
Preserved	299.25	299.25	0%	316.00	306.83	-3%

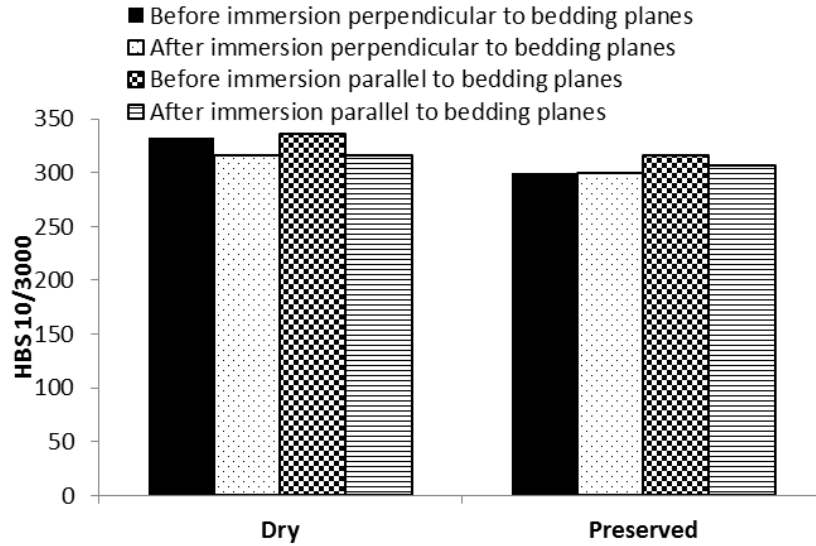


Figure 3.12: Brinell hardness of shale before and after immersion in 4wt% NaCl brine for 24 hours.

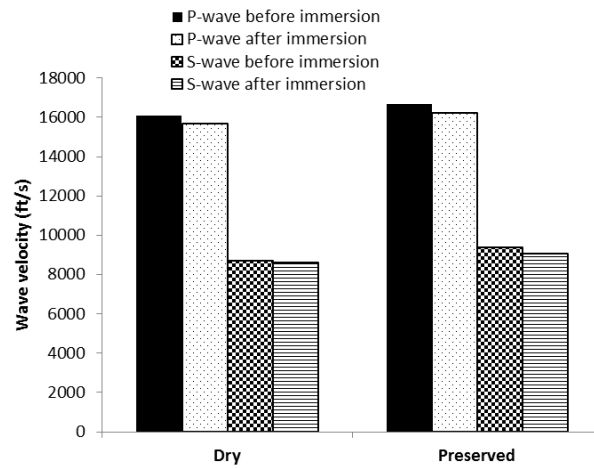
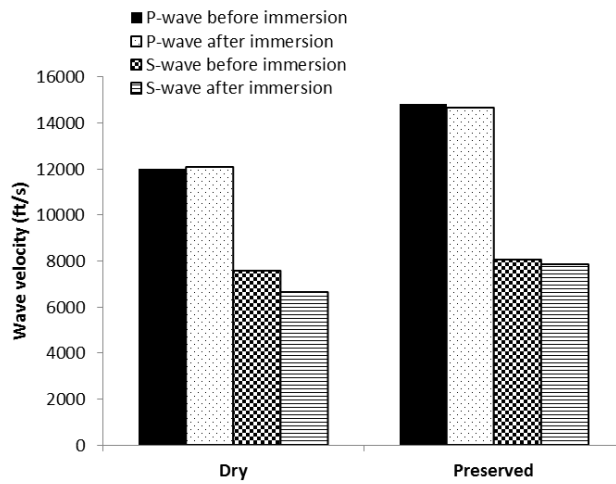
The dried-out sample showed larger changes in both directions. The hardness of the preserved sample did not change in the perpendicular direction, but it showed a 3% decrease in the parallel direction. The dry sample, however, showed a 5% decrease in the perpendicular direction and a 6% decrease in the parallel direction. This relatively small change in the hardness is directly related to the high calcite content of the Eagle Ford shale. Shales with higher clay content show larger changes in hardness after exposure to water based fluids (Wilson et al., 2014).

### 3.6.3 Wave Velocity Measurements

Wave velocities were also measured before and after immersion. Table 3.9 and Figure 3.13 show the changes in acoustic wave velocities after the Eagle Ford shales were immersed in the 4wt% NaCl brine for 24 hours.

Table 3.9: P and S wave velocities in ft/sec.

Condition	Perpendicular to bedding plane				Parallel to bedding plane			
	Before swelling		After swelling		Before swelling		After swelling	
	P-wave	S-wave	P-wave	S-wave	P-wave	S-wave	P-wave	S-wave
Dry	12016	7584	12076	6647	16090	8715	15672	8620
Preserved	14839	8064	14655	7852	16686	9390	16241	9084



(a)

(b)

Figure 3.13: Brinell hardness of shale before and after immersion in 4wt% NaCl brine for 24 hours. a) Perpendicular to bedding plane, b) parallel to the bedding plane.

Table 3.9 and Figure 3.14 show the Young's modulus and Poisson's ratio calculated from the wave velocity results. Both results showed that dry samples' ratios are significantly different than the ratios of the preserved samples. For Young's modulus, the preserved sample changed by only 3%, but the dry sample changed by 15%, making it five times larger than the value of the preserved sample. Moreover, there was a large difference between the results of the Poisson's ratios of the samples. The ratio of the dry sample increased 67%, and it was twenty-two times larger than the value of the preserved sample. For both Young's modulus and Poisson's ratio results, the preserved sample showed only 3% change which was in the error range, so the sample was not sensitive when contacted by NaCl brine. However, the dried-out sample showed very large changes in both moduli. This shows that the dried-out sample was artificially made water sensitive due to drying, a property which the preserved sample did not have.

Table 3.9: Changes in Young's modulus and Poisson's ratio.

Condition	Young's Modulus (psi)			Poisson's ratio		
	Before swelling	After swelling	Change (%)	Before swelling	After swelling	Change (%)
Dry	4.47E+06	3.81E+06	-15	0.169	0.283	67
Preserved	5.46E+06	5.30E+06	-3	0.290	0.299	3

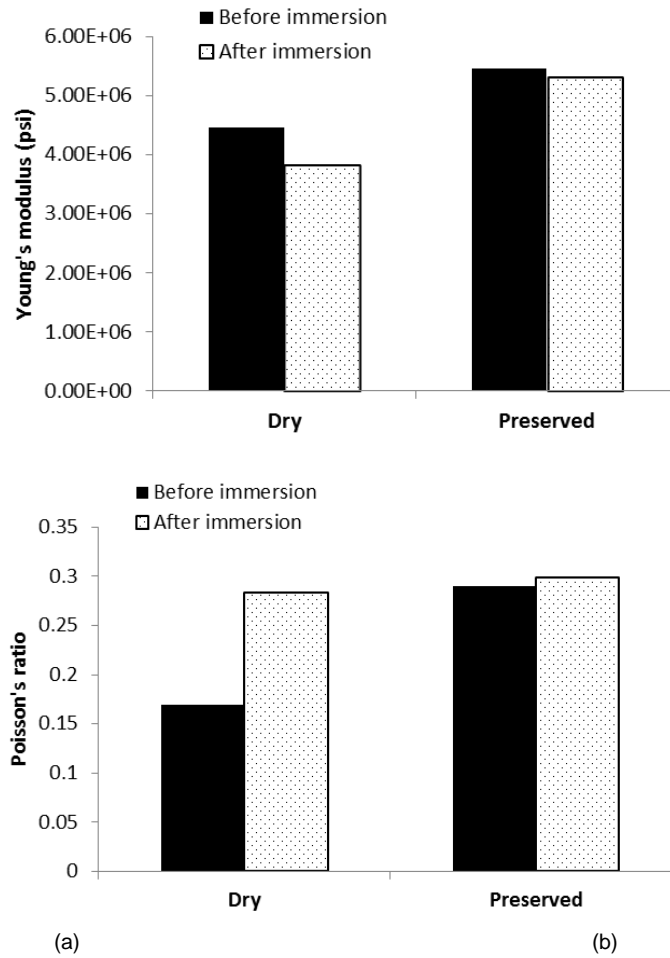


Figure 3.14: (a) Young's modulus change and (b) Poisson's ratio change of dry and preserved samples when exposed to 4% brine.

### 3.6.4 Permeability Measurement: Pressure Penetration Method

A pressure penetration technique (PPT) was used to measure the brine and gas permeability of shale samples in contact with the 4wt% NaCl brine. The experimental set-up consisted of several devices used to achieve a continuous flow of test fluid across the top face of the shale sample at a constant pressure. In a small sealed chamber beneath

the shale, the fluid pressure build-up was recorded as the test progressed. The rate of pressure build-up provided a quantitative value of shale permeability (Cai et al. 2012; Sharma et al. 2012; Ji et al. 2012). Figure 3.15 shows a schematic of the experimental set-up for the pressure penetration test, and Figure 3.16 shows the schematic diagram of the main cell assembly.

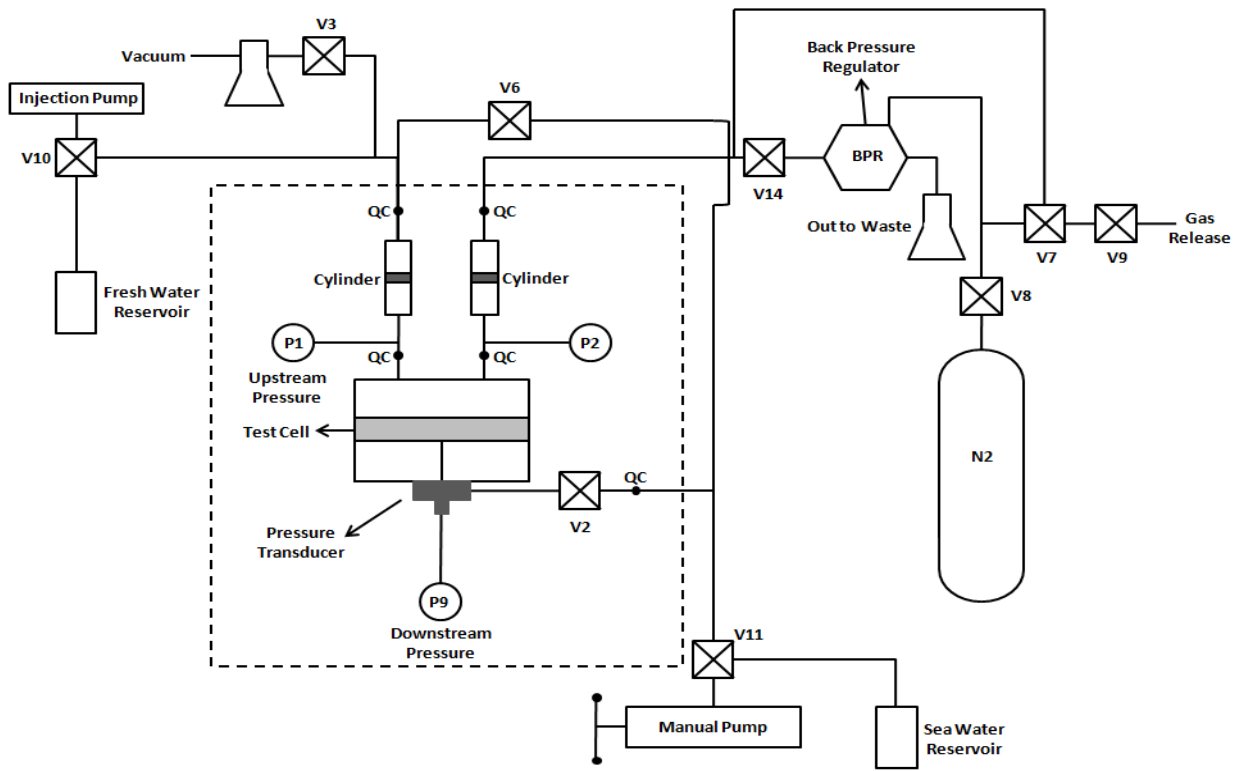


Figure 3.15: Pressure penetration test set-up.



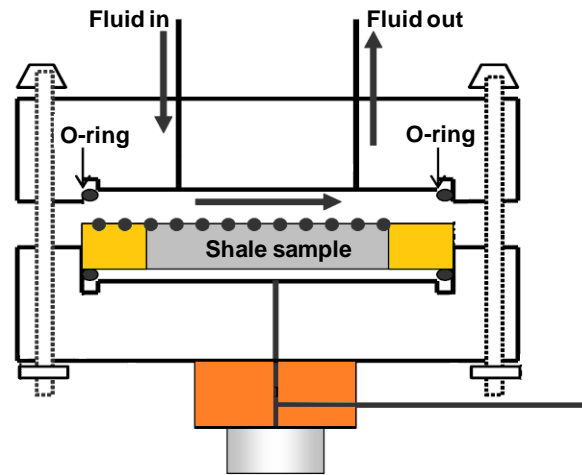


Figure 3.16: A schematic diagram of the main cell assembly.

The permeability of the shale to 4 wt% NaCl brine was measured with both preserved and dried-out samples. Figure 3.17 and Figure 3.18 show the pressure buildup graphs of two tests performed. The top narrow blue line is the upstream pressure, and the bottom narrow green line and thick red line are the downstream pressure. The early time portion, bottom thick red line part, of the downstream pressure was used to calculate the brine permeability. The brine permeability of the preserved sample was 183nD under 170psi effective stress, and it was three times larger than the permeability of the dry sample which was 68nD under 80psi effective stress. The dried out sample has air in the pore space, causing two-phase flow in the pores (for the dried out sample). This causes the water relative permeability to be lower than the single phase brine permeability (for the preserved sample). In addition, clays have shrunk in volume thereby decreasing the pore space open to sea water flow and the permeability.

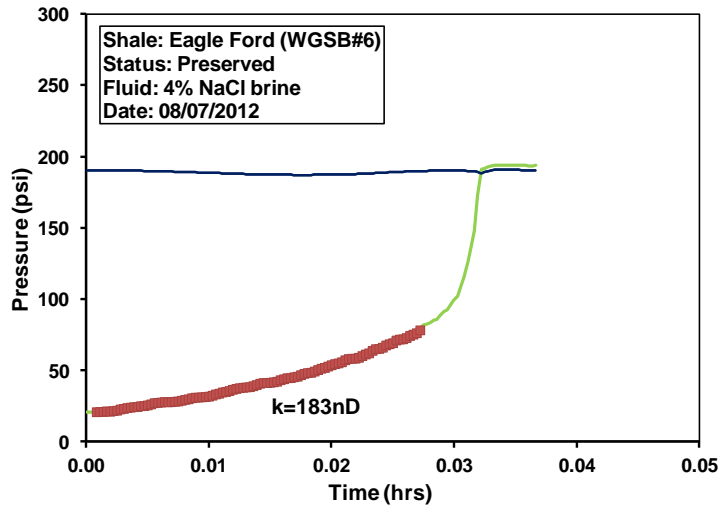


Figure 3.17: Brine permeability results for a preserved Eagle Ford shale sample from pressure penetration tests.

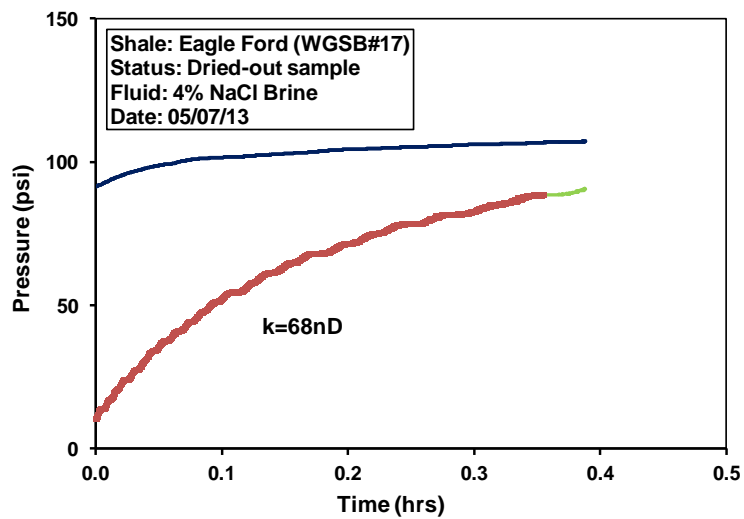


Figure 3.18: Brine permeability results for a dried-out, unpreserved, Eagle Ford shale sample using a pressure penetration test.

### 3.6.5 Permeability Measurement: GRI Method

Shale permeability was also measured using nitrogen with a dried-out sample using the PPT method and the Gas Research Institute (GRI) method. Weatherford

laboratory measured the nitrogen permeability of a dried-out sample using the GRI method.

The GRI method is the most common technique to measure the permeability of unconventional reservoir samples. This technique was originally developed by Luffel et al. in 1993 to measure the extremely low permeability of a Devonian shale. The conventional steady-state or pulse decay methods were not appropriate for measuring these low permeabilities because it took such a long time to measure the permeability. GRI-method is much faster than the steady-state method or the pulse decay method because it uses crushed-rock samples which have a larger contact surface. For the GRI method, the shale sample is crushed and sieved to 0.67mm diameter particles. During these procedures, the in-situ fluid is expected to evaporate and fractures, and cracks are induced in the sample by the crushing process (Sinha et al, 2012). Because gas is used for measuring the shale permeability, the GRI method yields an effective gas permeability,  $k_g$ , which is often referred to as matrix permeability,  $k_m$ . This is a misnomer since the permeability reflects the permeability of the matrix as modified by the induced fractures in it.

The crushed particles are stored in the sample cell (Figure 3.19). Using a pressure regulator, the reference volume of 22 cc is filled with nitrogen and the pressure change during gas expansion from the reference volume to the sample cell is monitored. Using the pressure data, the gas permeability of the shale sample is calculated (Tinni et al., 2012).

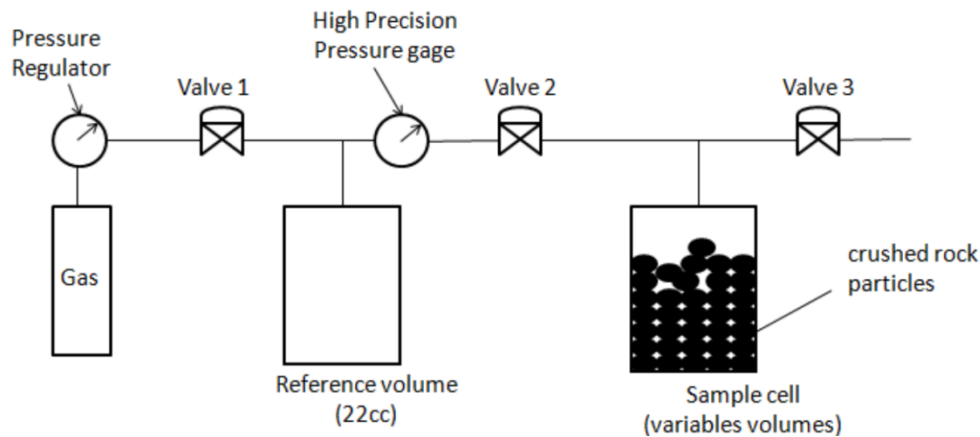


Figure 3.19: Schematic of apparatus used for GRI permeability measurement (Tinni et al., 2012).

Figure 3.20 shows the pressure buildup graph of the PPT test. The nitrogen permeability of the dried sample was measured to be 52nD. For the GRI method, a cylinder type sample which is 3.8cm in diameter with a length of 4cm was used. The nitrogen permeability was measured to be 22 $\mu$ D using the GRI method. This is 400 times larger than our PPT test result.

There can be many reasons for the differences in the two results. Perhaps the most likely is the introduction of cracks in the GRI method sample, the crushing and removal of water can result in additional small cracks that make the smaller sample size more susceptible to fluid movement. The PPT test used the preserved core itself without modifying its original structure, while the GRI method used the crushed shale sample. The GRI method reflects the matrix permeability as modified by the presence of cracks in the sample while the PPT method measures the matrix permeability. Sample preparation in the GRI method is a key to reproducibility. The PPT method is less susceptible to variations due to sample preparation.

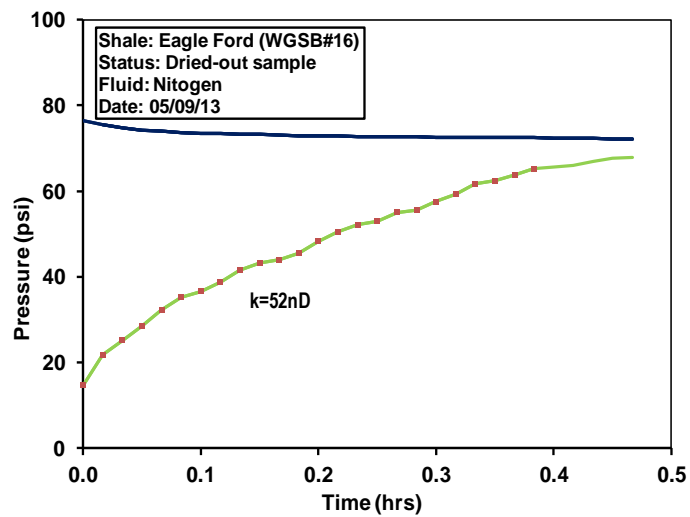


Figure 3.20: Nitrogen permeability results of dried-out sample from pressure penetration tests

### 3.7 CONCLUSIONS

Table 3.10 and 3.11 show a summary of the test results presented in this chapter. They clearly show the differences between preserved samples and results of un-preserved (dried) samples. These results indicate that measurements such as weight change, hardness, wave velocity and permeability need a carefully prescribed sample preparation protocol using preserved samples to yield reliable and reproducible results.

Table 3.10: Summary of mechanical properties from test results for Eagle Ford shale (25% clay).

Properties		Preserved	Unpreserved	Difference
Porosity		1.8%	4.9%	+172%
Weight Change		27.8g	24.6g	-11.54%
Hardness	Perpendicular	309	278	-10%
	Parallel	316	273	-13%
Young's modulus		4.62E+06	3.96E+06	-14%
Poisson's ratio		0.293	0.153	-48%

Table 3.11: Summary of fluid sensitivity test results for Eagle Ford shale (25% clay).

Properties		Preserved sample	Dried-out sample	Difference
Weight Change		0.61%	0.16%	4 times
Hardness	perpendicular to bedding	0%	-5%	5 times
	parallel to bedding	-3%	-6%	2 times
Young's modulus		-3%	-15%	5 times
Poisson's ratio		3%	67%	22 times
Sea water permeability		183nD	68nD	3 times

To preserve the core sample in the original state, the humidity of the chamber in which the samples are stored must be controlled. Strippable plastic or wax coating must be used in the field for sealing the core when it is obtained in the field. This coating is accomplished by dipping the core in a wax bath, and using special formulated wax for core encapsulation (Baker Hughes Incorporated, 2010). This prevents desiccation of the core (water from exiting the core). After the core has arrived at the lab, its original water activity should be measured. Then, samples can be kept in the proper desiccators, as discussed previously in this chapter. After removing the core from its stored state, it should be immersed in oil so as to preserve the shale and maintain its saturation condition. Most shale cores and samples can be kept in a sealed steel can immersed in oil, and this does not affect their original water activities and it maintains its original saturation condition (Chenevert and Amanullah, 2001).

## **Chapter 4: Interaction of Fracturing Fluids with Organic-Rich Shales**

### **4.1 INTRODUCTION**

Hydraulic fracturing is a widely used stimulation tool in low-permeability reservoirs. It can improve the performance of reservoirs, making them economically attractive (Sharma et al., 2004). To improve the effectiveness of hydraulic fracturing, many studies have been performed to develop better fracturing fluids. Such fluids should provide good proppant carrying capability, yield sufficient fracture width and the desired net pressure, be environmentally friendly, be cost effective, and have formation compatibility and controllable fluid loss (Montgomery et al., 2013). Oil-based fluids, water-based fluids, acid-based fluids, cross-linked gels, and foam fluids were developed to fulfill these requirements, and they are currently used in hydraulic fracturing (Kamel et al., 2009). Although various fracturing fluids are used in the oil field, the most commonly used fracturing fluid is slick water, a combination of water and friction reducer. Slick-water fracturing uses low concentrations of polymers and a low concentration of proppant, so it effectively reduces the treatment costs (Ely et al., 2014).

Most fracturing fluid studies are focused on fracture conductivity, proppant embedment, proppant settling, and flow behavior. Montgomery (2013) presented many studies of fracturing fluids and their components. However, relatively few studies have been conducted on the interaction between fracturing fluids and shale surfaces and how these fluids affect the petrophysical properties of shale.

This chapter presents an experimental study to determine and quantify how much permeability change occurs when a shale interacts with slick water solutions.



Experimental data is presented to show the how the permeability of shales is changed due to interaction with a fracturing fluid.

## **4.2 EXPERIMENTAL METHODS AND TRANSIENT PRESSURE MODEL**

From among various petrophysical properties, I chose to focus on the permeability change caused by contact with the fracturing fluid. The Pressure Penetration Technique (PPT) was used to measure the fluid permeability of shale, and to study the effect of fracturing fluid interaction on permeability. First I measured the shale permeability with 4 weight % NaCl brine as a reference permeability, then I injected fracturing fluid for 10 hours to offer enough interaction time with shale, and then I measured brine permeability again to observe the change in permeability.

### **4.2.1 Experimental Set-up: Pressure Penetration Technique (PPT)**

Figure 4.1 shows the schematic experimental set-up for the pressure penetration test. The experimental set-up consists of several devices used to achieve a continuous flow of the test fluid across the top face of the shale sample. At a constant upstream pressure, a test fluid was flowed across the top of a shale sample. In a small sealed chamber beneath the shale sample, on the downstream side, the fluid pressure build-up was recorded.

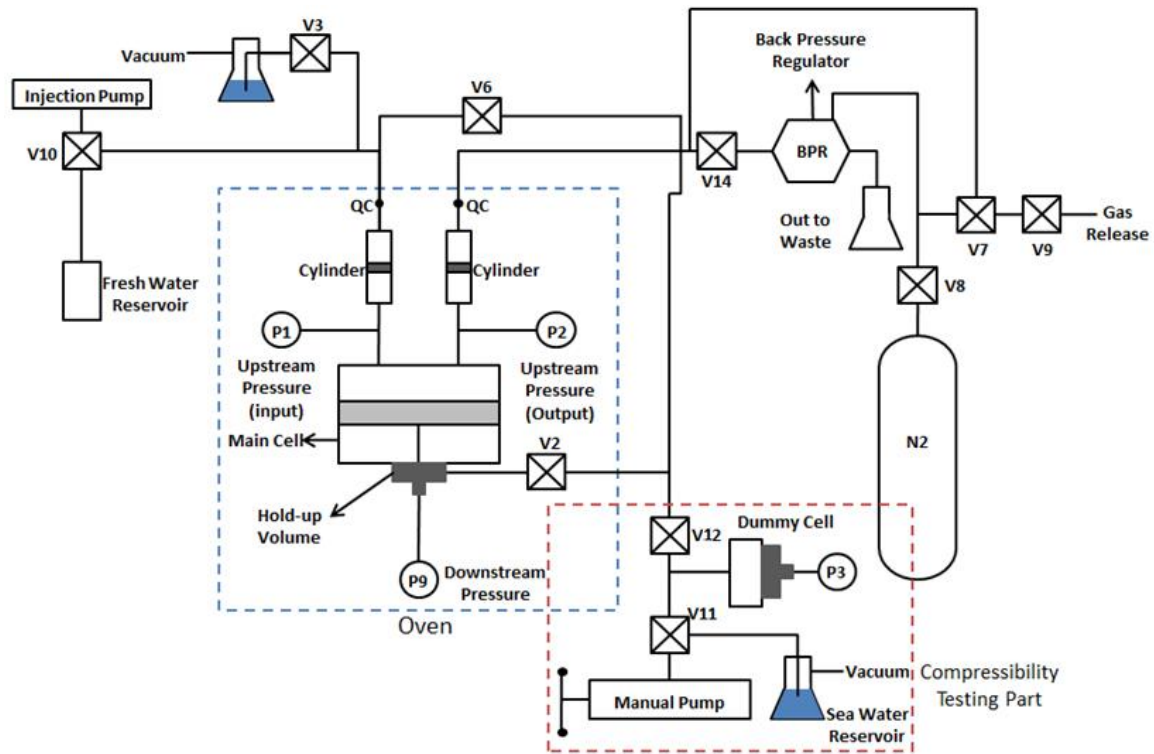


Figure 4.1: Schematic of pressure penetration test and compressibility test set-up.

Figure 4.2 shows two photographs of the PPT set-up. To prevent temperature changes in the lab from affecting the results, the cell and all important fluid lines and connectors are installed inside an oven. During the experiment, the door of the oven was closed and the experiment was performed at constant temperature. There are two cylinders within the oven: the upper cylinder is a test fluid cylinder, and the lower one is a waste fluid cylinder. Both cylinders have a floating piston inside to separate the pump fluid from the test fluid. From the injection syringe pump, fresh water was injected into the test fluid cylinder. The injected fresh water pushes the piston inside the cylinder. The test fluid is then moved by the piston, and the fluid flows into the main test cell and contacts the shale sample. At first, the injection pressure is not high enough to overcome the capillary pressure of the shale, so all the fluid passed across the shale surface into the

waste cylinder. As the test fluid is injected into the waste cylinder, the piston inside the waste cylinder moves, and it pressurizes the back pressure regulator (BPR) which opens when the pressure exceeds a certain pre-set pressure. The BPR controls the upstream pressure, and the pressure can be set with a nitrogen tank. If the outflow pressure is higher than the BPR setting, the waste fresh water comes out from the waste cylinder and is collected in a beaker. This maintains the BPR set-pressure. When the upstream pressure exceeds the capillary entry pressure of the shale, the test fluid starts to flow through the shale sample. Because the volume hold-up beneath the cell is fixed (V2 is closed) and filled with brine, there is no empty volume for the penetrating fluid to enter. For this reason, the downstream pressure (P9) increases as the test fluid penetrates the sample. The shale permeability can be estimated by recording this downstream pressure vs time.



Figure 4.2: Pressure penetration test set-up.

#### 4.2.2 Transient Pressure Model for Unsteady State Flow

The PPT test is referred to as an unsteady-state method for measuring permeability. A transient pressure model was used for calculating the sample permeability (Al-Bazali et al, 2006).

$$\ln\left(\frac{P_2 - P_1}{P_2 - P_0}\right) = -\frac{Ak}{\mu cVL}t \quad \rightarrow \quad k = -\left[\frac{\ln\left(\frac{P_2 - P_1}{P_2 - P_0}\right)}{t}\right] \frac{\mu cVL}{A} = -(slope) \times \frac{\mu cVL}{A}$$

where:

$P_2$ : upstream driving pressure,	$P_1$ : downstream build-up pressure
$P_0$ : downstream initial pressure,	$A$ : sample cross sectional area
$k$ : permeability,	$\mu$ : viscosity
$c$ : compressibility factor,	$V$ : beneath sealed chamber volume
$L$ : sample thickness,	$t$ : time

The dimensions of the sample, testing fluid viscosity, and upstream and downstream pressure data were known values. The unknowns were the compressibility factor and volume of the fluid beneath the sealed chamber.

Figure 4.1 shows the compressibility testing part of the PPT set-up. To measure the compressibility of brine in the bottom chamber, a dummy cell with a pressure transducer was attached for the compressibility testing. The system pressure was increased using a manual hand pump. Figure 4.3 shows the compressibility testing result. Using the pressure versus injected volume data and the equation presented below, the average compressibility of our system can be calculated.

$$c = -\frac{1}{V} \times \frac{(V_1 - V_2)}{(P_1 - P_2)} = -\frac{1}{V} \times \frac{1}{(slope)}$$

where:

$c$  : compressibility,

$V_1$  : initial volume,

$P_1$  : initial pressure,

$Slope$  : slope of Figure 4.3

$V$  : reference volume,

$V_2$  : final volume

$P_2$  : final pressure

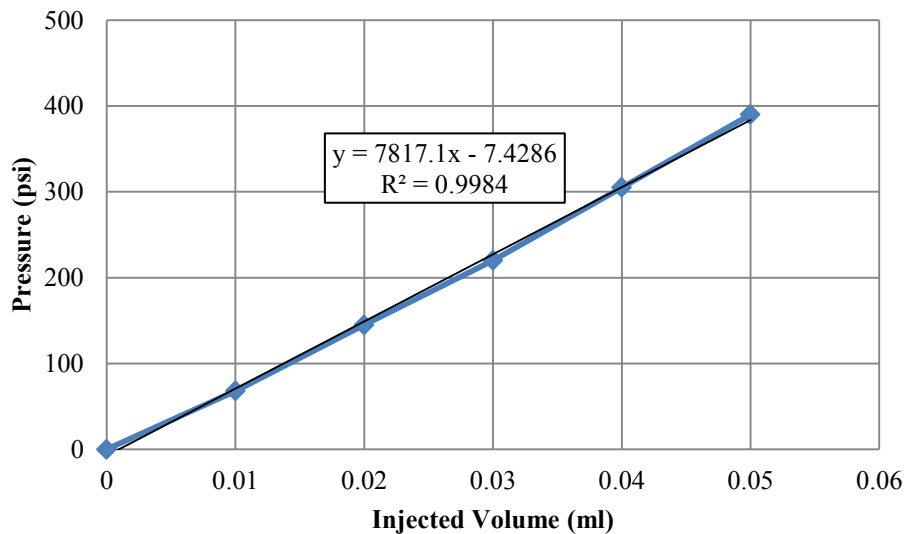


Figure 4.3: Brine compressibility test result and compressibility calculation equation.

Our result,  $1.87 \times 10^{-5}$ /psi, is about 5 times higher than the handbook-reported brine compressibility, which is  $3.17 \times 10^{-6}$ /psi. This is because the compressibility of our system does not solely depend on brine but also on the whole physical system such as the flow lines, pressure transducers and valves. Previous students who had used this PPT set-up did not consider the system compressibility, so their permeability results were much smaller than the fractured permeability.

To measure the hold-up volume beneath the shale sample, a similar approach was used as that used for the compressibility measurement. The downstream section is divided into two different sections. (Figure 4.4) When valve 2 was closed, the remaining downstream section, excluding hold-up volume, was called the closed system volume.

And when valve 2 was opened, the hold-up volume was then connected to the other downstream section; this is the open system volume.

The hold-up volume measurement procedures are performed as follows. First, the downstream system was vacuum evacuated, so that there was no air and fluid present in the downstream system. Next, we closed valve 2, valve 11, valve 6, and the dummy cell connection, and we increased the closed system pressure with a manual pump. We then plotted the injection fluid volume versus the closed system pressure. (Figure 4.5) Next we released the pressure on the manual pump and opened valve 2. We then increased the pressure of the open system volume using the manual pump. At this time, the hold-up volume remained empty; the system pressure increased only after a short interval, while the hold-up volume was filled with brine. Then the system pressure was increased as same as the tendency of the closed system. Thus, the injection fluid volume from the manual pump during the short interval was the same as the hold-up volume, 2.35 ml. (Figure 4.4).

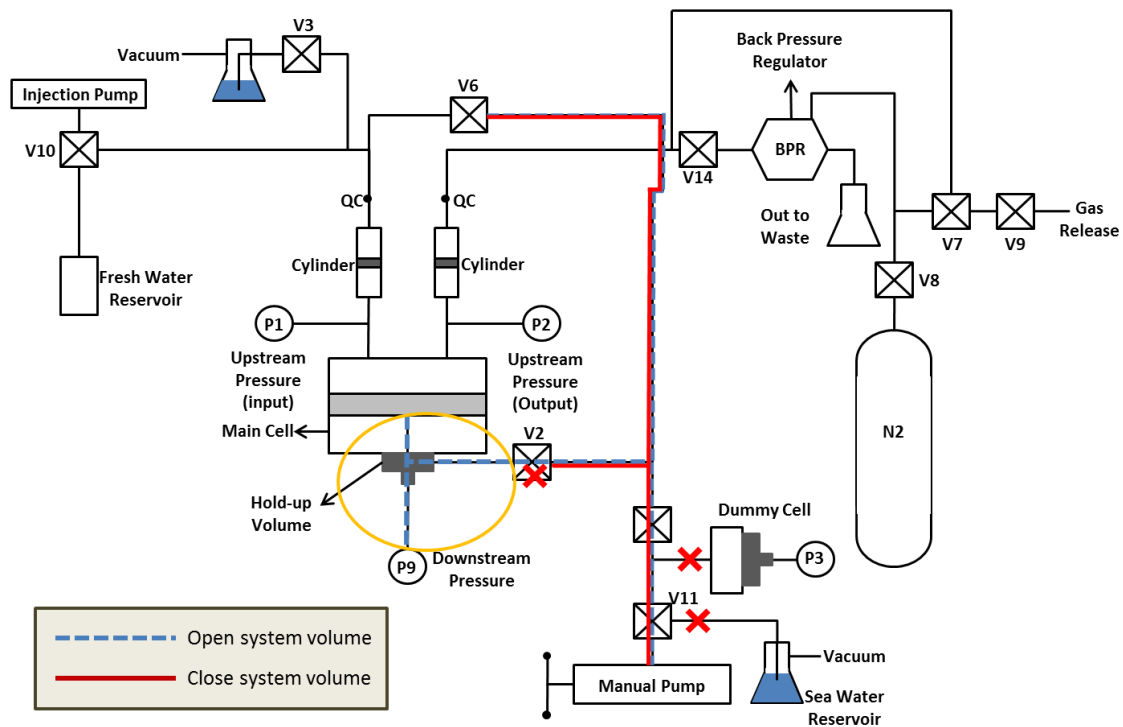


Figure 4.4: Open system volume (dotted blue line), closed system volume (red solid line), and hold-up volume (blue dotted line covered by orange circle) for hold-up volume measurement

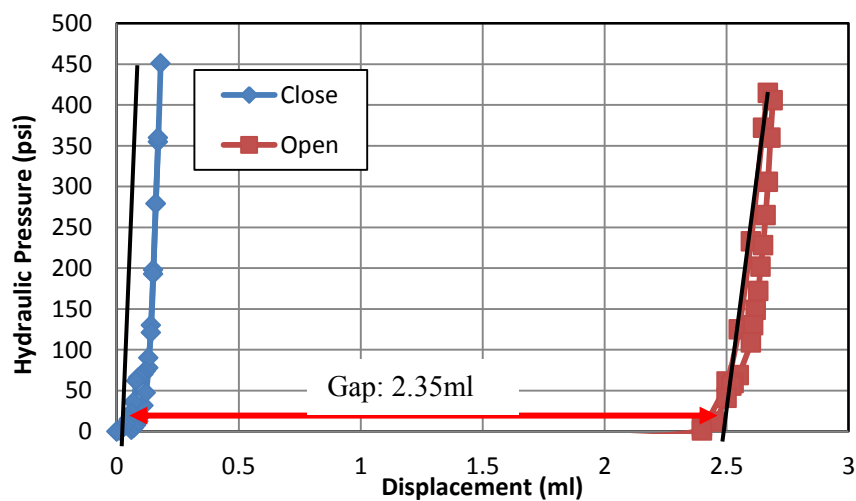


Figure 4.5: Displacement vs. pressure build up for open and closed cases

Now, every essential value for the experimental setup is known, and the shale fluid permeability can be calculated very precisely. Figure 4.6 shows the downstream pressure build-up result, and Figure 4.7 shows the graph of dimensionless pressure versus time. This graph was used in the transient pressure model. The slope of the thick line part of the plot is used to calculate the permeability. However, it is evident from the graphs that in some cases the slope is not constant. As can be seen in Figure 4.7, the slope of line at late time is higher than the slope of the line at early time. This implies that the permeability of this sample is not constant during this test, but rather increases during the test. When shale interacts with water, water uptake and ion gain/loss is expected to occur (Chenevert, 1989 and Zhang et al., 2004). Due to these interactions, the permeability can change during the fluid injection through the shale samples. The sensitivity and magnitude of permeability change are different for every sample. For some samples, the change is not big, so the slope is relatively constant, and only one permeability result is recorded for this case. For some cases, the slope changes very fast, and in these cases the experimental results should be divided into several sections, and then there can be more than one value of permeability recorded for the sections.

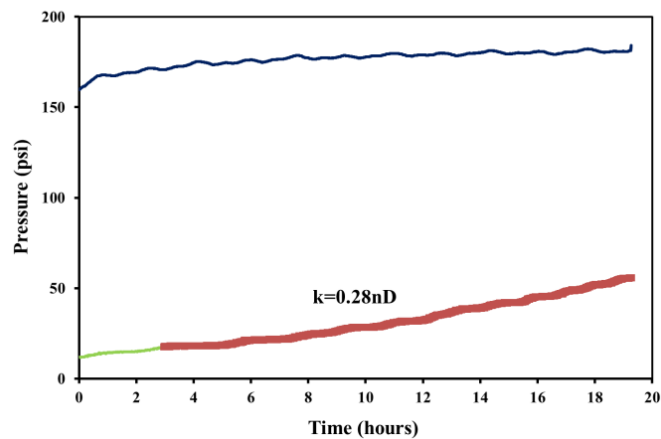


Figure 4.6: Downstream pressure build-up test result.



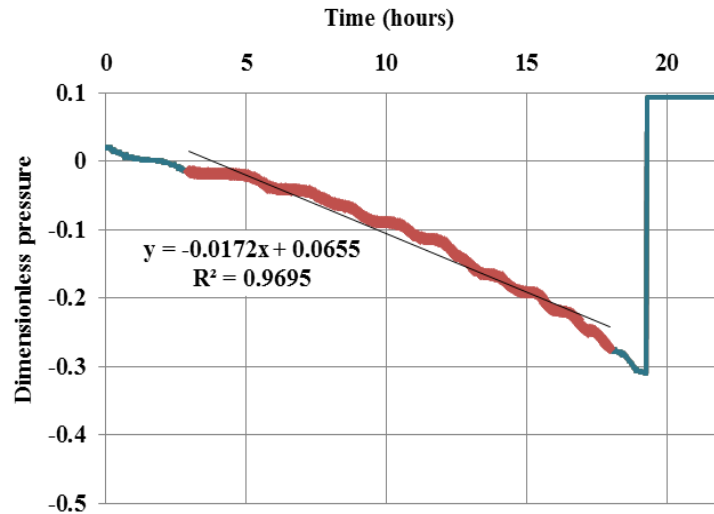


Figure 4.7: Graphical slope interpretation of dimensionless pressure versus time.

#### 4.2.3 Leakage Test after the Permeability Measurement

The permeability of shale is in the nano-Darcy range. Any leakage is critical for the permeability measurement. There were many trials to eliminate the system leakage as much as possible, but it was impossible to eliminate the leakage entirely. To account for this uncertainty, the leakage rate was measured and compared with the flow rate through the shale (used for obtaining the permeability results). If the leakage rate was in an acceptable range (leading to a less than 0.1nD correction in permeability), the rate was applied to the permeability results and used to correct the original value.

The leakage rate was measured after each permeability test as follows. When the permeability measurement was finished, both upstream pressure (P1 and P2) are the same, and the downstream pressure (P9) is similar to or smaller than the upstream pressure. Open V2 and increase the downstream pressure to be the same as the upstream pressure, and then close V2. After that, close V1 and V5, monitor the pressure change of

P1, P2, and P9. Because no fluid was injected and escaped from the closed system, the pressure should not decrease. If pressure was decreased, it is because of leakage, and the rate was recorded and subtracted the amount from the original permeability results (Figure 4.8).

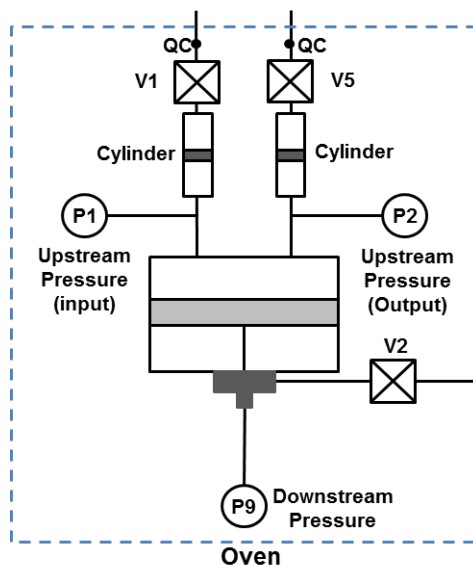


Figure 4.8: Leakage test to monitor the rate of leakage from the test cell.

#### 4.2.4 Sample Preparation

Utica shale core samples, which are 5 inches in diameter and 7 inches long, were used in these experiments. The mineralogical data were obtained from XRD measurements. (Table 4.1)

Table 4.1: XRD mineralogy test results, Utica shales.

Quartz	K-Feldspar	Plagioclase	Calcite	Ankerite/ Fe-dolomite	Dolomite	Pyrite	Illite/ Smectite	Illite + Mica	Chlorite	Total clay
23	2	4	24	3	3	2	10	18	9	38

Rectangular shale samples ( $1\frac{1}{4}$  inches long x  $1\frac{1}{4}$  wide x 6 inches high) were prepared for the permeability test. To eliminate any reaction with moisture during the coring process, an oil-cooled coring machine was used to cut the shale (Figure 4.9).

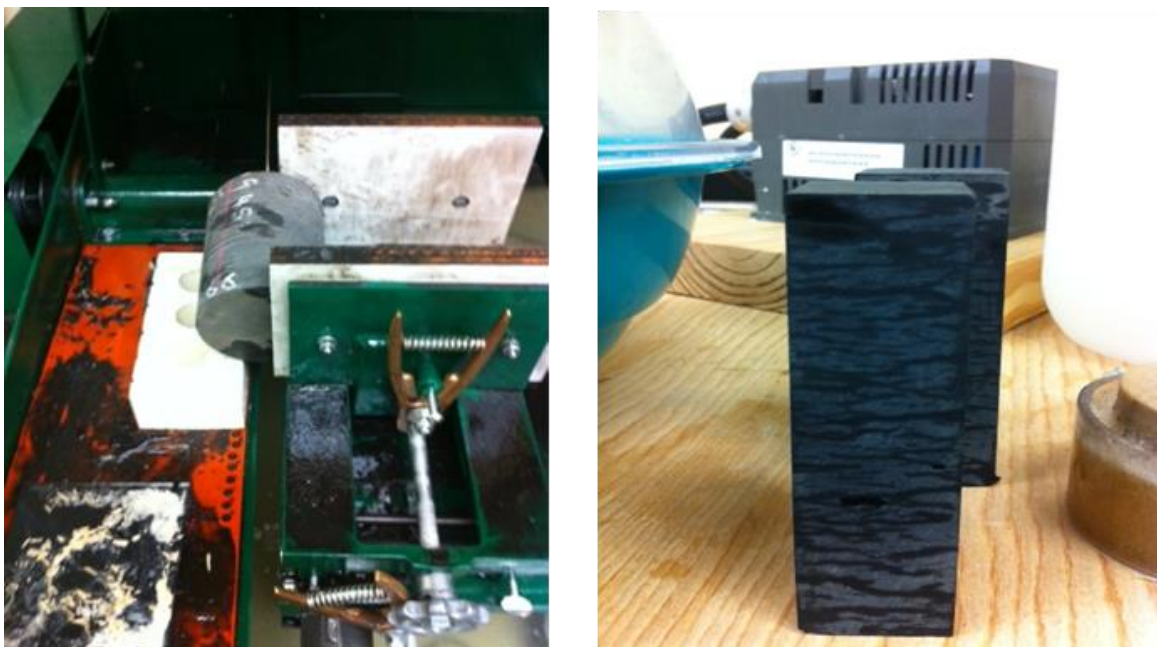


Figure 4.9: Oil-cooled saw (left) and prepared rectangular shale core samples (right).

Four rectangular samples were obtained from one core. They were wiped with a paper towel and flushed with hexane to remove the cutting oil from the rock surface. A rectangular sample was attached to a bottom plastic block using 5-minute glue and covered with a 2.5-inch ID plastic cylinder. Then mix epoxy resin (Momentive EPON Resin 828) and a curing agent (Momentive Epikure 3140) obtained from the Miller-Stephenson Chemical Company in a ratio of 1:1. The mixture was poured into the cylinder to seal the shale and to allow the preparation of a  $\frac{1}{4}$ -inch disk type sample. It takes about 10 days for the epoxy to harden sufficiently (Figure 4.10).



Figure 4.10: Epoxy resin encapsulating the shale core.

After the epoxy hardened, the samples were cut with an oil-cooled saw into ¼-inch disks and preserved in a controlled humidity desiccator that contained a specific saturated salt solution (Figure 4.11). These samples were kept in the desiccator to maintain the original water saturation of the shale. With a properly saturated salt solution in the bottom of the desiccator, the air humidity remains constant inside the desiccator, and the water saturation of the shale also stays constant. Our laboratory houses nine desiccators with humidity conditions ranging from 0.1 to 0.98. In this Utica shale experiment, the controlled humidity was 64% ( $A_w = 0.64$ ) (Figure 4.12).



Figure 4.11: Sliced disk type sample (left) and a desiccator containing properly saturated salt (right).

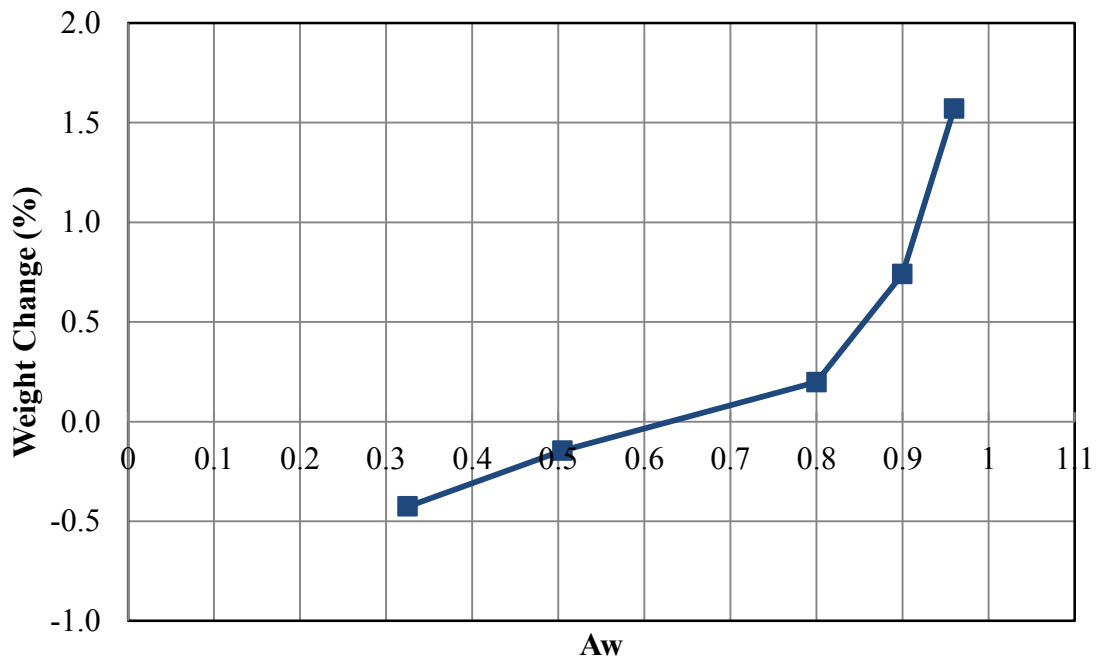


Figure 4.12: Original water activity results, Utica shale.

### 4.3 EXPERIMENTAL RESULTS

Three permeability tests were performed on the Utica shale sample (HUT-10). First, a 4 weight percent seawater solution was injected. The upstream pressure was set at 110 psi, and the downstream pressure was set at 20 psi, producing a 90 psi differential pressure between upstream and downstream. The brine permeability of the sample was 272 nD (Figure 4.13). After each permeability measurement, a leakage test was performed to determine the effect of leakage. The leakage effect slightly increased the original permeability value, and 272 nD is the permeability that was obtained after being corrected for leakage.

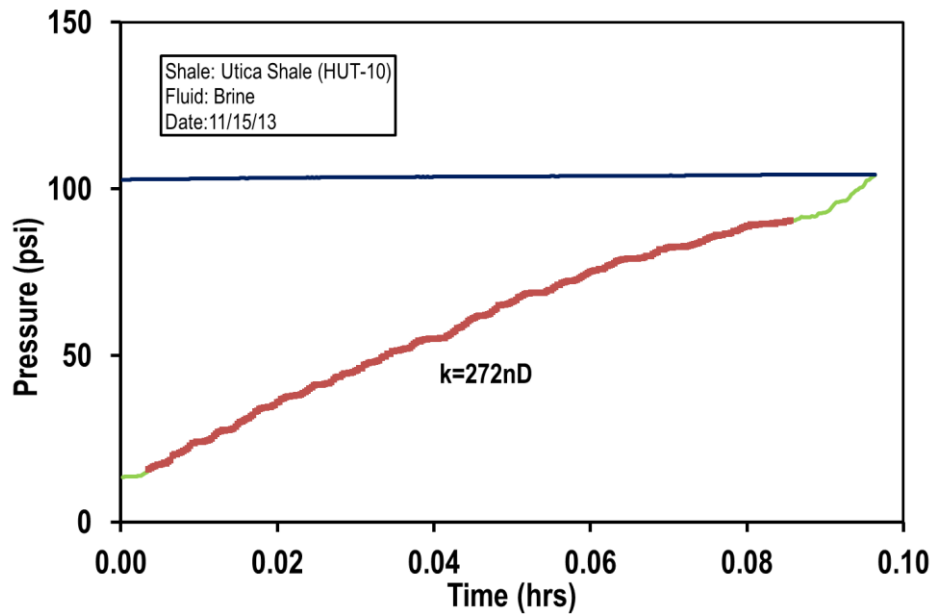


Figure 4.13: Brine permeability measurement, HUT-10 sample.

After the brine permeability test, the initial slick water permeability was measured. The slick water composition is a mixture of 1% polyacrylamide and 99% sea water, which is a 4 weight percent sea salt and deionized (DI) water solution. Polyacrylamide is widely used as a friction reducer, and the Flojet DR7000 product from SNF, Inc., was chosen here because of its good compatibility with both water and brine solutions. Before the permeability measurement, the viscosity of the slick water was measured using a rheometer (ARES-LS1, TA Instruments) with the double-wall Couette geometry. Figure 4.14 shows the viscosity results. The slick water is a shear thinning fluid and has higher viscosity compared to the pure brine.

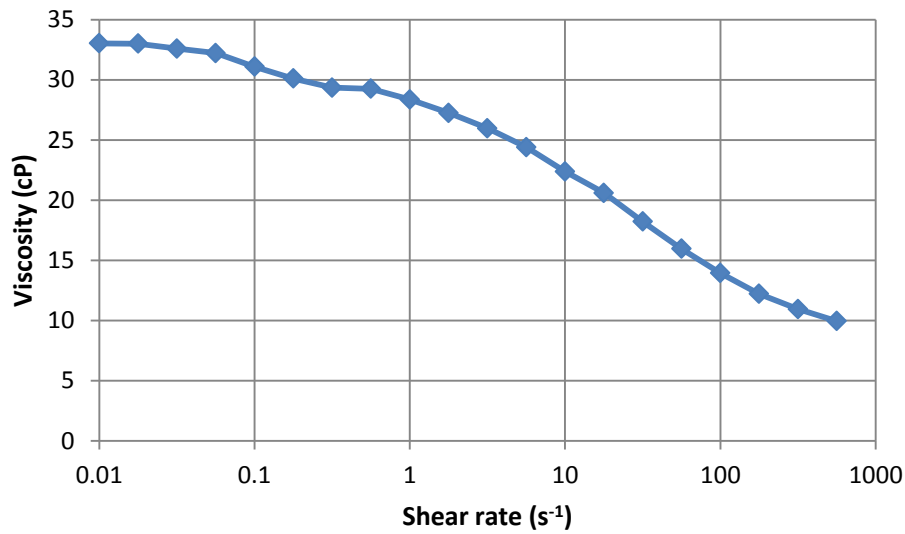


Figure 4.14: Viscosity measurement versus increasing shear rate.

During the PPT test, the pressure difference was maintained at 90 psi, which was the same as in the previous brine test. The slick water permeability was measured to be 6.4nD, much lower than the brine permeability (Figure 4.15).

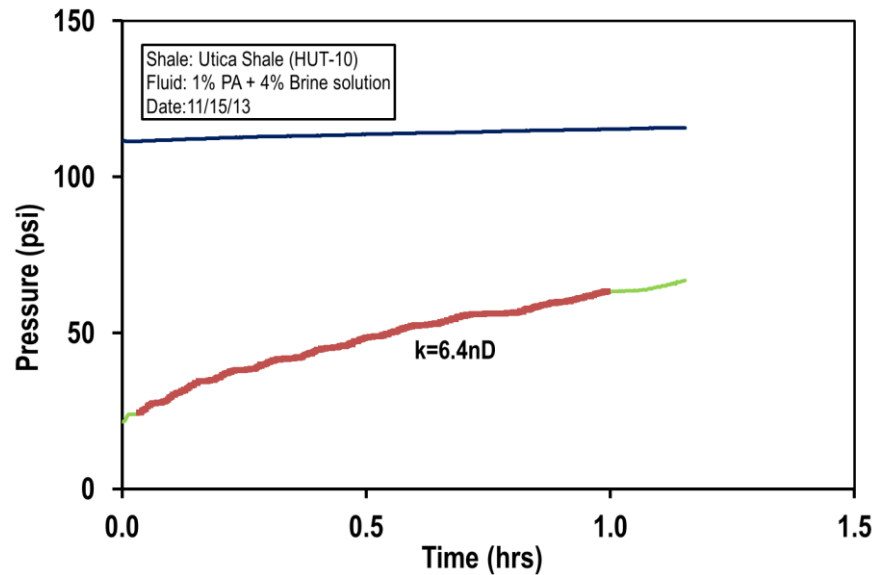


Figure 4.15: Initial slick water permeability measurement, HUT-10 sample.

After the initial slick water permeability was measured, slick water was injected continuously into the shale sample for 12 hours, and the sample was kept inside the main cell to be contacted by slick water. After the injection, another brine permeability test was performed to determine the effect of slick water injection on the brine permeability. The pressure difference was 140 psi at this time, and the final brine permeability was 8.5 nD. This value was similar to the initial slick water permeability value, and it was much lower than the original brine permeability. This means that slick water injection reduces the permeability of shale by a factor of about 20 (Figure 4.16).

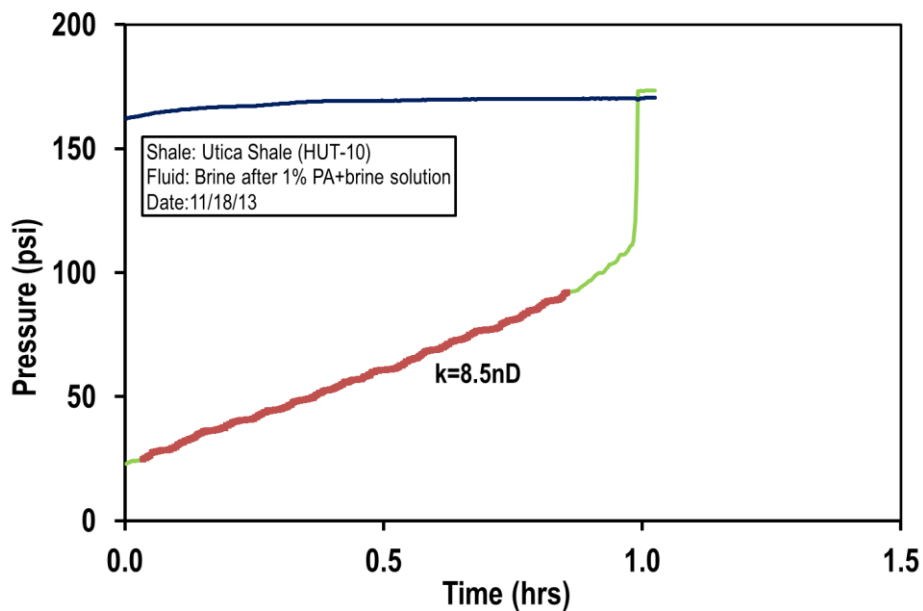


Figure 4.16: Additional brine permeability measurement, HUT-10 sample.



Another Utica shale sample (HUT-12) was tested with brine and slick water. (Figure 4.17) With a 110 psi pressure difference, the brine permeability was only 5 nD, which was much lower than that of the previous sample. After this brine test, a crack developed in the sample.

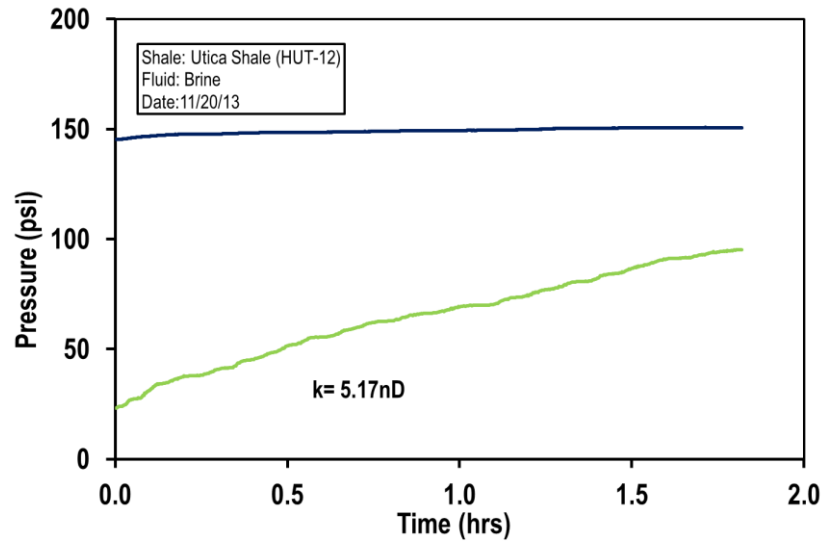


Figure 4.17: Initial brine permeability measurement, HUT-12 sample.

Because of the crack, the slick water permeability was 830 nD, which is much larger than the original brine permeability (Figure 4.18). Instead of discarding the sample, more slick water was injected to see whether it would plug the crack and reduce the permeability. After 10 hours of slick water injection, the permeability was measured again; the slick water permeability was reduced to 1 nD. This means that the slick water plugged and reduced the permeability of the shale, even when it had a small fracture in it (Figure 4.19). This has important implications for fluid leakoff during fracturing when these sorts of micro-cracks are generated. After this slick water test, another brine test was performed, but the permeability with a PPT test could not be measured due to the continuous generation of cracks, and the flow rate was higher than the measuring limit.

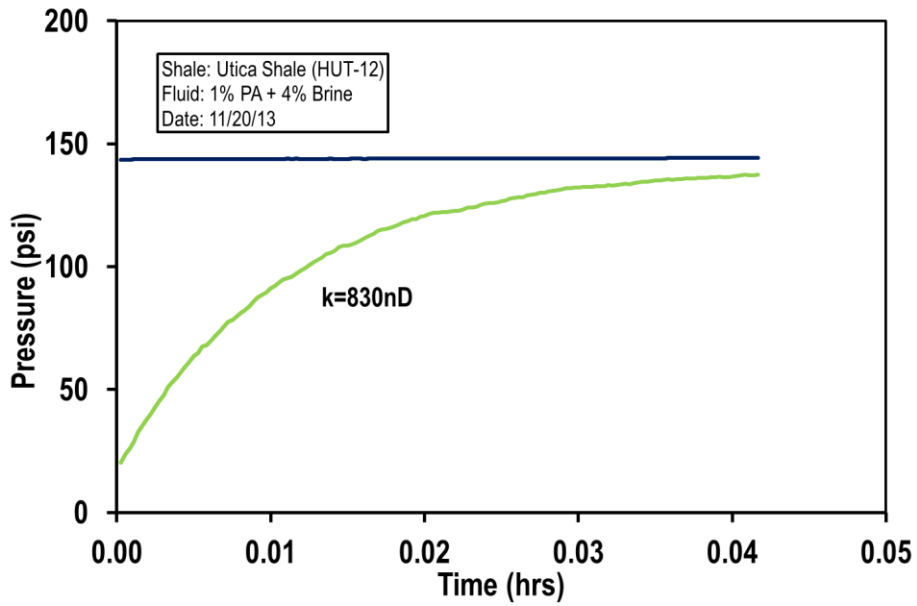


Figure 4.18: Initial slick water permeability measurement, HUT-12 sample.

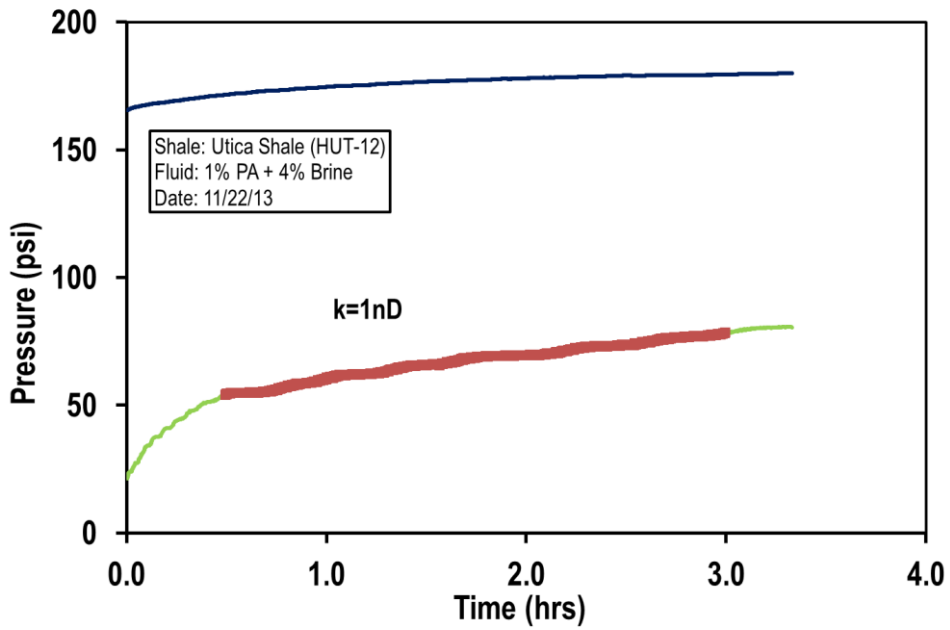


Figure 4.19: Another slick water permeability measurement of the HUT-12 sample after 10 hours of slick water injection.

One more test was performed with a Utica shale sample (HUT-16). This sample showed results that were similar to those of HUT-12. The initial brine permeability was 5nD, but a crack developed again in the sample after the brine test (Figure 4.20).

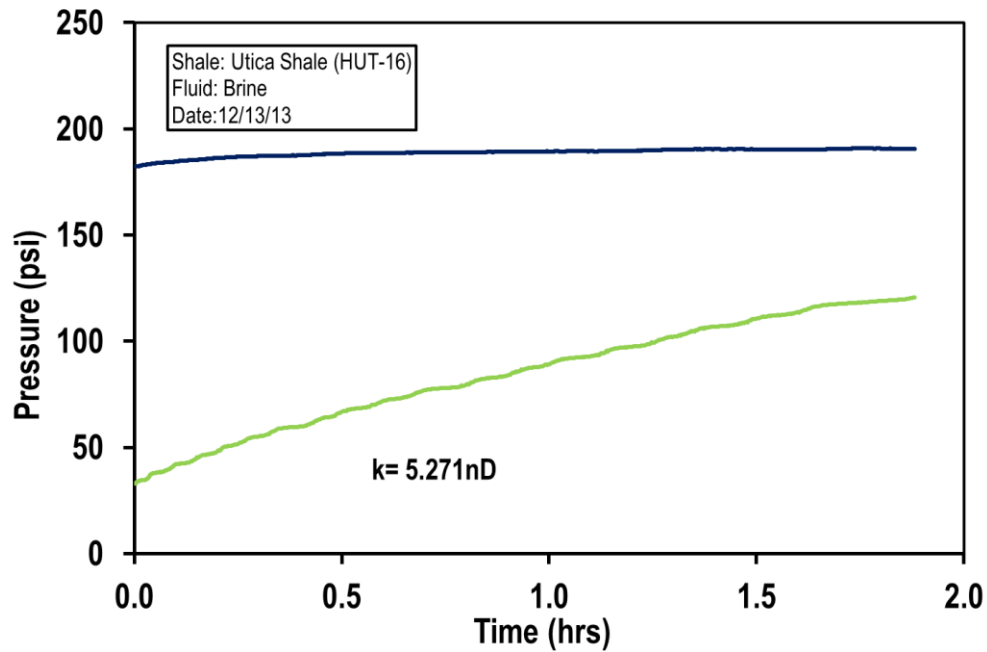


Figure 4.20: Initial brine permeability measurement, HUT-16 sample.

Due to the generated crack, the slick water permeability test concluded after several minutes. The slick water permeability was 64 nD, which is 13 times larger than the initial brine permeability (Figure 4.21). Using the same procedure as was used for the HUT-12 sample test, the slick water was injected for 10 hours, and the final slick water permeability was measured (Figure 4.22). The permeability was reduced again to 0.882, which is 98% smaller than the original slick water permeability. The additional brine permeability test was performed again, but it was impossible to measure the permeability due to very high flow rate.

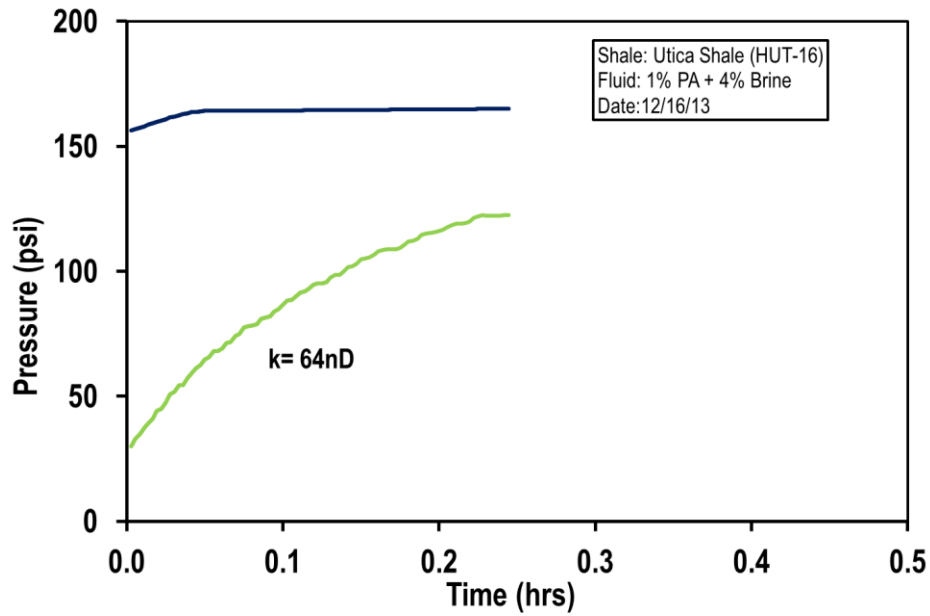


Figure 4.21: Initial slick water permeability measurement, HUT-16 sample.

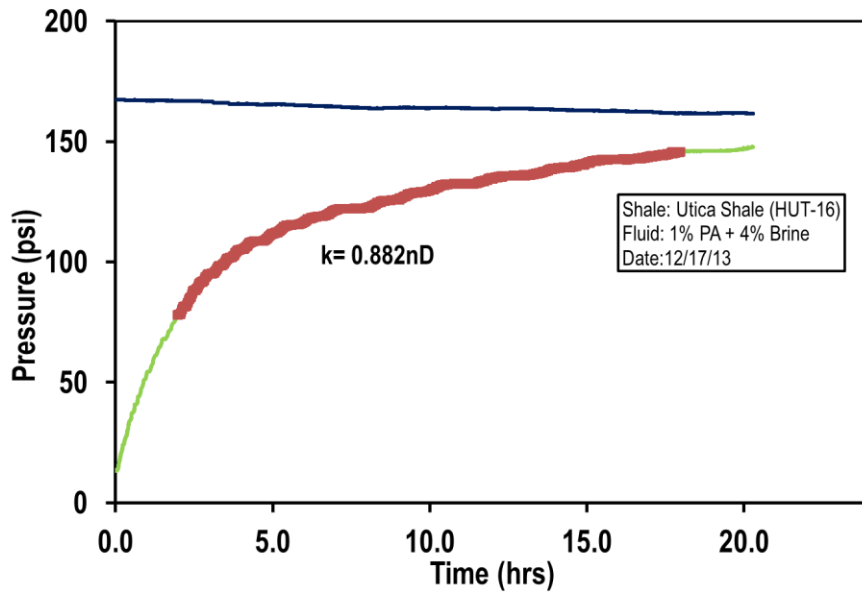


Figure 4.22: Another slick water permeability measurement, HUT-16 sample, after 10 hours of slick water injection.

### 4.3 CONCLUSIONS

The change in Utica shale permeability was investigated after the shale was exposed to slick water. Slick water plugged the shale surface and produced a shale permeability reduction of more than an order of magnitude. The HUT-10 sample results show that the slick water reduces the shale permeability by 97% of the initial brine permeability.

However, the slick water plugging was not stable, so it did not result in permanent permeability reduction when micro-fractures are present. From the HUT-12 and H-16 sample results, even though the slick water permeability was reduced to about 1 nD after 10 hours of injection, the subsequent brine permeability was too high to measure using the PPT set-up. The slick water plugging was not sufficient to block the generated cracks permanently (Table 4.2).

Table 4.2: Summary of Utica shale test results.

Sample	Brine (4% NaCl)	Slick Water (1% PA solution)	Brine (4% NaCl)
Utica shale (HUT-10)	272 nD	6 nD	9 nD (after 12 hr slick water injection)
Utica shale (HUT-12)	5 nD (Crack-generated)	830 nD → 1 nD (after 10 hrs of injection)	Cannot hold bottom pressure due to very high flow rate
Utica shale (HUT-16)	5 nD (Crack-generated)	64 nD → 0.88 nD (after 10 hrs of injection)	Cannot hold bottom pressure due to very high flow rate

The concentration of polyacrylamide (friction reducer) used in this study is 1% which is much higher than that used in the field (usually, 0.1% of friction reducer is used

at the field). The results presented in this study, therefore, represent a worst case scenario with regard to permeability reduction in the shale due to the friction reducer.

In this chapter, the permeability change (among the various petrophysical properties) of shales is solely studied. Other properties, such as proppant embedment, hardness, and wave velocities, were not considered in this study and have been studied elsewhere (Zhang, 2015). Moreover, only one friction reducer was tested in this study, and no other fracturing agents were investigated. Many fracturing fluid additives exist, such as clay stabilizers, cross-linked gels, and polymers and their effects on shale properties should be investigated. Such studies would be interesting in light of this study.

## **Chapter 5: High-Performance Water-Based Mud Using Nanoparticles for Shale Reservoirs**

### **5.1 INTRODUCTION AND PAST WORK**

Drilling through a clay rich shale layer often results in borehole instability problems. It has been estimated that shale formations make up more than 75% of all drilled formations; they account for more than 90% of all expenses associated with wellbore instability. Among the various factors that produce instability, our study will focus on the transfer of water to shale. Shale invaded by water raises a host of problems, including hole-collapse and wellbore weakening. This is because the clay minerals inside the shale interact with water in the drilling fluid. To prevent water from contacting the shale, oil-based muds (OBMs) are traditionally used. OBMs have good wellbore stability and lubricity properties since they do not interact with shales. OBMs, however, are expensive and are subject to environmental constraints, so some countries have established regulations to prevent the use of OBM. Because of this, water-based muds (WBMs) that are suitable for drilling shales are needed.

To use WBMs in shale reservoirs, several issues need to be resolved. For one thing, WBMs can interact with the shale pore fluid more easily than OBMs. This interaction can potentially lead to a loss of pore pressure support. To reduce the pressure loss, internal or external filter cakes should be developed. Shales have extremely low permeability and small pore throat size, so normal drilling fluids fail to form impermeable internal or external mud cakes and thus fail to stop fluid invasion. The industry uses several guidelines when choosing the particle size and distribution of bridging materials that can form effective internal and external mud cakes and minimize formation damage. Suri and Sharma (2004) showed that to form multiple particle bridges, the particle size should be no less than one-third the pore throat size. As shown earlier in

our lab, Al-Bazali et al. (2006) and Oleas et al. (2008), a variety of shales had an average pore throat size ranging from 10 to 30 nanometers. Comparatively, bentonite and barite, two commonly used drilling fluid additives, have much larger particle diameters, in the range of 0.1 to 100 microns. This particle size is too large to penetrate the shale pores and form a filter cake that will significantly impede the flow of water into the shale. To plug most shale pores particle sizes need to be less than about 50nm (0.05 microns).

In a recent study, Sensoy et al. (2009) and Cai et al. (2012) showed that nanoparticles (particle diameters in the nanometer range) can plug several types of shale, preventing water from flowing into the shale formation. They demonstrated that nanoparticles performed well at plugging the pore throats of Atoka and Gulf of Mexico (GOM) shales, significantly reducing the permeability of the shale and minimizing fluid invasion. Despite their positive results, their results are limited since they tested only shale samples which do not contain organic material such as bitumen, oil and gas.

In this chapter, a Texas gas shale, Eagle Ford shale and Barnett shale samples which contain organic materials such as kerogen, bitumen, oil and gas were tested. Our testing fluids were 4 weight percent sea salt brine, base mud, and a water-based mud containing nano-particles (Nano mud). To determine the proper size of nanoparticles to be used in the mud, the pore throat size of Texas gas shale was investigated using the dual beam SEM/FIB machine. The original surface of the shale was too rough, so it was impossible to observe in-situ shale structure and its pore throats. After the surface was milled with an ion beam, the in-situ structure and its pore throat size were investigated, and the pore throat was measured to be in the 20-30nm size range (Figure 5.1). Suri and Sharma (2004) ensured that the particles were small enough to plug the pores, and a particle size less than the pore throat size was chosen. Based on the pore throat size, we selected nanoparticles which are 20 nm in diameter. When the nanoparticles plug these



pore throats, the shale was effectively plugged and acted as if it much less impermeable to brine, minimizing shale swelling and other osmotic phenomena.

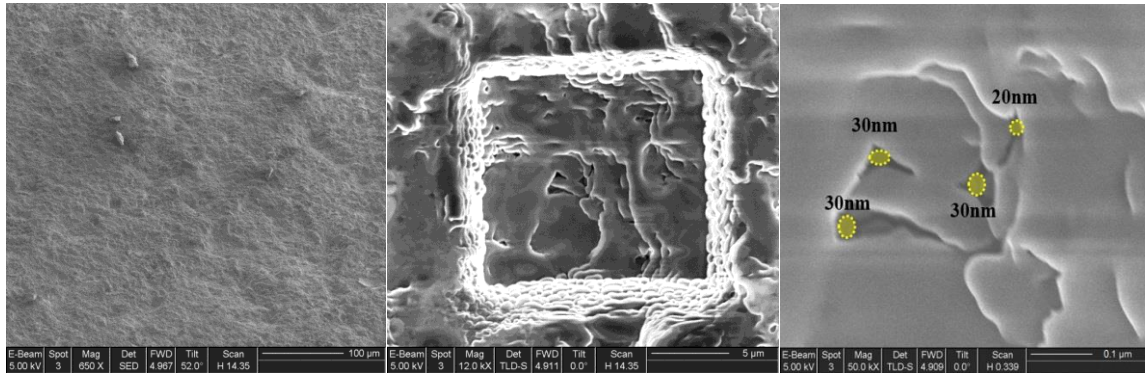


Figure 5.1: SEM image of Texas gas shale: (a) original surface, (b) ion-milled surface with dual beam SEM/FIB, and (c) pore throat size of shale.

## 5.2 EXPERIMENTAL PROCEDURES

The Pressure Penetration Technique (PPT) tests were performed to investigate the effect of physical plugging of shales by nanoparticles. Using this technique, the permeability of shale samples was measured in contact with various kinds of fluids: brine, base mud, and base mud with various concentrations of nanoparticles (Refer to Chapter 4 for details of the experimental technique). The shale permeability with 4 weight % sea salt brine was measured first as a reference permeability, and then base mud and a mud containing nanoparticles were tested to observe the change in permeability. A reduction in permeability means the muds containing nanoparticles were able to plug the shale pore throats, and water invasion into the shale was reduced. Water sensitive shales can be made more stable when exposed to such drilling fluids because of the reduction in water infiltration into the shale.

### 5.2.1 The Properties of Shales: Mineralogy and Native Water Activity

Three organic rich shales were chosen for our experiments. X-ray diffraction analysis (XRD) was conducted to investigate the mineralogy of the Texas gas shale, Eagle Ford shale and the Barnett shale (Table 5.1).

Table 5.1: XRD mineralogy test result of shales.

Mineral	Quartz	Calcite	Dolomite	Albite	Total Clay
Texas Gas Shale	17	50.7	2.9	7.9	19
Eagle Ford Shale	11	49.2	2.7	10.4	24.2
Barnett Shale	38.5	2.6	3.3	17.2	35

The original water activities of all shales were measured. Texas gas shale has a water activity of 0.92 (refer to Chapter 3), the Eagle Ford shale has a water activity of 0.72, and the Barnett shale has a water activity of 0.90 (Figure 5.2). With the native shale water activity established, the preserved shale samples were kept in a controlled humidity desiccator that contained a specific saturated salt solution. By storing the samples in such desiccators, the shale sample can be maintained in a preserved status without losing or gaining water from the surrounding air. The importance of shale preservation was discussed in detail in Chapter 3.

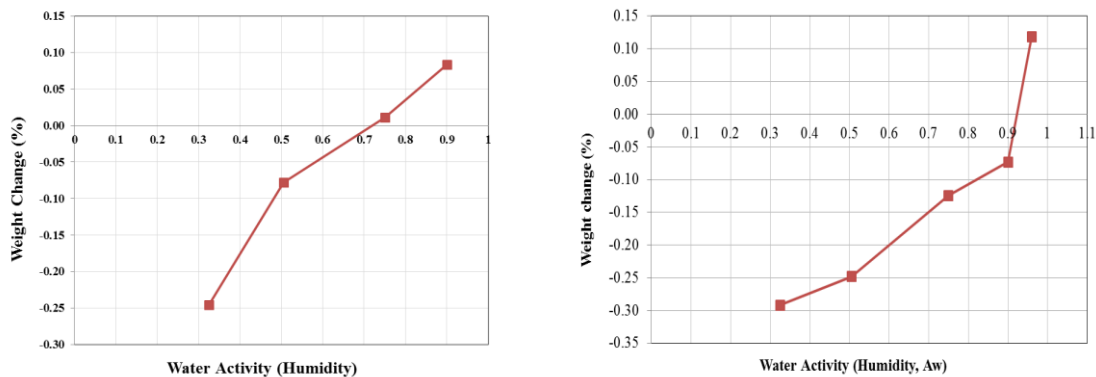


Figure 5.2: The water activity measurement of a) Eagle Ford shale and b) Barnett shale.

## 5.2.2 The Properties of Water Based Mud and Nano Mud

Our water-based muds were obtained from M-I Swaco for our joint work on nano-particle based drilling fluid development. I spent three months as a summer intern at M-I Swaco in 2012 and established the test procedures, such as shale sample preparation and also the permeability test apparatus for them. The base mud composition, the nanoparticle concentration and rheology data of muds are listed in Table 5.2 and 5.3. (Ji et al., 2012). The base mud used here is not a conventional base mud but the one which M-I Swaco specially designed for shale reservoirs to improve the drilling performance. However, it does not contain any nanoparticles, so it is a good starting point to test the effect of nanoparticles.

Table 5.2: The Composition of Base Mud.

<b>Base Mud Ingredient</b>	<b>CAS No.</b>	<b>Wt. %</b>
Water	7732-18-5	70-95
Sodium Chloride	7647-14-5	0-20
Barite	7727-43-7	0-25
Hydrocarbon		0-5
Polyoxypropylene diamine	9046-10-0	0-5
Silica, crystalline, quartz	14808-60-7	0.1-1

Table 5.3: Mud properties for the base mud and the nano-particle muds.

Contents	Unit	Base Mud	10ppb Nano Mud	30ppb Nano Mud
Nanoparticle solution	%	0	3%	10%
Density	lb/gal	11.99	11.86	11.95
10-sec gel strength	lb/100ft <sup>2</sup>	7	6	5
10-min gel strength	lb/100ft <sup>2</sup>	10	8	7
Plastic viscosity	cP	19	28	28
Yield point	lb/100ft <sup>2</sup>	36	18	12
pH		9.65	8.7	9

### 5.2.3 Pressure Penetration Technique (PPT) Test and Darcy Flow Test

The PPT set-up was specially designed for measuring the apparent permeability of low permeable cores, and it is a convenient tool to compare various kinds of fluids such as brine, surfactant solutions, base mud and mud with nanoparticle solutions. Figure 5.3 and 5.4 show the PPT test set-up. This set-up is designed for extremely low permeability samples with permeabilities in the range of 0.001nD to 20,000nD. If the permeability of shale is too high over the range of PPT test, original PPT set-up needs to be modified. In many cases, samples have natural fractures, or cracks can develop in the sample during the PPT test. In such instances, the flow rate through the shale sample is very high, and it is impossible to get enough data points to measure the apparent permeability. When this happens, we modify the PPT set-up, and use a different approach to measure the fluid permeability. Figure 5.5 shows the modification of the PPT set-up for such cases to measure highly permeable samples. This set-up is called as the steady-

state Darcy flow set-up. The modification of the PPT set-up is easily accomplished by disconnecting Valve 2 (V2) and connecting a graduated cylinder to the outflow. Then the outflow flow rate is measured and Darcy's law is used to calculate the permeability.

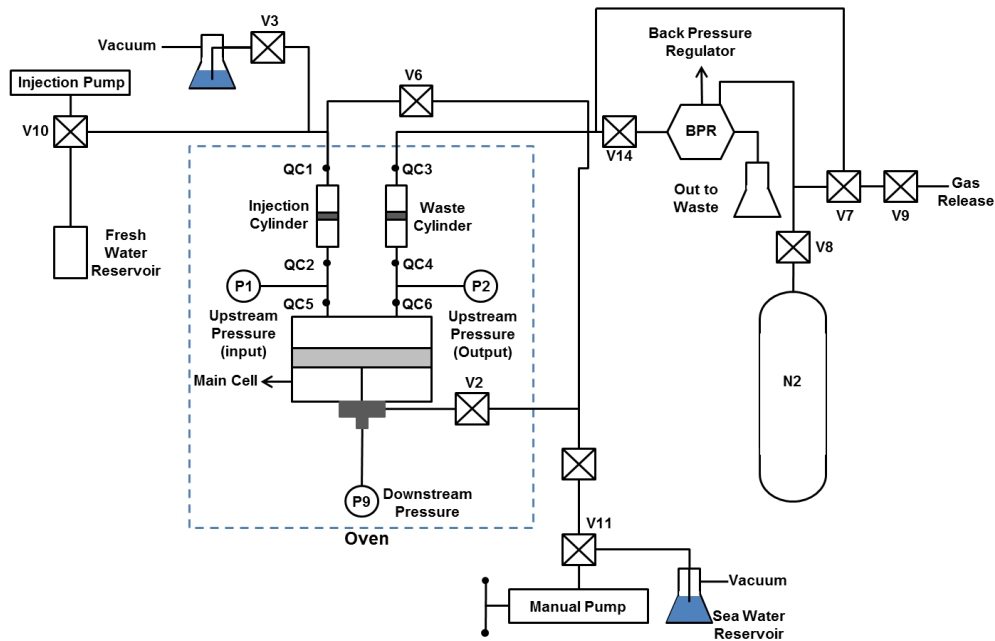


Figure 5.3: Pressure Penetration Technique (PPT) test set-up.

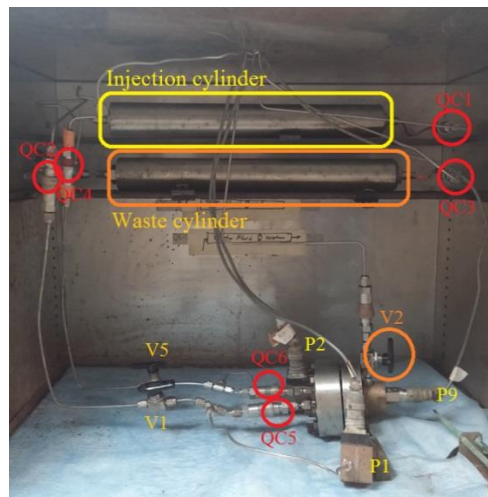


Figure 5.4: Picture of the PPT set-up inside an oven.

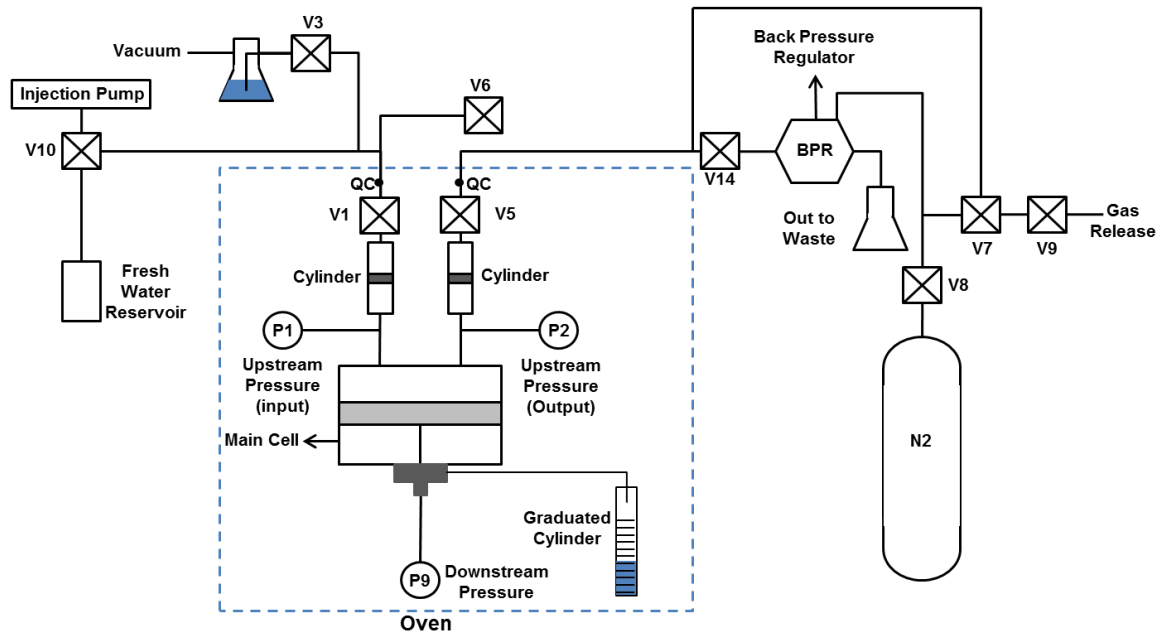


Figure 5.5: Modification of the PPT set-up for Darcy flow permeability test.

### 5.2.3 Permeability Measurement: Detailed Procedures

The first step in the permeability measurement is to clean the top injection cylinder. The quick connector, QC1 (Quick Connector 1) and QC2, are released then by holding the cylinder using a vice, a QC release fitting is applied, so the test fluid can exit from the cylinder. Then unscrew the top plug and pour left over fluid in a proper waste container. Using a vice, hold the other side of top cylinder then unscrew the bottom plug. Then the waste fluid is disposed into a proper container. Using a wooden push pole, the floating piston is removed from the cylinder. Using soap and a brush, all threads and the piston needs to be washed carefully.

The reference permeability test is always performed using 4 weight % sea salt brine solution. The volume of the cylinder is around 400ml, so a 400ml sea water

solution is prepared to fill the cylinder. To do this, 16g of sea salt is mixed with 384g of D-I (deionized) water. Then, the floating piston is put into the end of the injection site of the cylinder. Next, screw in the right cap, and hold the cylinder using a vice. Then fill the cylinder with sea water, and screw in the left cap. At this time, check to be sure that no air remains in the cylinder by watching sea water exit the QC release fitting. Remove the release fitting and install the injection cylinder connecting to QC1 and QC2, and put on the top shelf.

Then, prepare the waste cylinder. Remove the bottom waste cylinder which contains waste fluid by releasing QC3 and QC4. Dispose of fluids in a proper container and clean all threads and a piston as done before. Replace the piston and fill with tap water to the maximum level as done above. Install the bottom cylinder connecting to QC 3 and QC 4.

Then install a new shale sample into the main test cell. Remove the main test cell disconnecting QC 5 and QC 6. Then unscrew 11 bolts and nuts from the cell, and open the cell and remove two screen wires fit a plates, the used sample and the two O-rings, and then wash the cell parts and let them dry. Then fill the hold-up volume with sea water, and close V2. Install a new shale sample, screen wires and O-rings. We then add washers and bolts and hand tighten the nuts. A gap-gauge is used to ensure parallel top and bottom cell parts. Using a screwdriver-type torque wrench, torque all bolts to 12 ft-lb, then 24, then 36 ft-lb. Using gap-gauge, check again, adjust nuts if necessary until parallel. Then install the main cell at the original position connecting to QC 5 and QC 6, and then open V2.

Then, fill the injection syringe pump. Open V10, and push the toggle switch on the syringe pump from deliver to refill. Then push the toggle switch from stop to run. Set the max flow rate to 400 mL and set the rate to 100%. Watch the pump suck fresh water out of the fresh water reservoir. When the syringe pump fills to 500 mL, press the toggle switch to stop. Then raise the toggle switch to deliver and close V10.

Next step is to remove air from lines using vacuum evacuation. First, remove air from injection cylinder side. Open V3 and V10, and pull a vacuum on the fresh water reservoir using a vacuum bottle. Then release the vacuum hose, then close V3. Next, remove air from the bottom waste cell using a sea water manual pump. Then open V11 and V2, and pull a vacuum using a vacuum bottle, and close V2. Then release the vacuum on the sea water bottle. Close V11, and this allows the manual pump to pump the sea water. Clean out the beaker and attach to BPR. This allows us to keep track of the volume of water leaving the cylinder.

Now, it is ready to run a new test. Set the N<sub>2</sub> bottle pressure as an injection pressure, and set the syringe pump at 400 mL/hour and 100% rate. When the top pressure reaches the setting pressure, the pump rate is slowed to 150 mL/hour and 50% for the top pressure to be constant. Start recording the pressure data versus time using a LabView program. Using the hand pump, set the downstream pressure and close V2. Monitor the test until the bottom pressure approaches the top pressure, or until a satisfactory number of data points are taken. The base mud and nano mud tests can be performed using the same procedure as mentioned above. Just need to simply change from sea water to the mud being tested, and run the mud permeability test.



The permeability test usually takes more than 10 hours, and the mud characteristics inside the test cell may change over this time. If the shear rate is not fast enough, the mud can gel. To prevent this, the shear stress on the mud should always be larger than gel strength of the mud. The shear stress and the gel stress are easily measured in any test environment.

The minimum pump injection rate is 30 ml/hr, and the injection hole radius is 1/16 inches. The volumetric flow rate is  $8.333 \times 10^{-9} \text{ m}^3/\text{hr}$ , and the cross-sectional area of the hole is  $7.913 \times 10^{-6} \text{ m}^2$ . The flow velocity ( $v$ ) is then, 0.00105m/sec. The shear rate of mud ( $\dot{\gamma}$ ) is calculated below to be  $2.653 \text{ sec}^{-1}$ .

$$\dot{\gamma} = \frac{8v}{d} = \frac{8v}{2r}$$

The viscosity of nano-mud is 28 cp, and the viscosity of base-mud is 19 cp. The shear stress (shear rate times mud viscosity) of the nano-mud is  $15.52 \text{ lb}/100\text{ft}^2$ , and the shear stress of the base-mud is  $10.53 \text{ lb}/100\text{ft}^2$ . The gel strength of the nano-mud is  $6 \text{ lb}/100\text{ft}^2$  and the gel strength of the base-mud is  $7 \text{ lb}/100\text{ft}^2$  which are both smaller than the shear stress imposed on the mud as it is being circulated on the upstream side of the PPT cell, when the injection rate is faster than 30 ml/hr.

## **5.3 EXPERIMENTAL RESULTS**

### **5.3.1 Texas Gas Shale Results**

Five Texas gas shale samples were tested with brine, base mud, and nano-muds. The test results and conditions are listed in Table 5.3. These 5 samples were tested at a

differential pressure of 250 psi across the shale in the PPT tests; 300 psi upstream and 50 psi downstream.

Table 5.3: Texas Gas Shale (TGS) permeability results.

Sample	Testing Fluid	Permeability (nD)	Test time
TGS 10	4% NaCl Brine	22,624	2 minutes
	Base Mud	22	15 hours
	4% NaCl Brine	28	18 hours
TGS 7	4% NaCl Brine	15,097	3 minutes
	30ppb Nano-Mud	0.28	35 hours
TGS 9	4% NaCl Brine	19,810	2 minutes
	10ppb Nano-Mud	0.42	23 hours
	4% NaCl Brine	5.55	25 hours
TGS 24	4% NaCl Brine	109,370*	20 minutes
	10ppb Nano-Mud	0.0014	18 hours
	4% NaCl Brine	0.082/18.31	7 hours
TGSB 2	4% NaCl Brine	76,625*	20 minutes
	10% Nanoparticle solution	208	12 minutes

\* These results were measured by the Darcy flow permeability test set-up.

The first sample, TGS 10, was tested with brine and base mud with no nanoparticles. Figure 5.6 shows the 4 weight % sea salt brine permeability test results. The brine permeability was used as reference permeability, and it was 22,624nD which is much higher than the permeability of conventional shale. This indicates that the sample had micro-fractures in it. Even though, all shale samples which are used in this study are preserved, during the drilling or coring process, micro cracks can easily be generated. Moreover, many shales also have natural fractures, that is one possible reason why the reference permeability to brine is so high compared to the permeability of conventional shale samples.

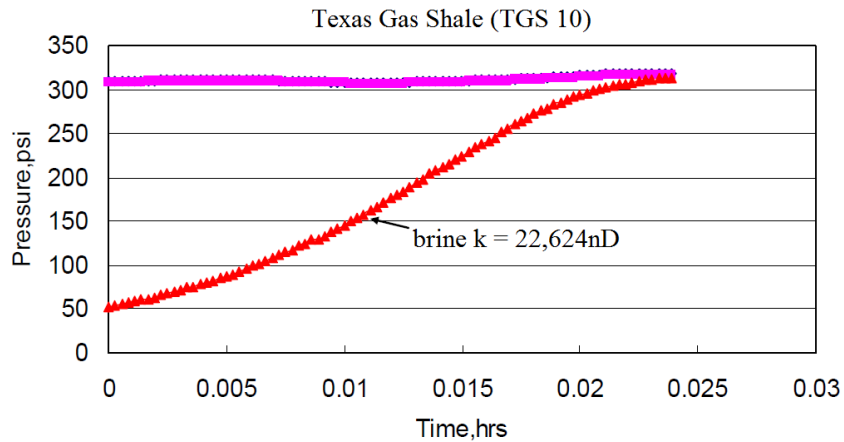


Figure 5.6: Brine permeability results of Texas Gas Shale (TGS 10).

After the brine test, the same sample was then flushed with the base mud to see how much plugging would happen when we introduced the base mud. The mud permeability was 22nD which is a 99.9% permeability reduction when compared with the reference permeability (Figure 5.7). To see the durability of this permeability reduction, another brine permeability test was run on the same sample. The permeability remained unchanged at 28nD, so the durability of the mud cake was good and the microfractures remain plugged even when exposed to brine (Figure 5.7).

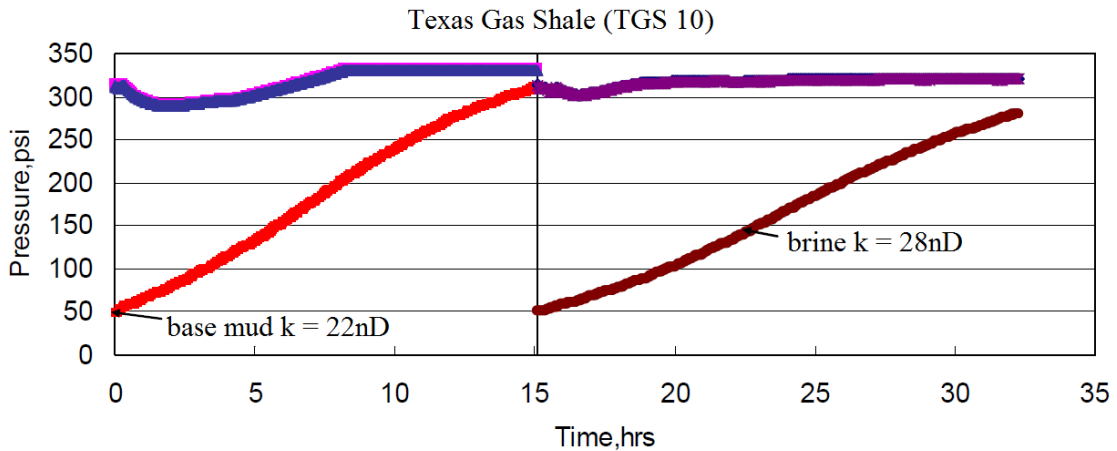


Figure 5.7: Base mud permeability results and following brine permeability results of Texas Gas Shale (TGS 10).

The second Texas gas shale sample, TGS 7, was tested with brine and 30 pounds per barrel (ppb) nano-mud. The reference permeability with brine was measured to be 15,097nD (Figure 5.8).

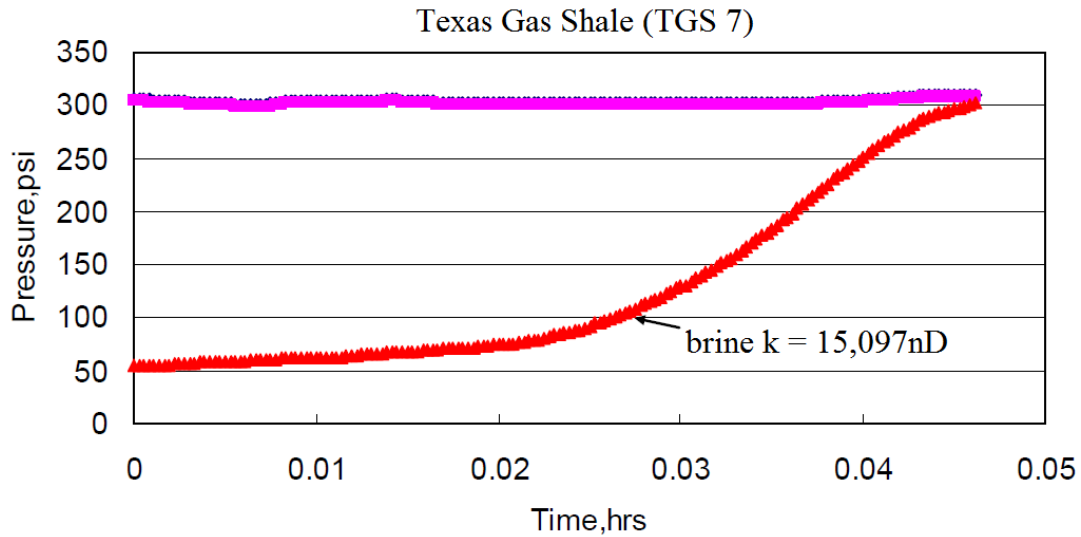


Figure 5.8: Brine permeability results of Texas Gas Shale (TGS 7).

After the brine injection, a 30ppb nano-mud was introduced. The shale permeability with the nano-mud was 0.28nD. This means that the nano-mud almost completely shut-off the pressure transmission through the sample (Figure 5.9). This indicates that shales with micro-fractures can be successfully plugged with muds containing nano-particles.

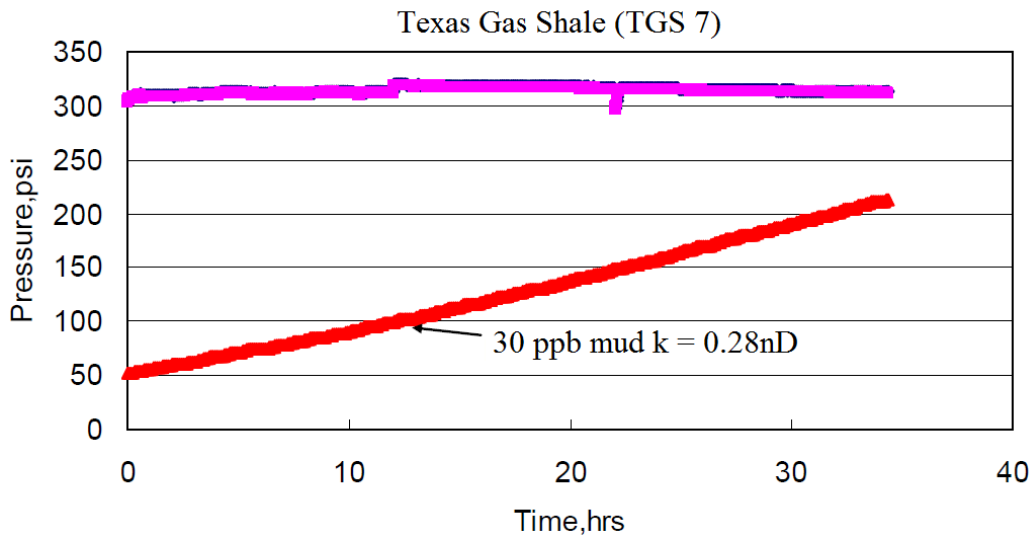


Figure 5.9: 30 ppb nano mud permeability results of Texas Gas Shale (TGS 7).

The third sample, TGS 9, was tested with brine and 10ppb nano-mud. In this test, the minimum concentration of nanoparticles which can reduce the permeability was observed. The permeability with brine was measured to be 15,097nD (Figure 5.10).

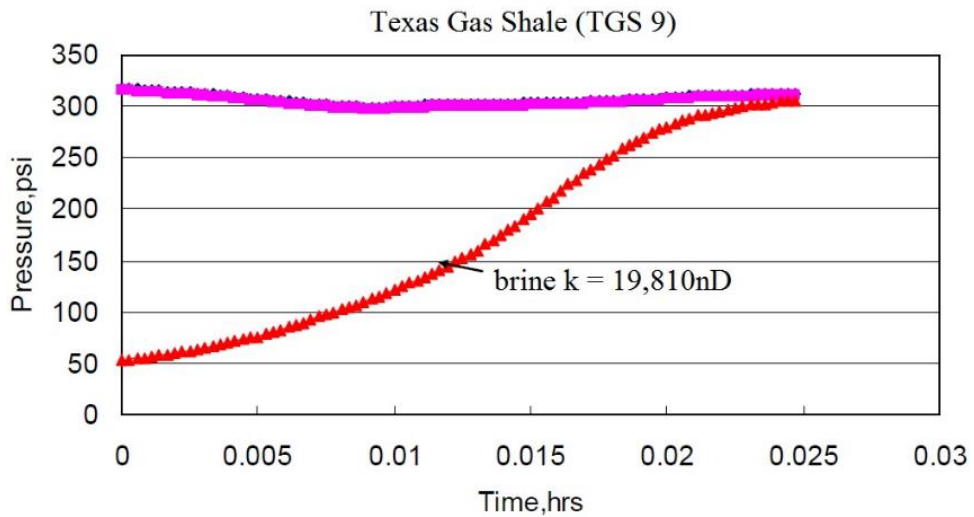


Figure 5.10: Brine permeability results of Texas Gas Shale (TGS 9).

Using the 10 ppb nano mud, the permeability was reduced to 0.28nD. It means that 10 ppb of nano-particles in the mud was enough to prevent water invasion into the shale. After the nano-mud test, one more brine permeability test on the same sample was run to see the durability of the plugging, and the permeability was increased to 5.55nD, but it was still much lower than the initial permeability (Figure 5.11).

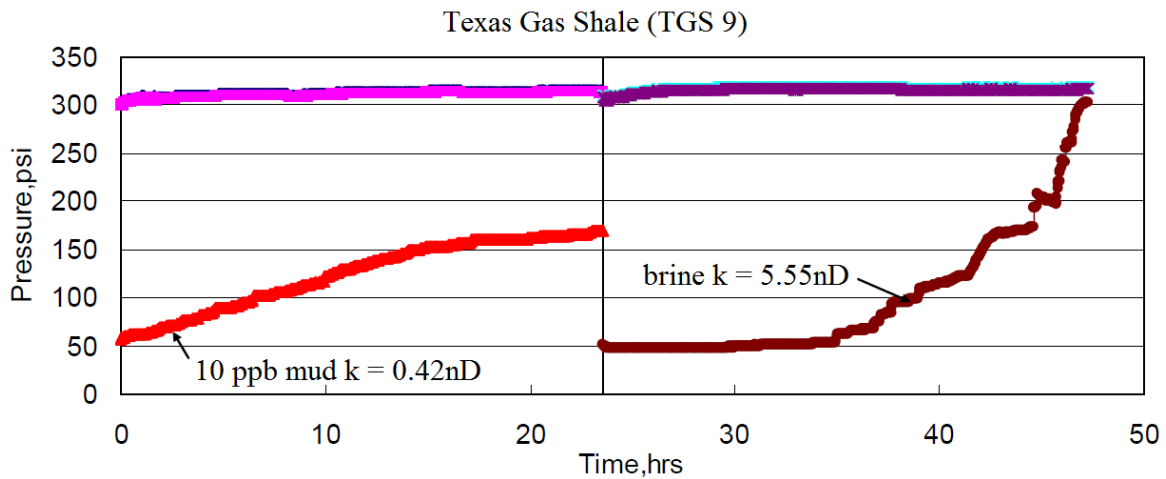


Figure 5.11: 10 ppb nano mud permeability results followed by brine injection, Texas Gas Shale (TGS 9).

The fourth sample, TGS 24, had a wider fracture (indicated by very high flow rate), so the PPT set-up was not suitable to measure its permeability. The Darcy flow test which is a modification of PPT was used to measure the permeability of this fractured sample. Figure 5.12 shows the collected fluid volume versus time for this test. Using the flow rate from this result, the apparent permeability of this sample was 109,370nD (0.1 mD).

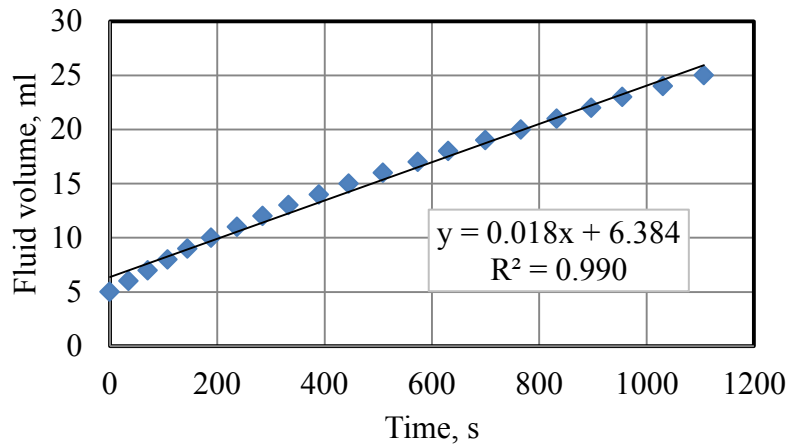


Figure 5.12: Brine permeability measurement of Texas Gas Shale (TGS 24) using Darcy flow test.

Then 10 ppb nano mud was introduced to test whether the nano mud could plug such large cracks and also pores of the shale sample. The nano mud permeability was 0.0014nD which was much lower than the original crack permeability. This shows that the nano mud effectively plugged the fracture and also the pore throats of the shale. It reduced the pressure transient and fluid loss to an almost immeasurably small value (Figure 5.13).

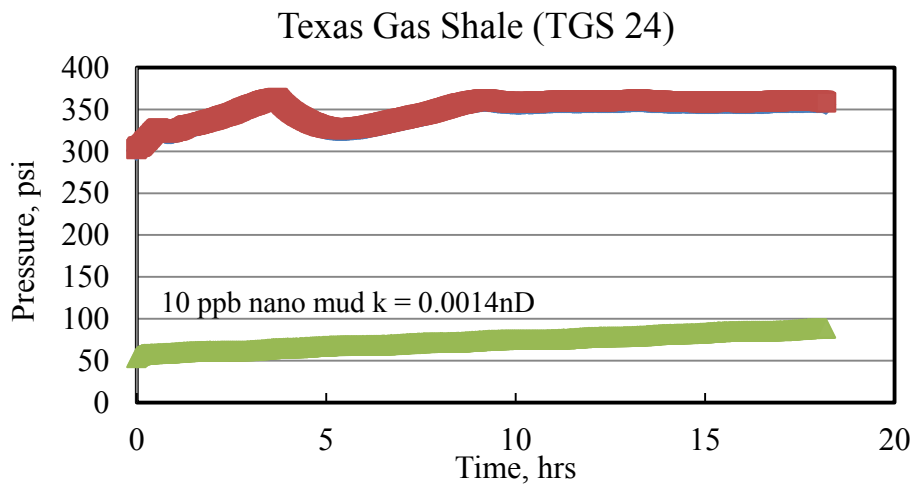


Figure 5.13: 10 ppb nano mud permeability results of Texas Gas Shale (TGS 24).

After the nano-mud test, the following brine permeability test was performed to see the durability of nano-mud. The initial brine permeability was 0.082nD and later it increased to 18.31nD due to the mud clean-up. This sample originally had a large crack which leads to a 0.1 mD permeability, so the nano-mud results in a huge permeability reduction, but the durability of plugging was not as stable as the cases of other samples. However, it was still much lower than the initial permeability (Figure 5.14).

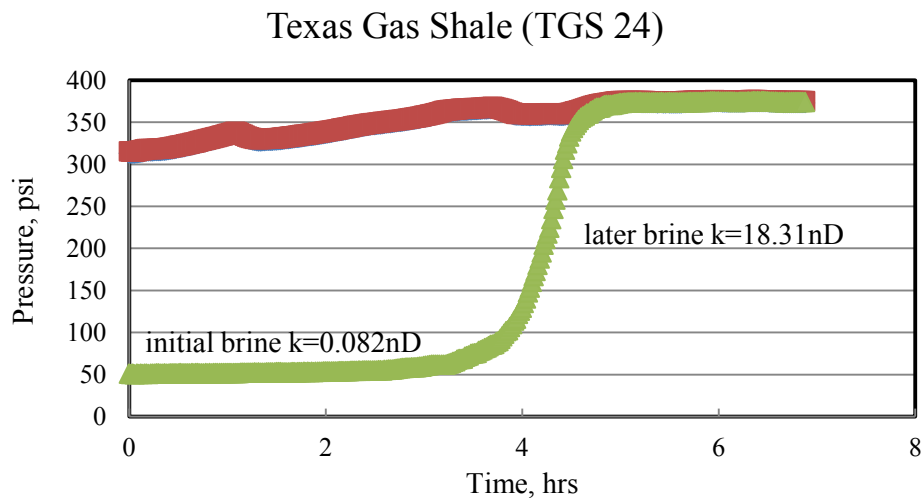


Figure 5.14: Brine permeability results of Texas Gas Shale (TGS 24).

The fifth sample, TGSB 2, also had a fracture, so we used the Darcy flow test to measure its permeability with brine. The brine permeability was 76,625nD based on the measured of flow rate (Figure 5.15).



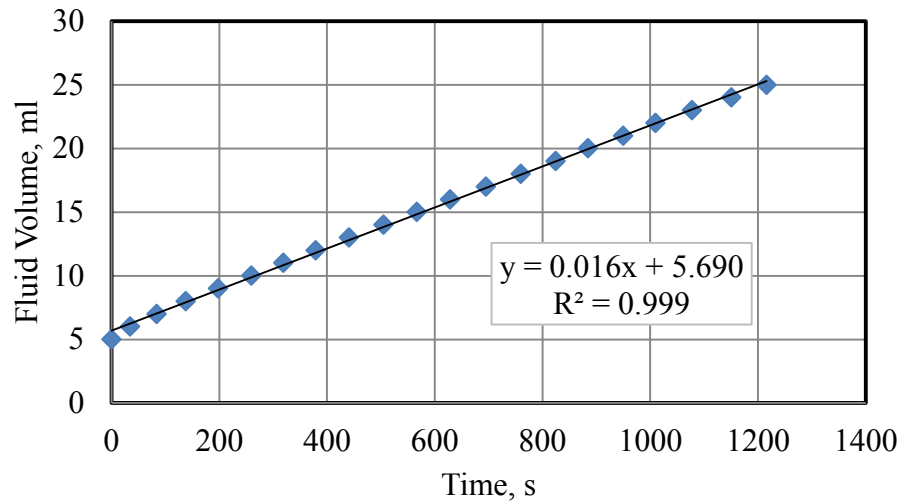


Figure 5.15: Brine permeability measurement of Texas Gas Shale (TGSB 2) using a Darcy flow test.

Then, a 10% nanoparticle solution without base mud was introduced to see whether a nanoparticle solution itself can plug the crack and matrix pore throats. Figure 5.16 shows that the nanoparticle suspension permeability was 208nD which was much lower than the original permeability. The nanoparticle suspension reduced the fluid permeability of the shale sample by plugging the crack and the shale's small pore throats. However, the permeability reduction was much smaller than that obtained with the base-mud or nano-mud because large crack and pore throat did not blocked by larger particles of mud contents. The nano mud appears to offer much better plugging for micro cracks as well as the pores in the shale matrix.

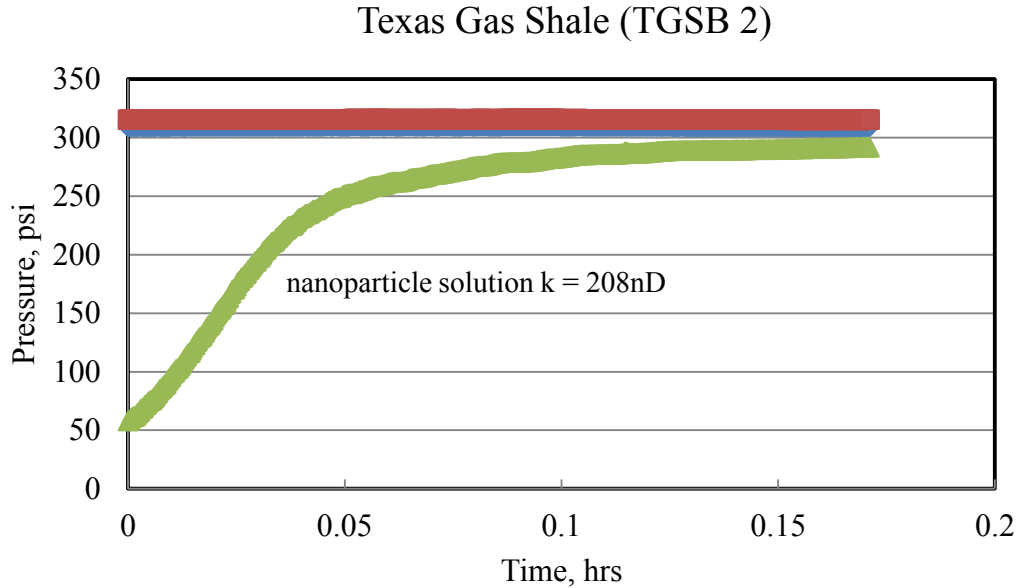


Figure 5.16: 10 percent nanoparticle solution permeability results of Texas Gas Shale (TGSB 2).

### 5.3.2 Eagle Ford Shale Results

Three Eagle Ford shale samples from South Texas were also studied. Brine permeability, base-mud permeability, and 10 ppb nano-mud permeability were measured. The test results and conditions are listed in Table 5.4. These samples had micro-cracks, so three of them were tested using the Darcy flow test to get the brine permeability.

Table 5.4: Eagle Ford shale permeability results.

Sample	Testing Fluid	Permeability (nD)	Test condition	Test time
WGS 17	4% NaCl Brine	61,127*	Upstream pressure: 200psi Downstream pressure: 0psi Pressure differential: 200psi	17 minutes
	10 ppb Nano mud	0.021	Upstream pressure: 300psi Downstream pressure: 50psi Pressure differential: 250psi	25 hours
WGS 32	4% NaCl Brine	290,964*	Upstream pressure: 100psi Downstream pressure: 0psi Pressure differential: 100psi	10 minutes
	Base mud	3.38	Upstream pressure: 300psi Downstream pressure: 50psi Pressure differential: 250psi	17 hours
	10 ppb Nano mud	0.12	Upstream pressure: 300psi Downstream pressure: 50psi Pressure differential: 250psi	28 hours
WGSB 6	4% NaCl Brine	183	Upstream pressure: 180psi Downstream pressure: 20psi Pressure differential: 160psi	3 minutes
	4% NaCl Brine	5,402,886*	Upstream pressure: 100psi Downstream pressure: 0psi Pressure differential: 100psi	4 minutes
	10 ppb Nano mud	0.138	Upstream pressure: 200psi Downstream pressure: 20psi Pressure differential: 180psi	6 hours
	4% NaCl Brine	242	Upstream pressure: 200psi Downstream pressure: 20psi Pressure differential: 180psi	3 minutes

\*These values were measured by the Darcy flow test instead of the PPT test.

The first sample, WGS 17, was tested with brine and 10ppb nano-mud. The brine permeability was measured using the Darcy flow test. Figure 5.17 shows the collected outflow volume versus time from the Darcy flow test. The brine permeability was 61,127nD.

After the reference permeability test, 10 ppb nano mud was injected to determine the permeability reduction due to introducing the nano mud. Figure 5.18 shows the PPT results of WGS 17 when the nano mud was injected. The nano mud permeability was

0.021nD which was much lower than the reference permeability, showing that the nano mud effectively plugged the pore throat and also the cracks.

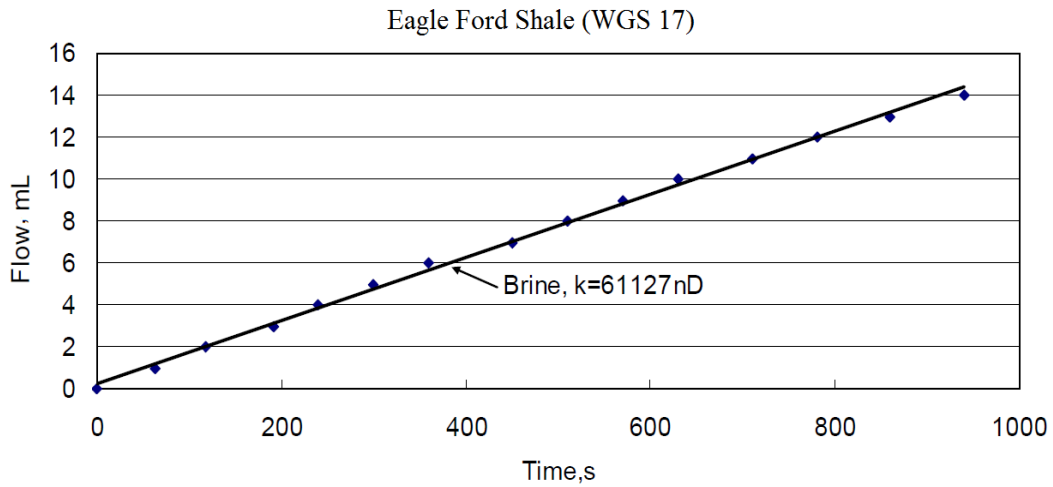


Figure 5.17: Brine permeability measurement of Eagle Ford Shale (WGS 17) using Darcy flow test.  $\Delta p = 200$ psi

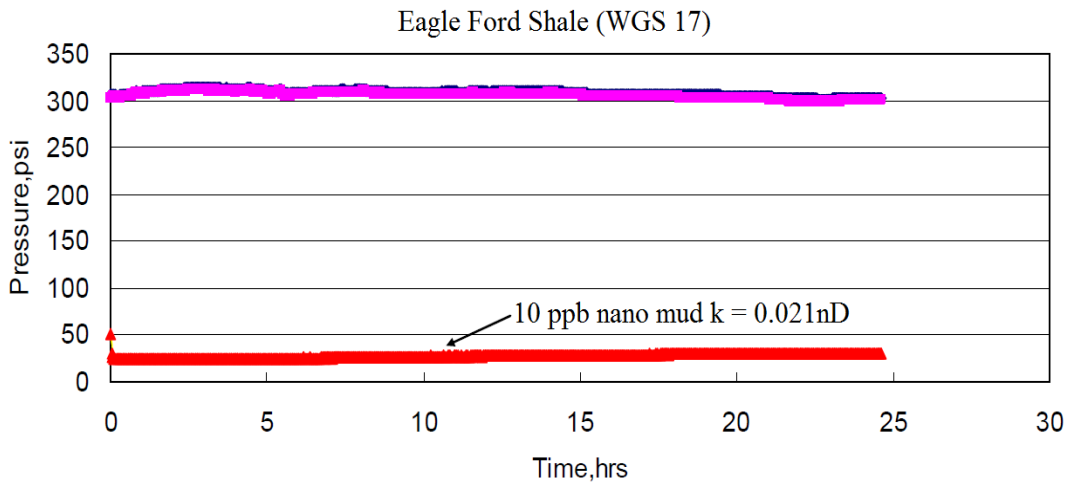


Figure 5.18: 10 ppb nano mud permeability results of Eagle Ford Shale (WGS 17).

The second sample, WGS 32, was tested with brine, base-mud and 10ppb nano-mud. In this test, the effect of nano particle addition to the base mud on the permeability reduction was investigated. The steady-state brine permeability was measured to be 290,964nD (Figure 5.19).

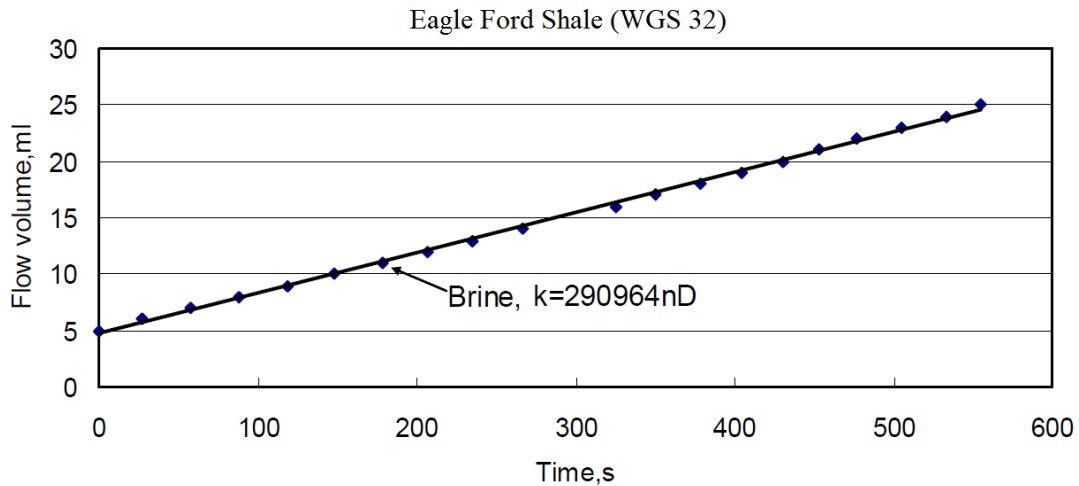


Figure 5.19: Brine permeability measurement of Eagle Ford Shale (WGS 32) using a Darcy flow test.

Using the base mud, the permeability was reduced to 3.38nD which was much lower than the reference permeability. After the base mud test, 10 ppb nano-mud was injected, and the permeability was reduced to 0.12nD (Figure 5.20).

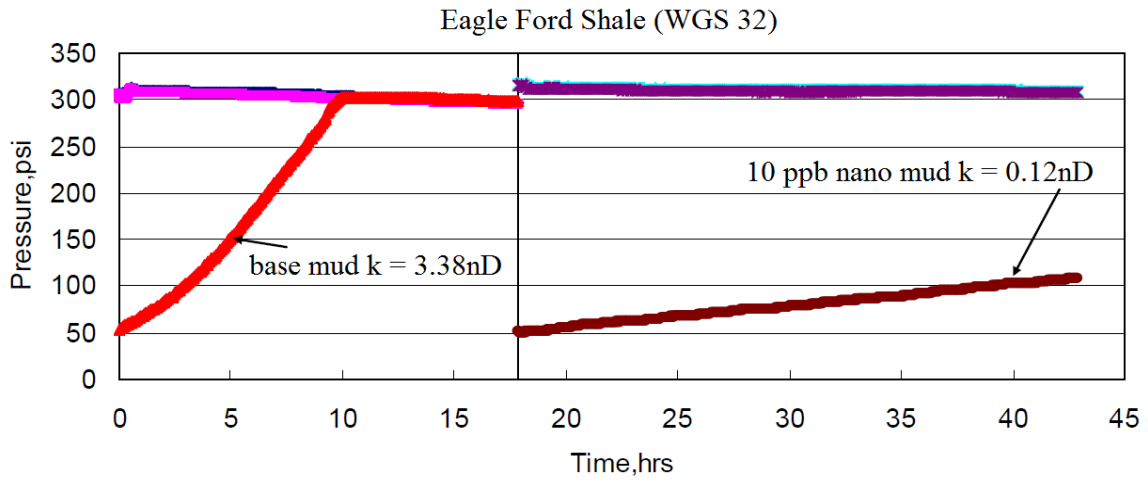


Figure 5.20: Base mud permeability and 10 ppb nano mud permeability results of Eagle Ford Shale (WGS 17).

The third sample, WGSB 6, was tested with brine and a 10ppb nano-mud. The reference brine permeability was measured using the PPT test. The permeability with brine was 183nD. However, after 2 minutes, a crack had developed in the sample, and the flow rate was increasing very fast (Figure 5.21).

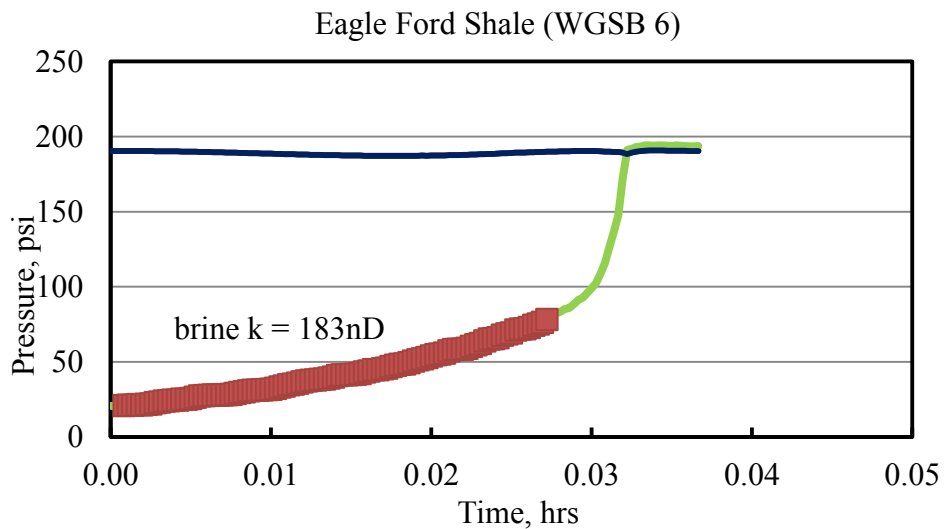


Figure 5.21: Brine permeability results of Eagle Ford Shale (WGSB 6).

Due to the crack generation, the reference brine permeability was re-measured using the Darcy flow test. The reference pseudo brine permeability was increased to 5,402,886 nD (Figure 5.22).

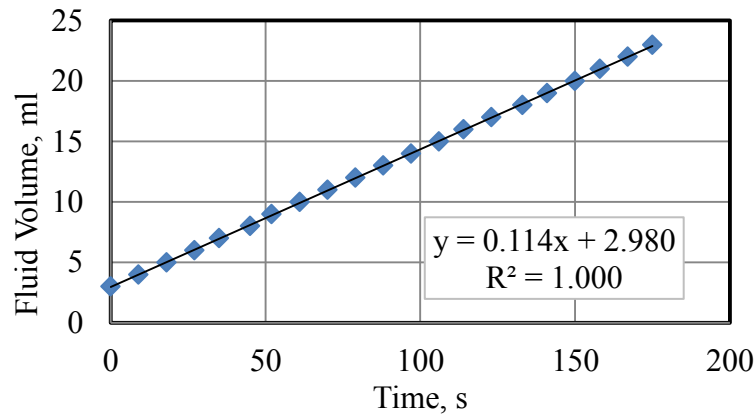


Figure 5.22: Brine permeability results of Eagle Ford Shale (WGSB 6) using the Darcy flow test.

After the brine Darcy test, a 10 ppb nano mud was introduced. The nano mud permeability was 0.138 which was less than 1nD, as we expected, based on the previous results (Figure 5.23).

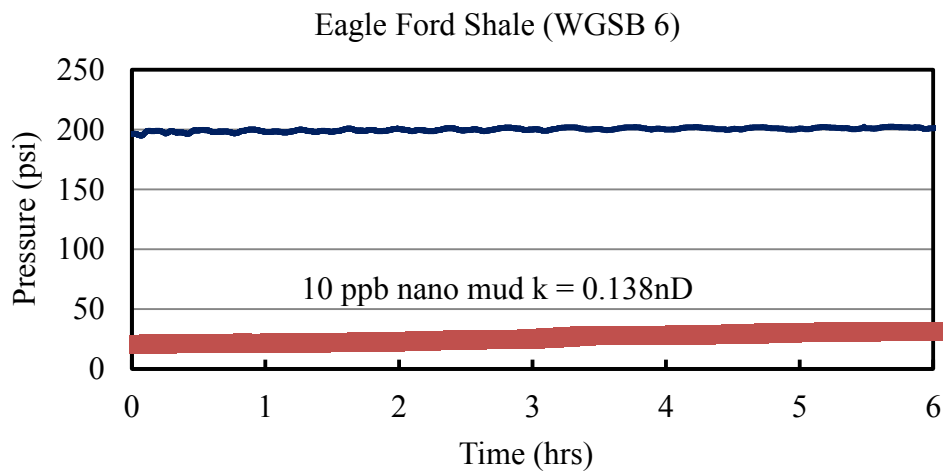


Figure 5.23: 10 ppb nano-mud permeability results of Eagle Ford Shale (WGSB 6).

After the nano mud test, the brine permeability was measured to determine the durability of the 10 ppb nano-mud cake. The brine permeability was 242nD which is much lower than the reference permeability but much higher than the 10 ppb nano-mud permeability. In addition, at the end of the test, the crack re-opened and the flow rate was increasing very fast. At this time, the generated micro crack was too big to be plugged with the nano-mud, and it showed a permeability of 5mD. In this case, the nano-mud filter cake was not strong enough to block the crack permanently. With subsequent brine injection, the cake was removed and the crack was opened again (Figure 5.24).

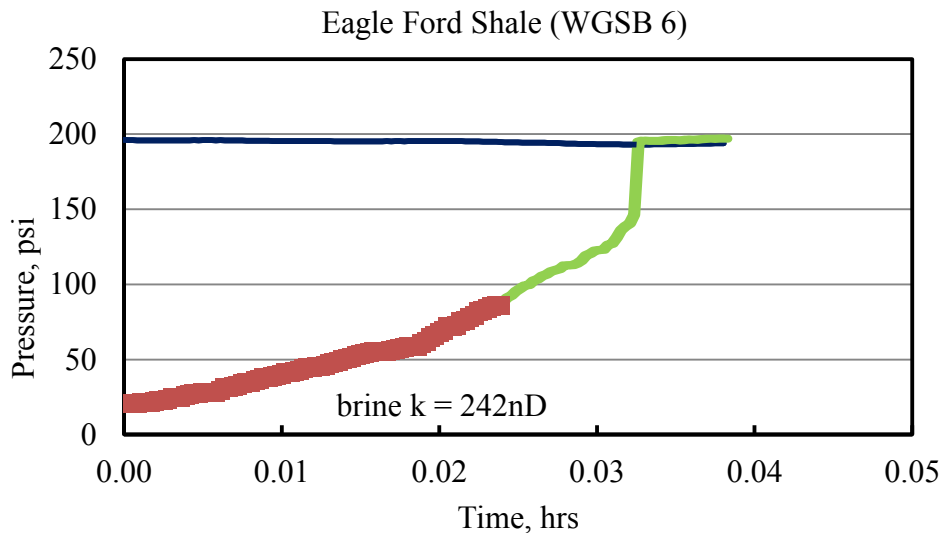


Figure 5.24: Brine permeability results of Eagle Ford Shale (WGSB 6).

### 5.3.3 Barnett Shale Results

Samples of the Barnett shale was also tested. In this case, a surfactant, StimOII® FBA M from CESI Chemical (a Flotek Industries, Inc. company) which may reduce the pressure drop through shale, was also tested before the base mud and the nano mud tests. The surfactant properties are list in Table 5.5.



Table 5.5: The properties of surfactant, StimOII® FBA M.

Name	Substance (Weight %)	pH	Density
StimOII® FBA M	Isopropyl alcohol (10-30%), Citrus Terpenes (10-30%), Proprietary (10-20%)	6.8-8.3	7.95-7.98

The permeability to brine, surfactant solution, base mud, 10 ppb nano mud, and 10% nanoparticle solution permeability were measured. The test results and conditions are listed in Table 5.6.

Table 5.6: Barnett shale permeability results.

Sample	Testing Fluid	Permeability (nD)	Test condition	Test time
PBS 1	4% NaCl Brine	342	Upstream pressure: 140psi Downstream pressure: 20psi Pressure differential: 120psi	8 minutes
	3% Surfactant solution	728	Upstream pressure: 110psi Downstream pressure: 10psi Pressure differential: 100psi	5 minutes
	Base Mud	0.17	Upstream pressure: 170psi Downstream pressure: 10psi Pressure differential: 160psi	18 hours
	Base Mud (Increase $\Delta P$ )	1.52 (Crack)	Upstream pressure: 260psi Downstream pressure: 50psi Pressure differential: 210psi	10 hours
	10 ppb Nano Mud	0.93	Upstream pressure: 140psi Downstream pressure: 20psi Pressure differential: 120psi	1 hour
PBS 2	4% NaCl Brine	81,505	Upstream pressure: 100psi Downstream pressure: 0psi Pressure differential: 100psi	9 minutes
	1% Surfactant solution	74,397	Upstream pressure: 100psi Downstream pressure: 0psi Pressure differential: 100psi	35 minutes
	10% Nanoparticle solution	16.25	Upstream pressure: 300psi Downstream pressure: 50psi Pressure differential: 250psi	20 minutes

The first Barnett shale sample, PBS 1, was tested with brine, a 3% surfactant solution, a base mud and a 10ppb nano-mud. In this test, the effect of surfactant solution on the permeability was investigated. The subsequent effectiveness of the base-mud or nano-mud is also evaluated.

Figure 5.25 shows the PPT test results of PBS 1 with brine injection. The reference permeability with brine was measured to be 342nD which was a much lower brine permeability compared with the other gas shale samples.

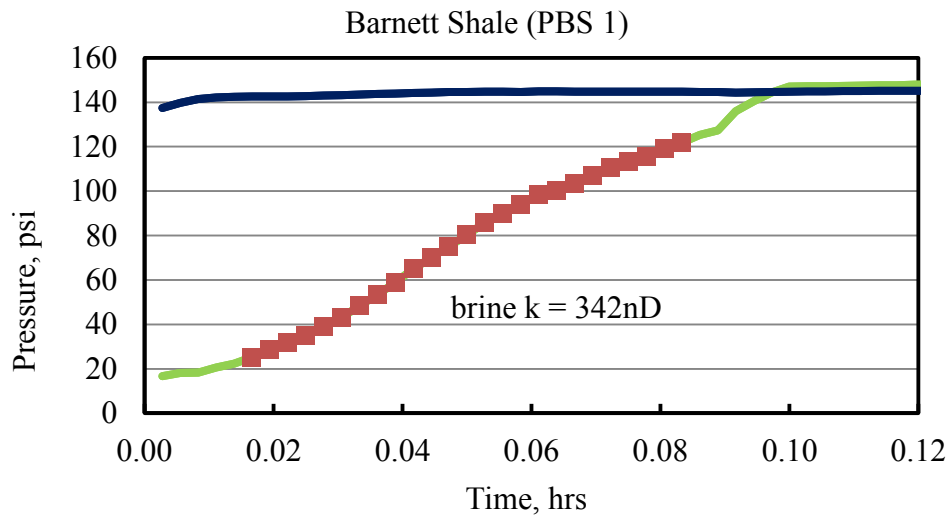


Figure 5.25: Brine permeability results of Barnett Shale (PBS 1).

After the brine test, a 3 weight % surfactant solution was injected. It was prepared by mixing 12g of surfactant with 388g of D-I water. The surfactant solution permeability was 728nD. This shows that the surfactant solution increased the fluid permeability by a factor of 2 (Figure 5.26). A likely reason for this is a change in the wettability of the shale caused by the water wetting surfactant.

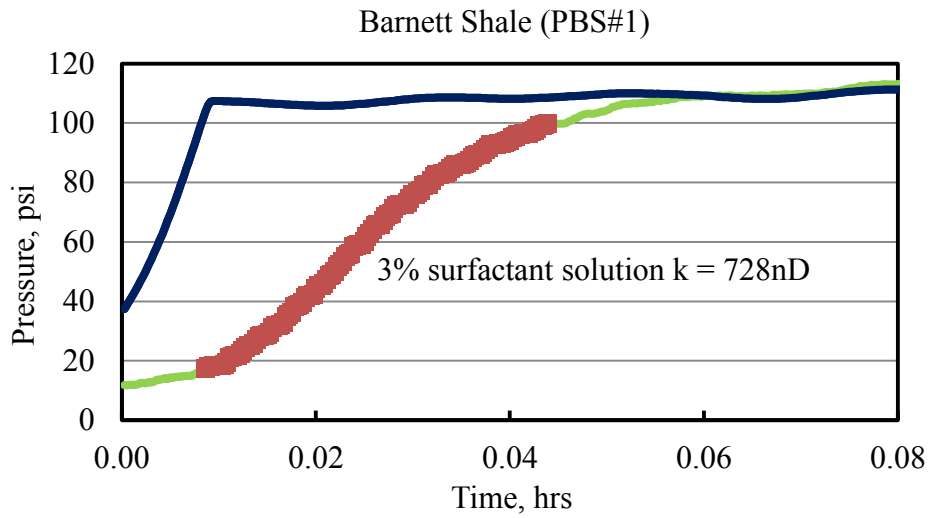


Figure 5.26: 3% surfactant solution permeability results of Barnett Shale (PBS 1).

Then the base mud was injected, and the permeability was measured to be 0.17nD which was much lower than the reference permeability. In this case, a nano mud was not needed because a sufficient permeability reduction was obtained with the base mud.

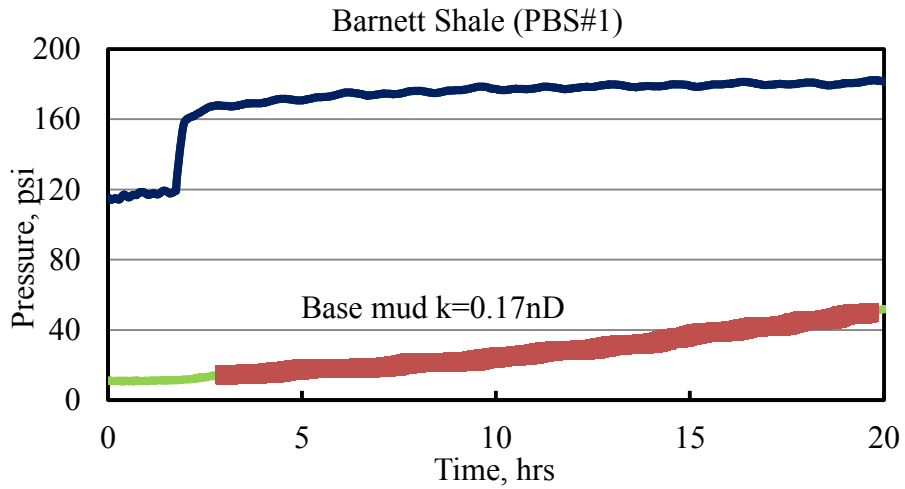


Figure 5.27: Base mud permeability results of Barnett Shale (PBS 1).

Even though, no further test was needed for this sample, the effect of the pressure differential on the permeability results was investigated. The previous test was performed at 170 psi upstream pressure and 10 psi downstream pressure, so there was a 160 psi pressure differential. The pressure differential was increased to 210 psi with 260 psi upstream pressure and 50 psi downstream pressure. Figure 5.28 shows the results of increased pressure differential when testing with base mud. The base mud permeability increased to 1.52nD, and cracks were generated after 7 hours of mud injection. Due to the crack, the flow rate at the later part was much faster than the initial test.

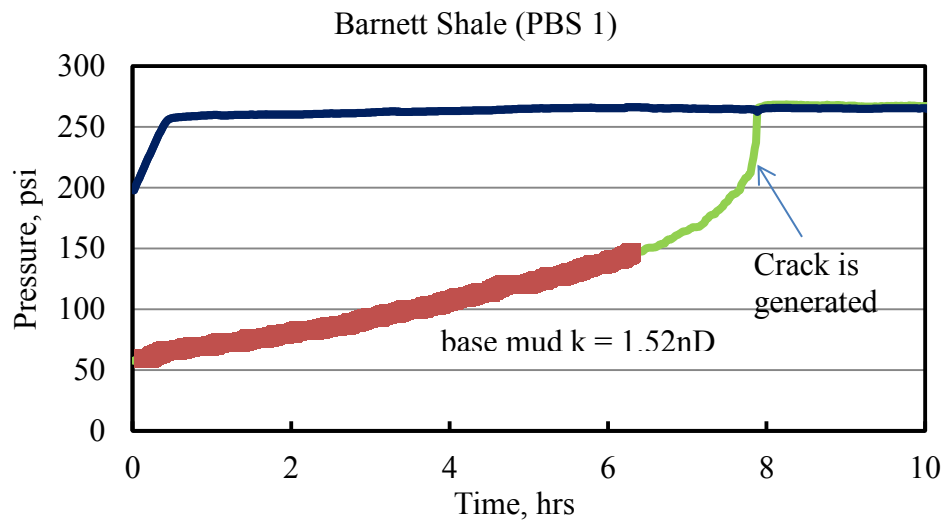


Figure 5.28: Base mud permeability results with increased pressure differential of Barnett Shale (PBS 1).

To test the fracture plugging ability of the nano-mud, a 10 ppb nano-mud was used. Figure 5.29 shows the nano mud permeability results. The permeability obtained

was 0.93nD which was similar with the second base mud test. It means that the nano mud effectively plugged the fractured shale.

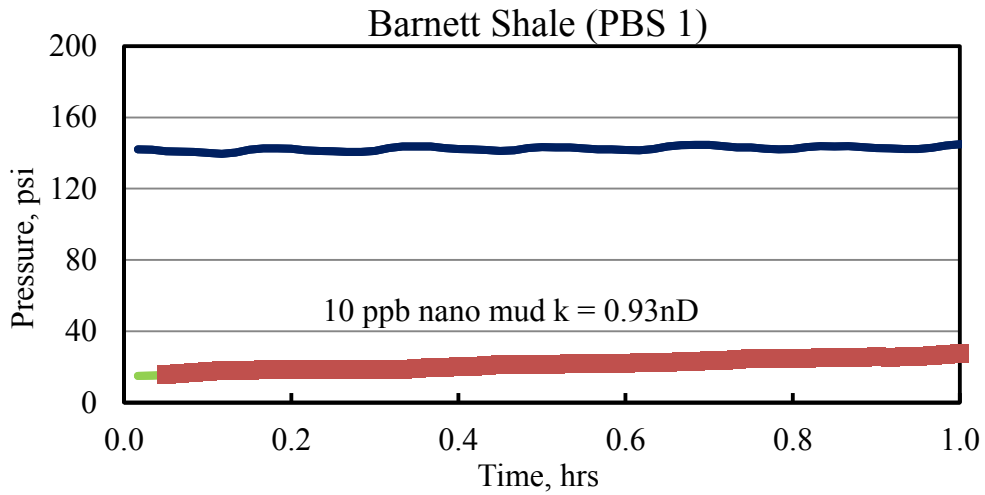


Figure 5.29: 10 ppb nano mud permeability results of Barnett Shale (PBS 1).

The second Barnett shale sample, PBS 2, was tested with brine, followed by 1% surfactant solution and 10% nanoparticle solution. In this test, the effect of mud on the permeability reduction was determined, and the effect of a 1% surfactant and a 10% nanoparticle solution was measured.

This PBS 2 sample had natural fractures, so the permeability was measured by the Darcy flow method. The reference permeability results are shown in Figure 5.30. The brine permeability was 81,505nD.

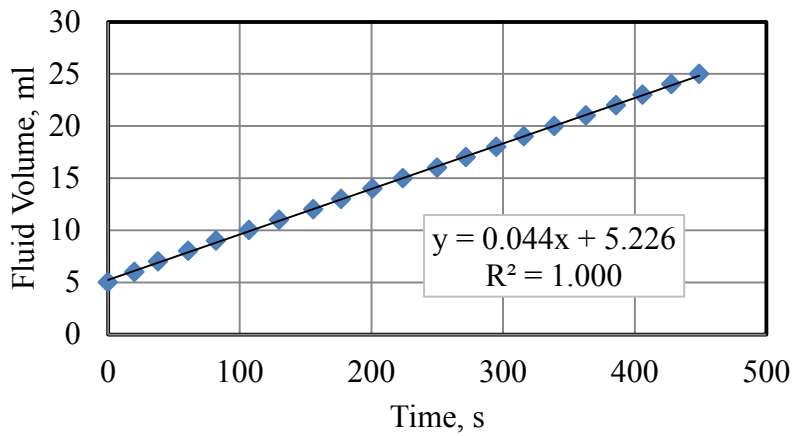


Figure 5.30: Brine permeability results of Barnett Shale (PBS 2) using Darcy flow test.

Then a 1% surfactant solution was introduced to determine whether the surfactant would plug the crack and also plug the pores of the shale sample. The surfactant solution permeability was 74,397nD which was only slightly lower than the brine permeability (Figure 5.31).

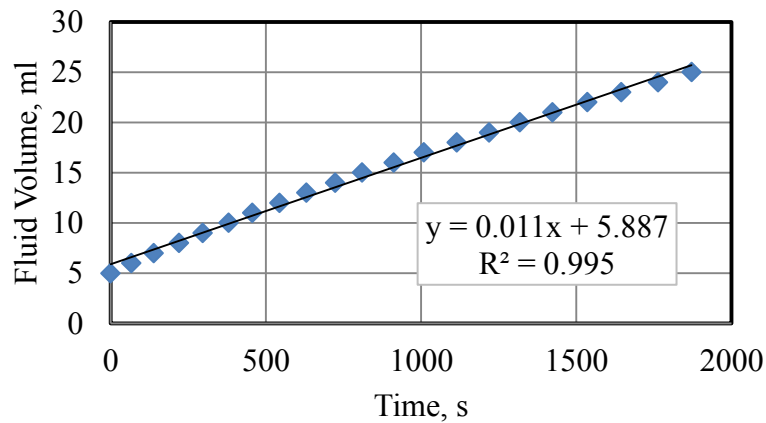


Figure 5.31: 1% surfactant solution permeability results of Barnett Shale (PBS 2) using a Darcy flow test.

Lastly, a 10% nanoparticle solution was injected to see the effect of nanoparticle plugging. The nanoparticle solution permeability was 16.25nD which was much lower than the brine and surfactant solution permeability. However, after 10 minutes of testing, the crack reopened. The permeability in the later part of the experiment was similar to the brine permeability.

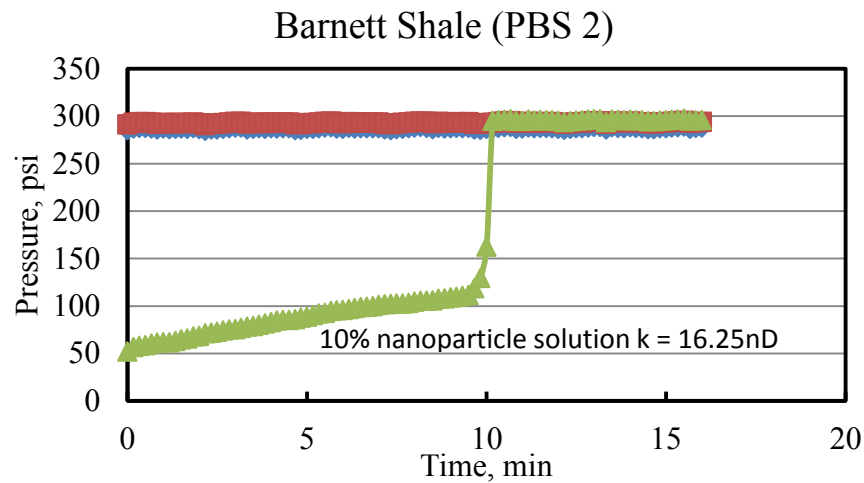


Figure 5.32: 10% nanoparticle solution permeability results of Barnett Shale (PBS 2).

#### 5.4 CONCLUSIONS

Several Texas gas shale samples were tested with brine, base-mud, and nano-muds. The test results are shown at Figure 5.33. The brine reference permeability was varied from 20 $\mu$ D to 100 $\mu$ D. When the base-mud and nano-mud systems were injected to the shale samples, the fluid permeability was reduced by an order of magnitude. The base-mud also reduced the permeability into the 20nD range. The goal of this study was to develop an impermeable barrier and reduce the permeability as much as possible. Only the nano mud showed a permeability that was reduced to less than 1nD.

A 10% nano particle solution was also tested. The solution also reduced the permeability, but the sample had a micro crack, so the nanoparticles themselves were not enough to block the micron-sized crack. To block cracks and also the pore throats, the nano particle mud mixture, which has both small and large particles, is needed.

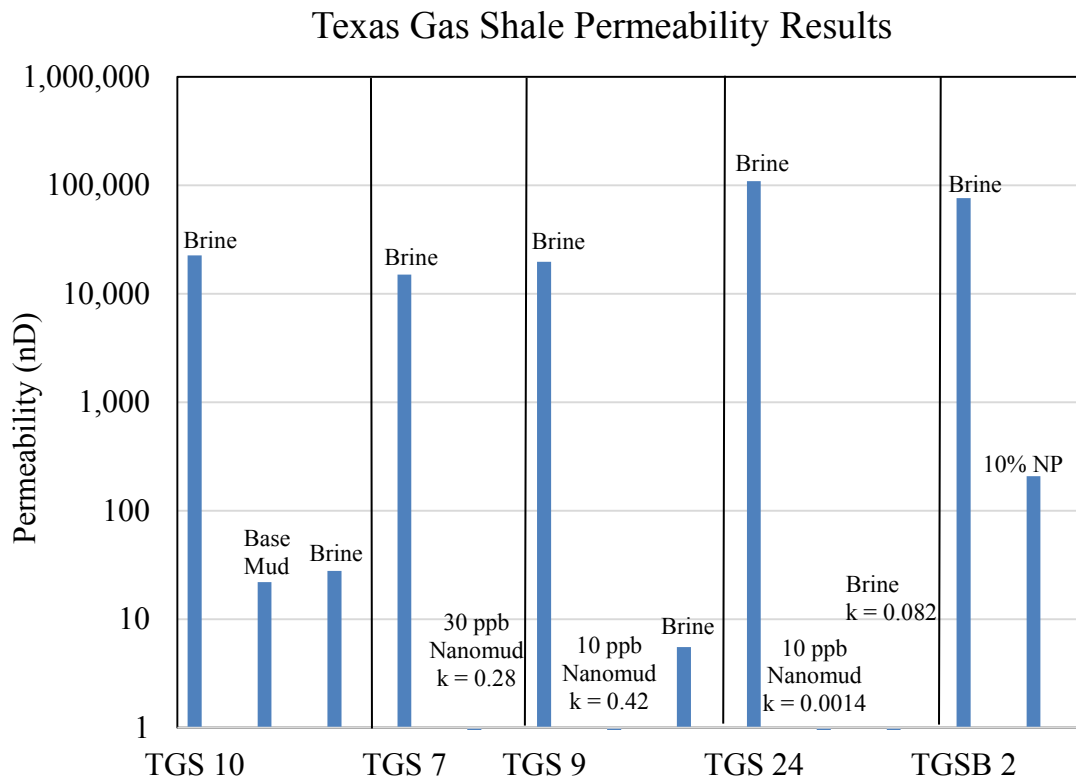


Figure 5.33: Texas Gas Shale (TGS) permeability results.

Three Eagle Ford shale samples were tested with brine, a base mud, and a 10 ppb nano-mud. The test results are shown at Figure 5.34. The brine reference permeability was varied from 50  $\mu$ D to 5 mD (sample with fractures). When the base-mud and nano-mud systems were injected, the fluid permeability was reduced by an order of magnitude.



In the WGS 32 case, the base-mud had a 3.38nD permeability, and the 10 ppb nano-mud had a 0.12nD permeability. The nano mud had significantly better plugging performance than the base mud. In the WGSB 6 case, many micro cracks were generated, and it had an extremely high permeability of 5mD. This time, we used a 10 ppb nano mud and the permeability was reduced to 0.138nD.

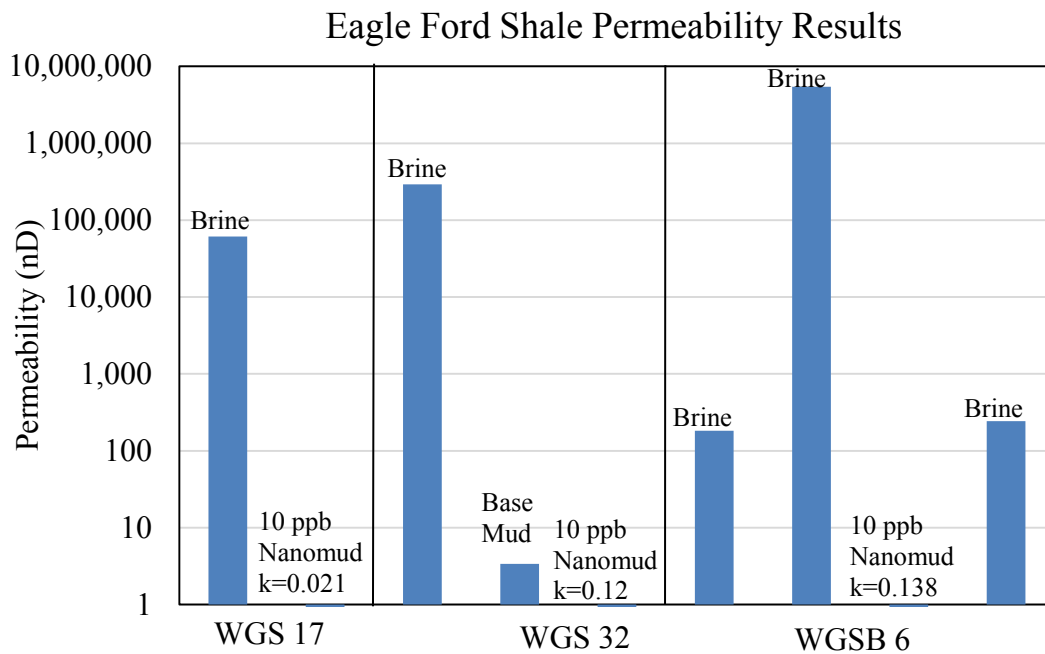


Figure 5.34: Eagle Ford Shale (WGS) permeability results.

Finally, two Barnett shale samples were also tested with brine, a base mud, a 10 ppb nano-mud and a 10% nanoparticle solution. The test results are shown at Figure 5.35. The brine reference permeability was 342nD indicating that there were no micro-cracks in the sample. Within this study, a surfactant solution that was expected to be a permeability modifier was tested, but the surfactant solution did not reduce the

permeability at all. The base mud produced enough permeability reduction for the Barnett shale. A 10% nanoparticle solution also produced a similar permeability reduction. For this low permeability shale, the nano-mud was not essential to block the pore throats.

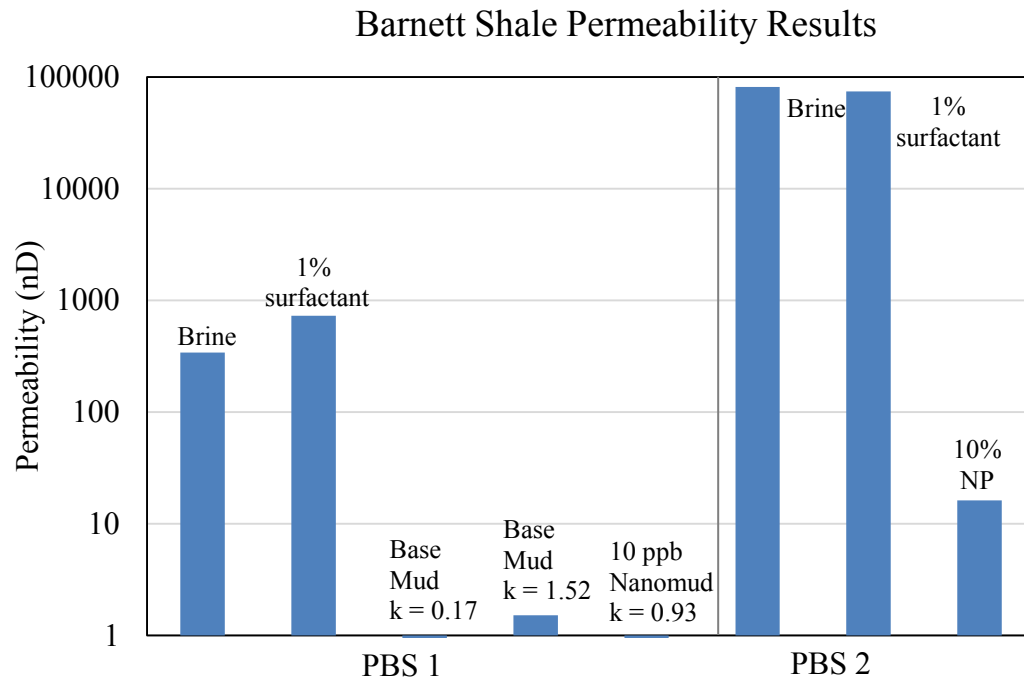


Figure 5.35: Barnett Shale (PBS) permeability results.

Based on the above test results, the following conclusions are drawn.

- With properly designed water-based muds containing nanoparticles, water invasion into shales is reduced by orders of magnitude. This implies that such muds have the potential to reduce the interaction between shales and water-based muds.
- The physical plugging by nanoparticles is durable, since the brine test after the nano-mud test still shows very low permeability compared with the original brine

permeability. There were two exceptions, TGS 24 and WGSB 6. In both these tests the durability of the nanoparticle plugs was short lived. They were not strong enough to plug the very large aperture micro cracks which had developed.

- Base mud which does not contain nanoparticles also reduces the permeability of shales, but the permeability reduction is less than with the nano-mud.
- The permeability reduction is observed for both fractured and un-fractured shales. This is important since in many instances drilling induced fractures can be a major source of wellbore instability.
- The addition of nano-particles to a water-based mud has the potential to significantly reduce water invasion into a shale and thereby reduce wellbore instability problems.
- It may be possible to drill shale wells (vertical and horizontal) with nanoparticle additives in water-based muds which have lower costs and a smaller environmental footprint than oil-based muds.

## **Chapter 6: Relative Permeability Measurement of Organic-Rich Shale**

### **6.1 INTRODUCTION**

Multi-phase fluid flow in shale reservoirs is a complex phenomenon. Many studies have been published that express this flow using theoretical and experimental approaches. For example, Darcy's law is an empirical equation invoked to calculate the ability of fluids to flow in a micro-porous material i.e. permeability. In most cases, more than one fluid exists in the reservoir, so flow interference between fluid phases is expected to occur, and the permeability of the fluid is reduced by the presence of other fluids. Relative permeability is a useful concept to quantify and explain such multiphase flow effects in a porous material. The relative permeability is defined as a ratio of the effective permeability of the given fluid to the absolute permeability of the formation rock. Relative permeability is essential for estimating productivity, injectivity, and ultimate oil recovery from reservoirs and also to plan production and diagnose the formation damage (Honarpour et al., 1988).

The most accurate way to measure the relative permeability of rocks is the steady-state method. In this method, a wetting phase fluid and a non-wetting phase fluid are injected simultaneously each at their own constant rate. The pressure drop in each phase is measured across the sample while the two phase fluids are pumped through the sample. The fluid saturations in the sample are measured by different methods. Perhaps the most accurate method is one in which the outflow fluid is collected and re-injected until a steady-state is reached. Constant pressure drop and constant saturation indicate that a steady-state has been reached.

For conventional cores, it takes several weeks to obtain the relative permeability curves. The apparent permeability of a shale is about 0.01 to 1 $\mu$ D, which is much lower than for sandstones (1 to 100mD range). Therefore, although the steady-state method is the most accurate, it takes very long even for cores with permeabilities in the 1mD range. Thus it is completely impractical when applied to ultra-low-permeability cores.

Due to the extremely low permeability of shale, determining the relative permeability in shale is very difficult. No such measurements have ever been made and reported.

An alternative way to measure relative permeability is the unsteady-state method. Using the unsteady-state method, only a few hours are needed to complete the relative permeability test for conventional cores (Welge, 1952; Johnson et al., 1959; Jones and Roszelle, 1978). In the unsteady-state method, the core is first saturated with the wetting phase, and a non-wetting phase fluid is injected until a residual saturation of the wetting phase is obtained. Next the wetting phase fluid is injected into the core at either a constant flow rate or a constant pressure drop to displace the non-wetting phase. Throughout the injection, the pressure drop and the ratio of production rates of the two phases are measured (Peters, 2012).

In this chapter, I introduce relative permeability measurements with a confining pressure (RPC) test set-up. This test set-up was developed to measure relative permeability of a shale using the unsteady-state method using a constant pressure differential. Due to the extremely low permeability of shale, it was very challenging to measure the relative permeability. In addition, the porosity of shale is about 10%, so the pore volume of a cylindrical core sample that is 1 inch in diameter and 1 inch in length is only 1.28 cc, which is very small compared to a sandstone sample. The recovered non-wetting fluid, oil, from wetting phase injection, is less than 0.5 ml, so it is hard to

measure the outflow fluid ratio. After many attempts and redesigns of the test set-up, a functioning RPC set-up was finally developed, which measures the relative permeability of shale samples. To the best of our knowledge this chapter presents the first ever reported relative permeability results for shale samples.

## 6.2 SAMPLE PREPARATION

Bakken shale was used for our relative permeability measurement. This shale has a relatively high permeability (0.1 to 1 micro-Darcy) compared to Eagle Ford or Barnett shales, so it is easier to measure relative permeability using Bakken shale samples.

### 6.2.1 Mineralogy Measurement

X-ray diffraction (XRD) and X-ray fluorescence (XRF) were used to identify the mineral composition of Bakken shales (Figure 6.1). Table 6.1 shows the mineralogy results of Bakken shale as measured using XRD and XRF.



Figure 6.1: ED-XRF handheld device.

Table 6.1: Bakken shale mineralogy results

Sample	Al	Si	Ca	Mg	Illite	Total clay	SiO <sub>2</sub>	Calcite	Dolomite	Other
Bakken	2.2	16.2	6.6	1.5	12.3	17.6	26.8	10.5	11.2	33.9

### 6.2.2 Sample dimensions

The core sample for relative permeability measurements is prepared as shown below (Figure 6.2). The cylindrical core sample has a 1 inch diameter and is 1 inch long and it has across-sectional area of 6.06 cm<sup>3</sup>. The core sample bulk volume is 12.86 cm<sup>3</sup>, and the total porosity from NMR measurements is 10%, so the pore volume is 1.286 cm<sup>3</sup>.

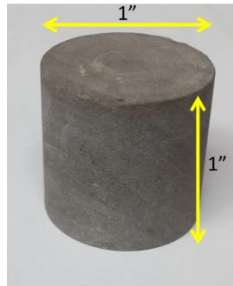


Figure 6.2: Sample dimensions for relative permeability measurements.

### 6.3 EXPERIMENTAL METHODS

There are two major steps in measuring relative permeability: first, measure the porosity and the in-situ fluid saturation change before and after the wetting phase injection, and then measure the fluid ratio and the rate of outflow during wetting-phase injection. To measure the porosity and the in-situ fluid saturation, Nuclear Magnetic Resonance (NMR) spectroscopy is used. The flow rate of the outflow fluid is measured using a core holder arranged in a particular manner referred to as the RPC set-up.

### **6.3.1 In-situ Fluid Content and Porosity Measurement using NMR Spectroscopy**

Conventional characterization methods such as the retort test cannot adequately measure the in-situ fluid content of shale due to the extremely low permeability of shale. Thus, other possible approaches such as thermal gravimetric analysis (TGA) and Pyrolysis-gas-chromatography-mass spectrometry (Py-GC-MS) were tested. These are destructive methods, and liquid evaporation occurred during the sample preparation process. The shale sample needs to be broken into powder to run Py-GC-MS, and during the procedure, some of in-situ fluid evaporated; thus, in-situ saturation is inaccurately measured. In addition, after this test, following tests cannot be run due to the destruction of the sample (Gips et al., 2014).

On the other hand, NMR spectroscopy is a non-destructive method, so further experiments can be run on the same sample after the fluid saturation measurement. No evaporation occurs during the test if the sample is properly wrapped during the measurement. NMR is widely used in the oil and gas industry for measuring porosity and fluid saturation of formations. Thus, the NMR method was used because it effectively measures the in-situ fluid content and the neutron porosity of shale without core destruction. The longitudinal ( $T_1$ ) and transverse ( $T_2$ ) relaxation time measurements using NMR, and the porosity and the in-situ fluid saturation are all calculated on the basis of relaxation times.

Figure 6.3 shows the NMR core analyzer, GeoSpec2, obtained from Oxford Instruments, which was used for measuring  $T_1$  and  $T_2$  relaxation times.





Figure 6.3: NMR core analyzer (Oxford Instruments, GeoSpec2).

By understanding the effects of  $T_1$  and  $T_2$  relaxation times, fluid saturations and also porosity were calculated. From the  $T_2$  echo train raw data, echo-fit mapping, which can then be converted to a  $T_2$  distribution diagram related to neutron porosity was obtained. Figure 6.4 shows Bakken shale's  $T_2$  distribution chart. The area under the curve represents the pore space of the sample, and porosity from the given bulk volume was calculated (Gibs et al., 2014).

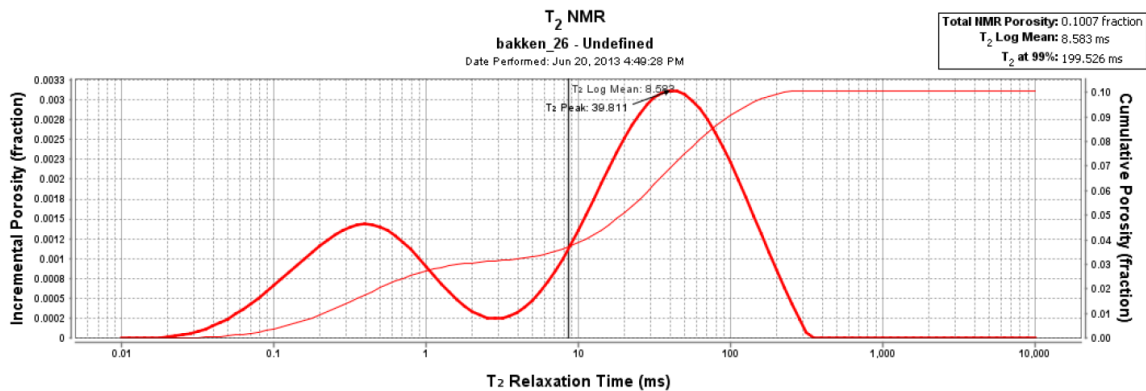


Figure 6.4: Bakken shale sample -  $T_2$  Distribution Chart (Gibs et al., 2014).

In-situ fluid saturation of shale is much harder to measure than porosity. The 2-D mapping and an understanding of wettability are essential. Cao Minh et al. (2012) used the 2-D map of diffusion versus  $T_2$  and their advanced diffusion model for the fluid

identification. The authors of that study added a wettability factor at the  $T_2$  surface calculation from considering the viscosity difference of fluid. A  $T_1$  vs.  $T_2$  plot and a  $T_1/T_2$  ratio vs.  $T_2$  plot are used for calculating the in-situ fluid contents (Figure 6.5). Lewis et al. (2013) showed the correlation between these plots and fluid properties in the Eagle Ford shale. In their paper, free oil in large pores was detected when there were longer  $T_1$  and  $T_2$  times and the ratio reached approximately 1. On the other hand, organic matter, such as kerogen in small pores, was detected where there was a short  $T_2$  time and a high  $T_1/T_2$  ratio.

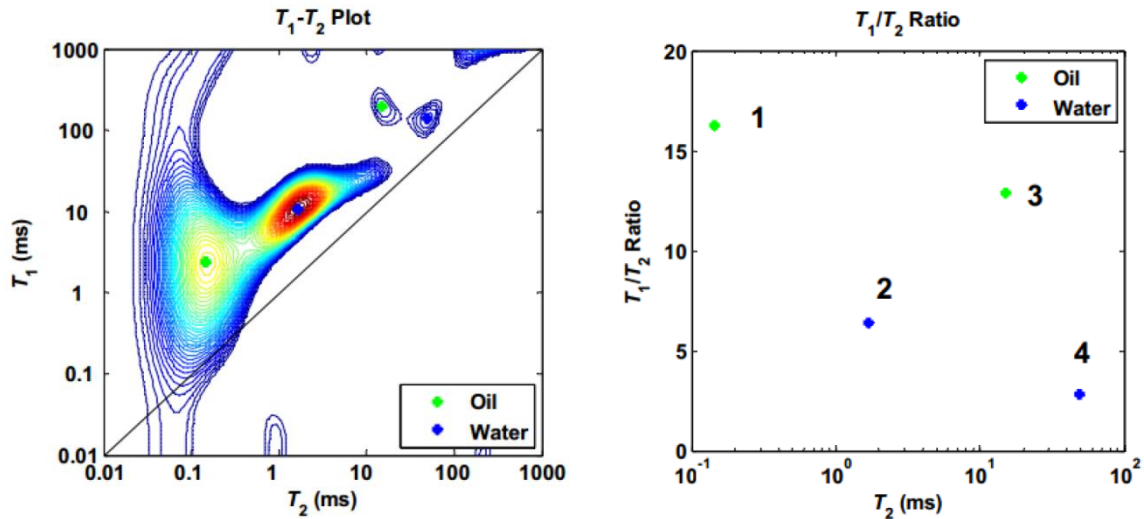


Figure 6.5:  $T_1$  vs.  $T_2$  plot (left), and  $T_1/T_2$  ratio vs.  $T_2$  plot (right) (Lewis et al., 2013).

To calculate the saturation of oil and water, the distribution of  $T_2$  is separated. In Figure 6.6, the blue line shows the NMR results after NaCl brine was injected into the oil-saturated Bakken shale. The left peak shows the pore volume that is saturated with brine, and the right peak shows the pore volume that is saturated with oil. However, the two peaks were not fully divided, so the exact saturation amount cannot be obtained. For that reason, 1 weight %  $MnCl_2$  brine was injected into the core instead of 4 weight %

NaCl brine. The resulting curve is fully divided into two separate peaks, so the exact brine and oil saturation inside the sample can be calculated.

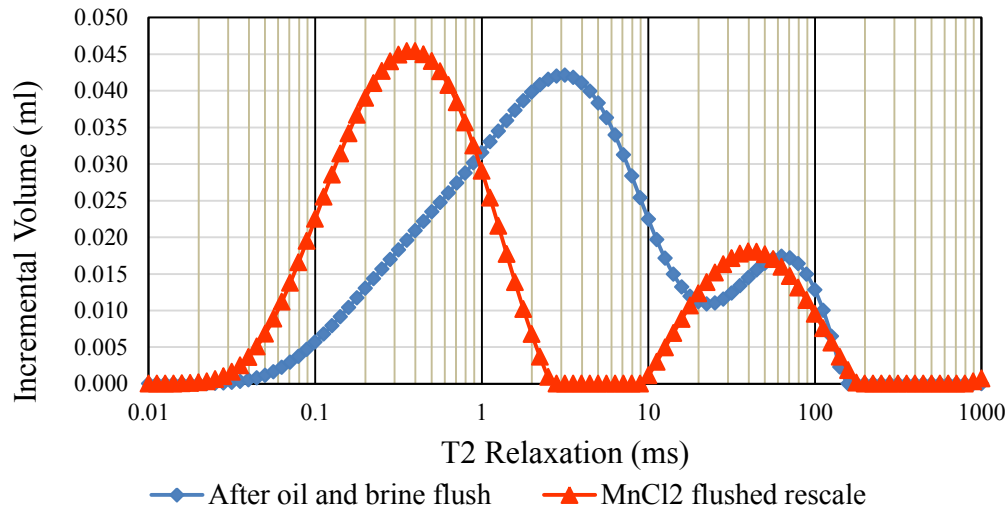


Figure 6.6:  $T_2$  distribution chart change due to the  $MnCl_2$  flushing, Bakken shale sample.

The peak separation is maintained even though we injected other fluids after  $MnCl_2$  brine injection. After the first  $MnCl_2$  brine flood, the core sample was saturated with decane again. The in-situ fluid saturation was measured again to calibrate the maximum oil saturation and minimum water saturation. Figure 6.7 shows the results before and after the oil flooding. After  $MnCl_2$  brine flooding, the water saturation (red left peak) of the core sample was high, and the oil saturation (red right peak) of the core sample was low. After decane flooding, the two peak heights reversed: the water saturation of the core sample was low, and the oil saturation of the core sample was high.

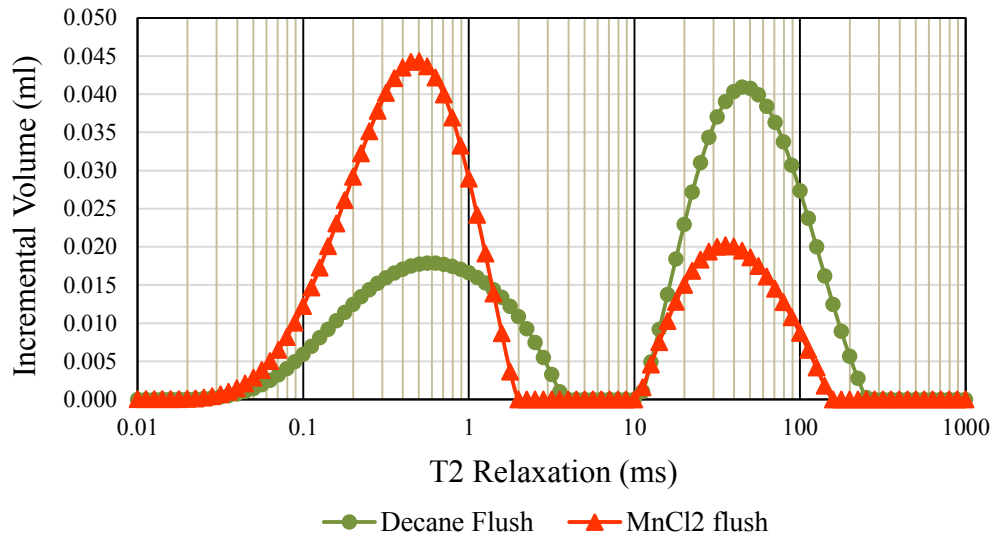


Figure 6.7:  $T_2$  distribution change after decane injection, Bakken shale sample.

The use of  $MnCl_2$  in the brine provided a new reliable method for measuring the oil and water saturations in the core at any point in the relative permeability experiments. This proved to be extremely useful in estimating average fluid saturations in the core at different stages in the relative permeability experiment.

### 6.3.2 Outflow Rate and Ratio of Production Fluid Measurement Using RPC Set-up

Figure 6.8 shows the schematic of the RPC set-up, and Figure 6.9 shows a photograph of the RPC set-up. Two pressurized vessels are used to inject a non-wetting phase into the shale, and only one pressurized vessel is used to inject wetting phase fluid into the shale. Originally, a syringe pump was set to inject the displacing fluid, but the syringe pump leaked ever so slightly. The injection flow rate was extremely small and the injection pressure was relatively high and any leak at all was unacceptable during the test. For this reason, pressurized vessels with a high-pressure nitrogen gas tank was introduced

to maintain constant injection pressure and to inject testing fluid. This system provided the most reliable injection method without leakage.

Two different sizes of pressurized vessels were used to inject fluid into the core holder. The larger vessel, which has about 2 L volume, was connected to a nitrogen tank, and 100 ml of red-dyed  $\text{MnCl}_2$  brine was added into the vessel. The rest of the empty space is filled with nitrogen gas. The smaller vessel, which has about 45 ml volume, was fully filled with decane. The solubility of nitrogen gas in decane is much higher than the solubility of nitrogen gas in water, so the direct contact of nitrogen gas with decane was prevented using a fluid barrier, brine. The pressurized nitrogen gas pushes brine toward the small vessel, and the brine pushes decane toward the core sample.

A shale core sample was placed in the core holder which provides a rubber sleeve around the core. Between the rubber sleeve and inner surface of the core holder, oil was used as a confining fluid using a mechanical pump. The oil maintains a constant confining pressure during the experiment.

The outflow was gathered in a small graduated cylinder or syringe, and the collected fluid volume was monitored with an IP camera and a time-lapse video capturing program. From the video, the outflow oil and water ratio and their amounts were recorded on an Excel spreadsheet, and the relative permeability was calculated.

It was very difficult to measure the exact outflow ratio and amounts versus time due to the extremely slow outflow rate, which is less than  $5 \mu\text{L}/\text{min}$ . When the outflow volume was not the same as the injection volume, it was found that the outflow had not flowed through the pipe, but it had instead attached to the lower surface of the sample. In this case, the gravity force at the outflow was less than the attraction force between the shale surface and the outflow fluid. To prevent this problem, a syringe pump was attached to the outflow end of the core and brine was continuously injected at a fixed rate

across the outlet face of the core at  $5 \mu\text{L}/\text{min}$ , which is the approximately equal to the superficial velocity of outflow. Due to this modification, the outflow fluid from shale moved much more easily, and the proper outflow ratio was obtained for the shale. The volume of the circulating fluid was subtracted from the measured volume collected to obtain the true outflow from the core.

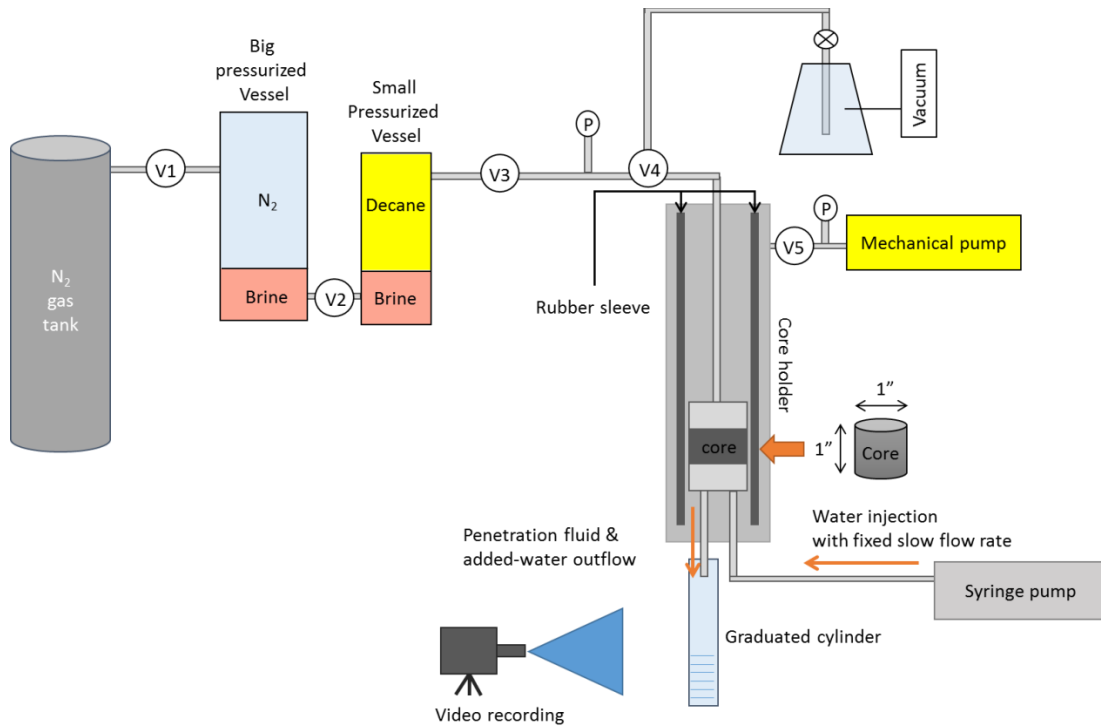


Figure 6.8: A schematic of the RPT set-up.

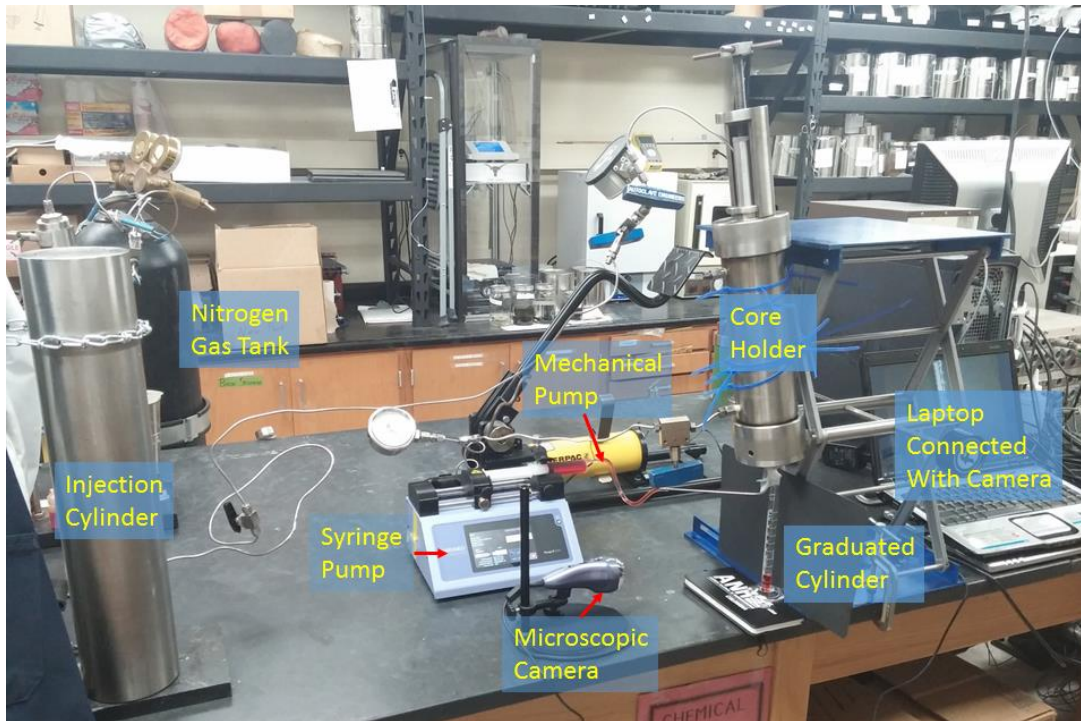


Figure 6.9: Photograph of the RPT set-up in the laboratory.

### 6.3.3 Experimental Procedures

A cylindrical shale core sample 1 inch in diameter and 1 inch in length was prepared. First, the sample was saturated with decane, which is a type of light oil. We inserted the sample into the core holder, and then closed the inlet and the outlet of the core holder. Using the mechanical pump, the confining pressure was increased to 2000 psi, and valve 5 (V5) was closed. Then 100 ml of red-dyed  $\text{MnCl}_2$  brine was added into the big vessel, and valve V2 was closed. Decane was added into the small vessel, and valve V3 was closed. V4 is a three-way valve. We opened V4 in the direction of the vacuum pump and vacuumed the air of the injection line for 2 minutes, and then closed V4. After that, V1 was opened and nitrogen gas was injected until the system pressure reached 800 psi. We then closed V1 and released the pressure of the nitrogen gas tank. We put a 10 ml graduated cylinder at the outlet of the core holder and covered the

connection with parafilm to prevent the evaporation of collected fluid. We then started to run outflow brine injection using the syringe pump. Pump rate was set as 5  $\mu\text{l}/\text{min}$ , and the target volume was set as 7 ml. After that, we opened V2 and V3 and started the decane injection, and we monitored outflow using a time-lapse video capturing program. After we collected more than 5 ml of oil, the oil saturation procedure ended. We then opened V1 to release the injection pressure, and we opened V5 and released the confining pressure. We opened the inlet and the outlet of the core holder and took the sample out and cleaned the surface with a paper towel. We also cleaned the inside of the core holder with a paper towel to remove leftover fluid.

After the saturation of core with oil, water-flooding (brine-flooding) was begun, i.e. we injected a wetting fluid, brine, to produce the non-wetting phase, oil. We inserted the core into the core holder again. We closed the inlet and the outlet, introduced the confining pressure, and closed V5. We closed V2 and V3 and then detached the small vessel. We then opened V4 and ran the vacuum and closed V4. We opened V1 and injected nitrogen gas and set the pressure as 600 psi, and then closed V1 and released the pressure of nitrogen tank. We poured 1 ml of dyed brine into the graduated cylinder; because there is no gauge for amounts smaller than 1 ml, we could not measure the exact amount of produced fluid below 1 ml. We put the cylinder at the outflow and covered the top with parafilm. We started to inject outflow brine. We opened V2 and V3 to inject brine. The outflow was monitored using the time-lapse video capturing program, VideoVelocity. The experiment continued until no more oil came out from the sample. After that, we took out the sample and measured in-situ fluid saturation using NMR spectroscopy to calibrate the irreducible oil saturation and the maximum water saturation.

Figure 6.10 shows the time-lapse video capture program. The time gap was set as 5 minutes, and we obtained a 12-second-video for every 1 hour.





Figure 6.10: Time-lapse video capture program, VideoVelocity.

Figure 6.11 shows the collected oil and water in the graduated cylinder. Because red dye was applied to the brine, the produced oil and water are easily distinguished.

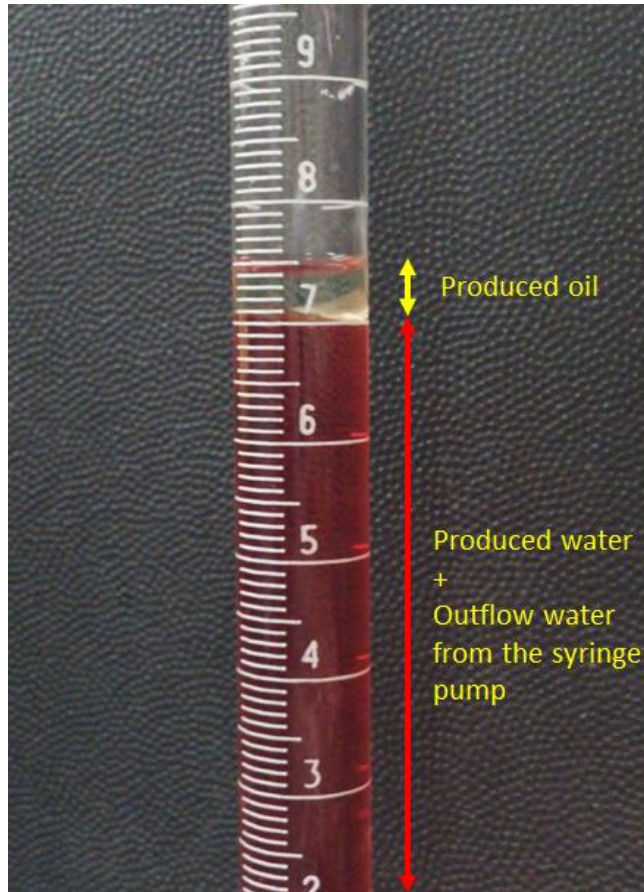


Figure 6.11: Collected oil and water at the water-flooding experiment.

Using the video results, the volumes of oil and water outflow collected are recorded and plotted. Figure 6.12 shows a sample of the original experimental data. At the start of the water-flooding, only oil came out from the sample. After 5 hours of injection, water started to be collected along with oil. After 7 hours injection, only water came out from the sample. The resulting graph is not smooth, due to noise. To calculate relative permeability, the derivative of these cumulative volumes needs to be taken. To accomplish this, the experimental results need to be smoothed to reduce the noise.

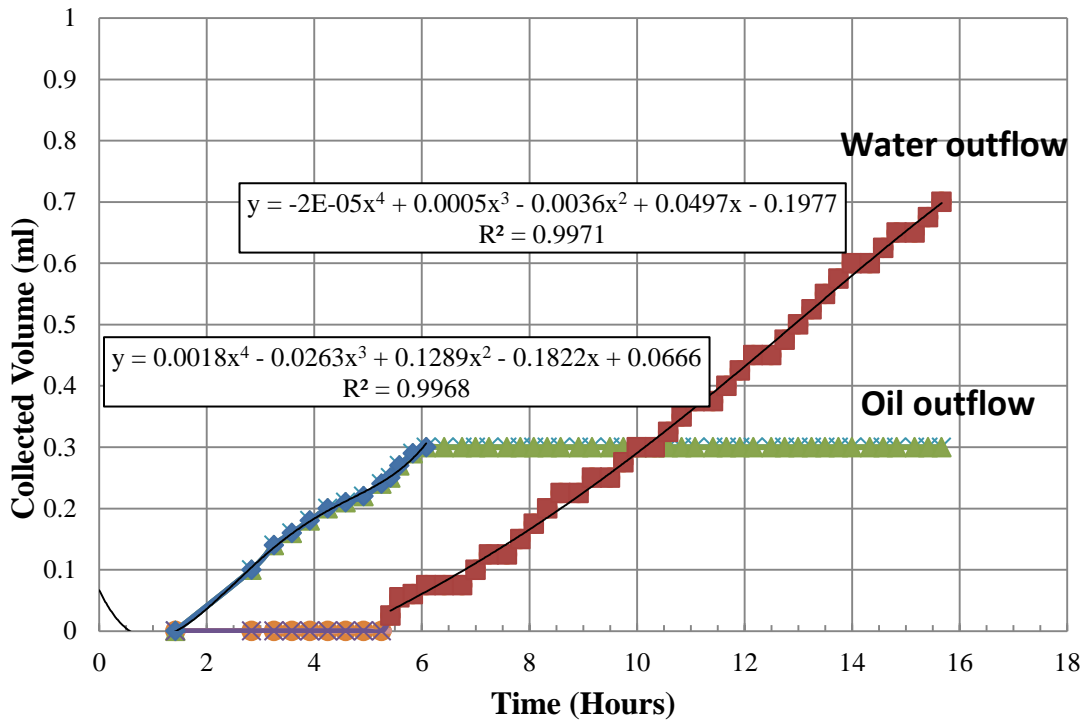


Figure 6.12: Original experimental data, first water-flood, Bakken Shale (EBS-1).

In Figure 6.12, trend lines show the first part of the oil outflow and the later part of the water outflow. Using equations derived from the trend line, the smoothed version of the experimental results were obtained (Figure 6.13), in order to calculate the relative permeability.

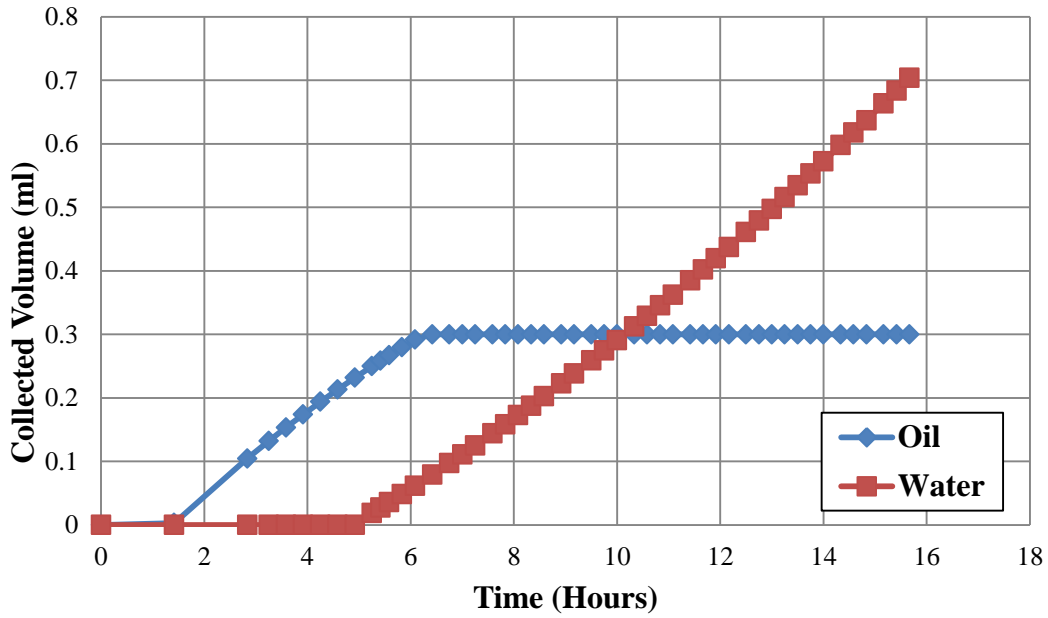


Figure 6.13: Smoothed experimental data, first water-flood, Bakken Shale (EBS-1).

### 6.3.4 Relative Permeability Calculation using the Johnson-Bossler-Neumann (JBN) Method

The relative permeability calculation from the unsteady-state method was developed by Welge (1952) and Johnson, Bossler, and Neumann (1959), and the procedures are outlined by Peters (2012). To calculate the relative permeability, the following variables need to be calculated:  $W_i$ ,  $N_{pD}$ ,  $\Delta P$ ,  $f_{nw2}$ ,  $S_{w2}$ ,  $I_r$ , and  $f_{nw2}/k_{rmw}$ .

$W_i$  is the injected wetting fluid volume divided by the pore volume. In the current system, injected volume is unknown, so the injected volume was assumed to be the same as the produced volume.

$$W_i = \frac{V_{injected}}{V_{pore}} = \frac{V_{produced}}{V_{sample,bulk} \times \phi} \quad (1)$$

$N_{pD}$  is the produced oil volume divided by the pore volume, and it can be calculated using this equation:

$$N_{pD} = \frac{V_{produced\ oil}}{V_{pore}} = \frac{V_{produced\ oil}}{V_{sample,bulk} \times \emptyset} \quad (2)$$

$\Delta P$  is the differential pressure, and in our results, it was not changed during the test. During the water-flooding, the injection pressure was 600 psi, and the outflow was open to the air, so the differential pressure was 600 psi.

Peters and Khataniar (1987) suggested the calculation of  $f_{nw2}$  from the curve fits of  $N_{pD}$  versus  $\ln W_i$ . Figure 6.14 shows the graph of  $N_{pD}$  versus  $\ln W_i$  and the trend line. The constants of equation (3) are used for the calculation of  $f_{nw2}$ .

$$N_{pD} = A_1 + A_2 \times \ln W_i + A_3 \times (\ln W_i)^2 \quad (3)$$

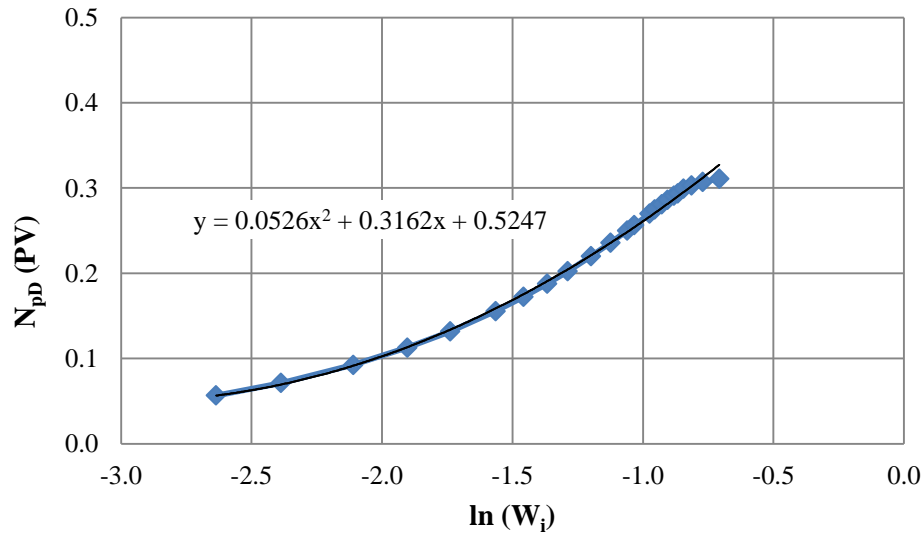


Figure 6.14: Curve fit of the  $N_{pD}$  vs.  $\ln(W_i)$  example.

Inserting  $A_2$  and  $A_3$  values of equation (3) into equation (4), then get  $f_{nw2}$ .

$$f_{nw2} = \frac{q_{nw}}{q} = \frac{dQ_{nw}(t)}{dQ_i(t)} = \frac{dN_{pD}}{dW_i} = \frac{A_2 - 2 \times A_3 \times \ln W_i}{W_i} \quad (4)$$

The wetting phase saturation can be calculated with equation (5). Although the initial water saturation was unknown, the final water saturation was obtained from the NMR measurement after the water-flooding. After the initial water saturation was calculated,  $S_{w2}$  was calculated for every end point condition for the relative permeability calculation.

$$S_{w2} = S_{w,initial} + \frac{V_{produced\ oil}}{V_{pore}}, \quad S_{w,final} - \frac{V_{produced\ oil}}{V_{pore}} = S_{w,initial} \quad (5)$$

The relative injectivity ratio is defined in equation (6):

$$I_r = \frac{\left(\frac{q}{\Delta P}\right)}{\left(\frac{q}{\Delta P}\right)_s} = \frac{\left(\frac{q}{\Delta P}\right)}{\frac{kA}{\mu_{nw}L}} \quad (6)$$

From the curve fits of  $\ln\left(\frac{1}{W_i I_r}\right)$  versus  $\ln\left(\frac{1}{W_i}\right)$ , the trend line equation (7) is acquired.

$$\ln\left(\frac{1}{W_i I_r}\right) = B_1 + B_2 \times \ln\left(\frac{1}{W_i}\right) + B_3 \times \left[\ln\left(\frac{1}{W_i}\right)\right]^2 \quad (7)$$

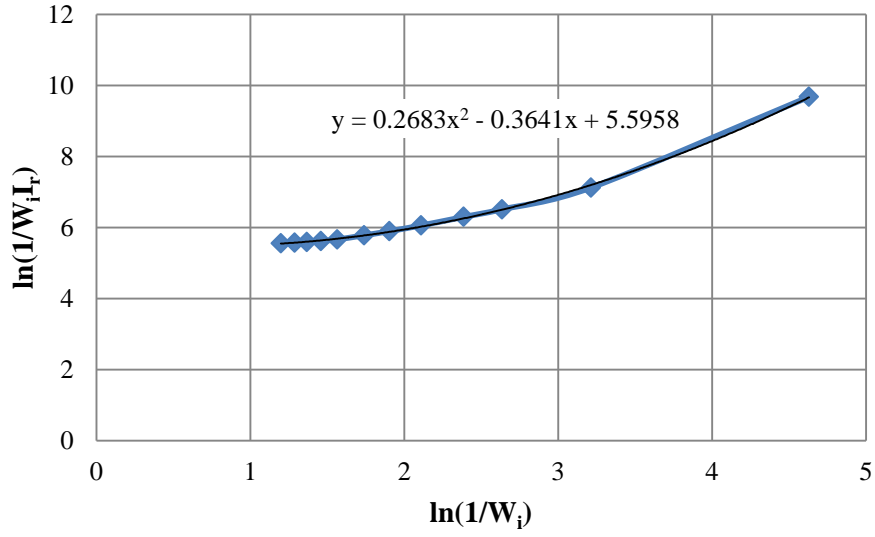


Figure 6.15: Example curve fit of  $\ln\left(\frac{1}{W_i I_r}\right)$  vs.  $\ln\left(\frac{1}{W_i}\right)$ .

The constants of the trend line;  $B_1$ ,  $B_2$  and  $B_3$  are inserted into equation (8).

$$\frac{f_{nw2}}{k_{rnw}} = \frac{d\left(\frac{1}{W_i I_r}\right)}{d\left(\frac{1}{W_i}\right)} = \left[ \frac{B_2}{\left(\frac{1}{W_i}\right)} + \frac{2 \times B_3 \times \ln\left(\frac{1}{W_i}\right)}{\left(\frac{1}{W_i}\right)} \right] e^{\left( B_1 + B_2 \times \ln\left(\frac{1}{W_i}\right) + B_3 \times \left[ \ln\left(\frac{1}{W_i}\right) \right]^2 \right)} \quad (8)$$

The relative permeability of the non-wetting phase i.e. the oil relative permeability, can be calculated using equation (9).

$$k_{rnw} = \frac{f_{nw2}}{\frac{d\left(\frac{1}{W_i I_r}\right)}{d\left(\frac{1}{W_i}\right)}} \quad (9)$$

The relative permeability of the wetting phase, i.e. the water relative permeability, can be calculated using equation (10).

$$k_{rw} = \frac{\mu_w}{\mu_{nw}} \left( \frac{1}{f_{nw2}} - 1 \right) k_{rnw} \quad (10)$$

#### 6.4 EXPERIMENTAL RESULTS

Two Bakken shale samples, EBS-1 and EBS-2, were tested. Two similar samples were prepared from the same core at the same formation depth and with similar mineralogy, so both samples should show similar relative permeability.

Figure 6.12 shows the first water-flooding test results of EBS-1, and Table 6.2 shows the calculation results of the variables and relative permeability at a superficial velocity of 0.003 m/d. Superficial velocity is calculated using equation (11).

$$u_s = \frac{Q}{A} = \frac{1.0039 \text{ cm}^3 / 56400 \text{ sec}}{5.0645 \text{ cm}^2} = 0.003 \text{ m/d} \quad (11)$$



Table 6.2: Calculation sheet of the first water-flood results, EBS-1.

Wi(PV)	NpD (PV)	ΔP (psi)	1/Wi	ln(Wi)	ln(1/Wi)	fnw2	Sw2	q/Δp	lr	1/(Wi*lr)	ln(Δ/Wi*lr)	fnw2/kmw	krmw	krw
0.000	0.000	593					0.57		0.000					
0.002	0.002	593	452.024	-6.114	6.114	246.175	0.572	1.38E-08	0.033	13795.907				
0.081	0.081	593	12.328	-2.512	2.512	2.300	0.651	4.94E-07	1.169	10.549	2.356	0.12594313		
0.103	0.103	593	9.752	-2.277	2.277	1.592	0.673	4.56E-07	1.079	9.038	2.201	0.61581236	2.585628186	
0.119	0.119	593	8.396	-2.128	2.128	1.246	0.689	4.40E-07	1.042	8.056	2.086	0.94616693	1.316868121	
0.135	0.135	593	7.400	-2.001	2.001	1.005	0.705	4.26E-07	1.010	7.329	1.992	1.19743861	0.839431445	
0.151	0.151	593	6.637	-1.893	1.893	0.830	0.721	4.13E-07	0.977	6.793	1.916	1.37345182	0.604233673	0.134629182
0.166	0.166	593	6.036	-1.798	1.798	0.698	0.736	3.99E-07	0.944	6.392	1.855	1.48654169	0.469393022	0.220988333
0.180	0.180	593	5.551	-1.714	1.714	0.595	0.750	3.85E-07	0.912	6.088	1.806	1.55051293	0.384014808	0.283622884
0.209	0.194	593	4.792	-1.567	1.567	0.444	0.764	7.59E-07	1.796	2.668	0.981	1.57775524	0.281386838	0.383070687
0.222	0.201	593	4.504	-1.505	1.505	0.390	0.771	7.08E-07	1.677	2.686	0.988	1.55795892	0.250086938	0.425846206
0.235	0.208	593	4.251	-1.447	1.447	0.343	0.778	7.05E-07	1.669	2.547	0.935	1.52408087	0.225168434	0.468439922
0.255	0.217	593	3.921	-1.366	1.366	0.285	0.787	7.00E-07	1.658	2.364	0.861	1.45503461	0.195975101	0.534014973
0.275	0.227	593	3.641	-1.292	1.292	0.238	0.797	6.95E-07	1.646	2.212	0.794	1.37264926	0.173363848	0.603428672
0.295	0.233	593	3.392	-1.221	1.221	0.198	0.803	5.37E-07	1.272	2.665	0.980	1.28039059	0.15441362	0.681084843

Table 6.3 shows the in-situ fluid saturation of EBS-1 sample before and after water-flooding. Due to the water-flooding, oil saturation decreased from 0.43 to 0.19, and water saturation was increased from 0.57 to 0.81.

Table 6.3: In-situ fluid saturation change of the first water-flood results, Bakken Shale (EBS-1).

Status	Oil Saturation ( $S_o$ )	Water Saturation ( $S_w$ )
Before water-flooding	0.43	0.57
After water-flooding	0.19	0.81
Change	(-) 0.24	(+) 0.24

Figure 6.16 shows the relative permeability result of EBS-1 at the first water-flooding. As water saturation was increased, the oil permeability was decreased, and the water permeability was increased. Craig (1971) presented several rules of thumb and his second rule of thumb is that the saturation at which oil and water relative permeabilities are equal would be greater than 50% water saturation in strongly water-wet rock (see Chapter 2). In Figure 6.16, the crossover point, where the water and oil permeabilities are equal, occurs at water saturation of about 75%, suggesting that this core sample is strongly water-wet. The crossover points of all tests which were performed here showed a crossover point of around 75%, and this strongly suggests that all the Bakken shale samples in this study are water-wet. This is consistent with other observations made in the literature which have pointed out that the Middle Bakken is a reservoir for oil that originated in the Lower Bakken layers i.e. it is not the source rock. Being originally water saturated and being filled by a drainage process it is expected to be water wet. .

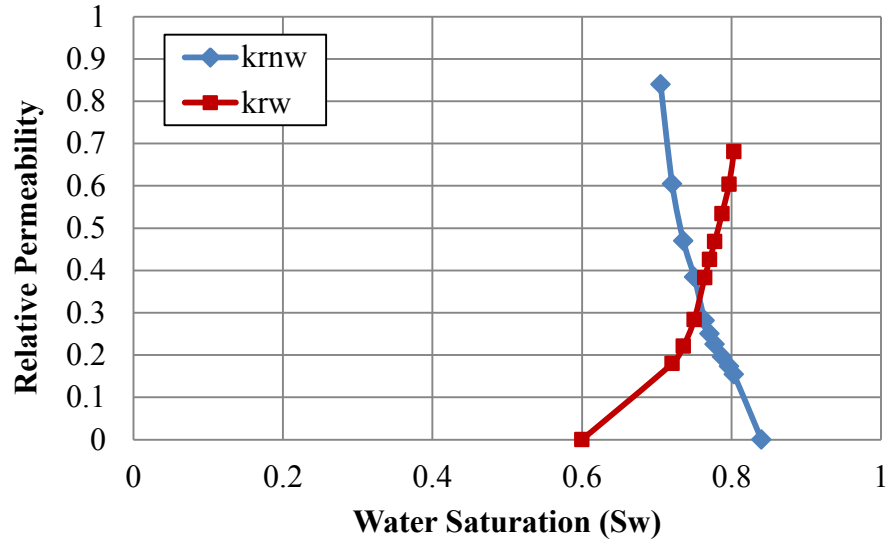


Figure 6.16: Relative permeability curve, first water-flood, Bakken Shale (EBS-1).

After the first water-flooding, the in-situ fluid saturation was measured to calibrate the minimum (irreducible) oil saturation and the maximum water saturation. When the sample was re-saturated with decane, the maximum oil saturation and the irreducible water saturation were measured.

The relative permeability results of EBS-1, can be fit with an modified Brooks-Corey equation (Goda and Behrenbruch, 2004),

$$k_{ro} = k_{ro,max} \left( \frac{S_o - S_{or}}{1 - S_{or} - S_{w,irr}} \right)^{n_o}$$

$$k_{rw} = k_{rw,max} \left( \frac{S_w - S_{w,irr}}{1 - S_{or} - S_{w,irr}} \right)^{n_w}$$

The exponents  $n_o$  and  $n_w$  range from 1 to 6, and the maximum relative permeabilities,  $k_{ro,max}$  and  $k_{rw,max}$  are between 0 and 1.

Figure 6.17 shows the fit of the oil relative permeability between measured values and equation calculated values. For this set of data, modified Brooks-Corey equation

provides a reasonable fit with EBS-1 water and oil relative permeability throughout most of the investigated range of water saturations.

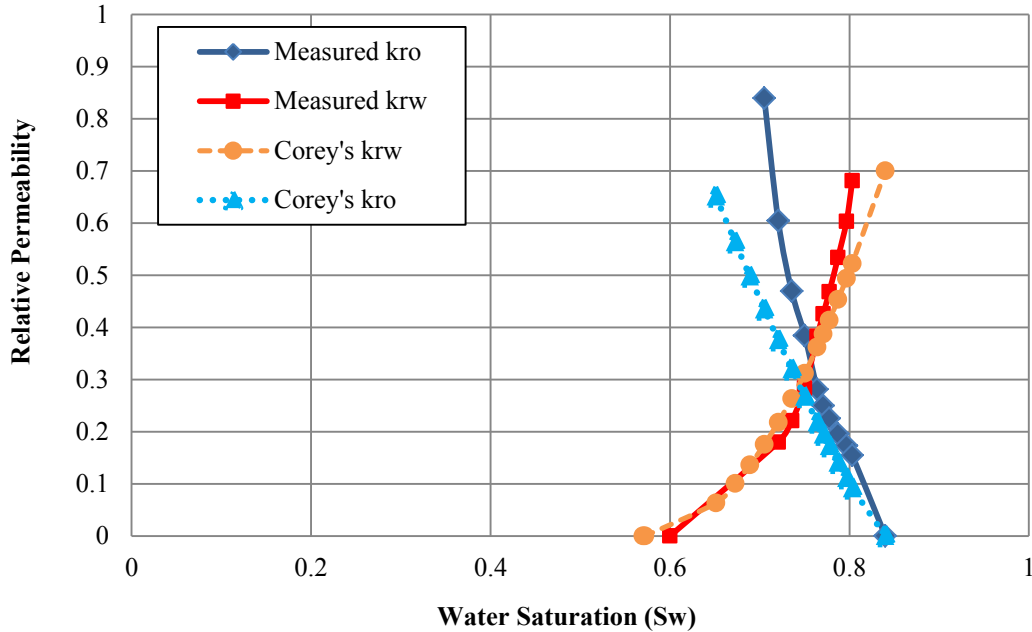


Figure 6.17: Relative permeability comparison with Brooks-Corey equation's results.

A second water-flood with EBS-1 was performed to see how much difference was generated in the relative permeability. Figure 6.18 shows the outflow analysis result of EBS-1 for the second water-flood. This time, water and oil were observed in the outlet right from the start. The water outflow rate was slow at first, and it increased later in the experiment. This may occur because of capillary end effects during the forced injection or due to incomplete displacement of the water during the oil flood. The reasons are unclear at this point. However, the relative permeability results from the second waterflood differ from the results of the first water-flood. Figure 6.19 shows the smoothed version of the experimental results using the trend line of Figure 6.18.

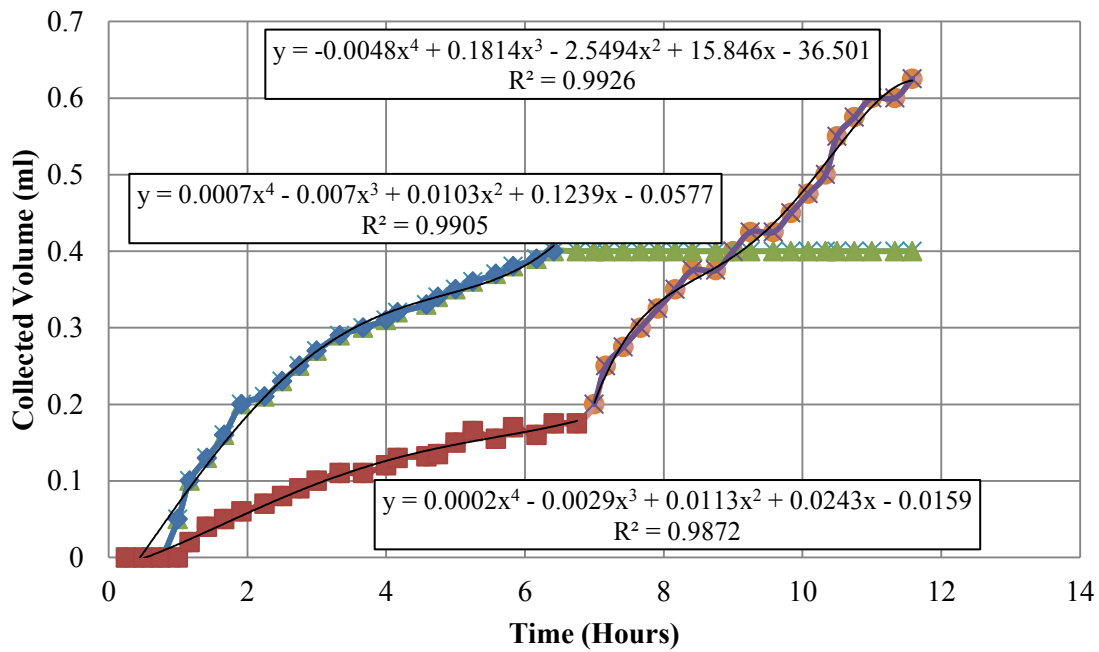


Figure 6.18: Original experimental data of the second waterflood, Bakken Shale (EBS-1).

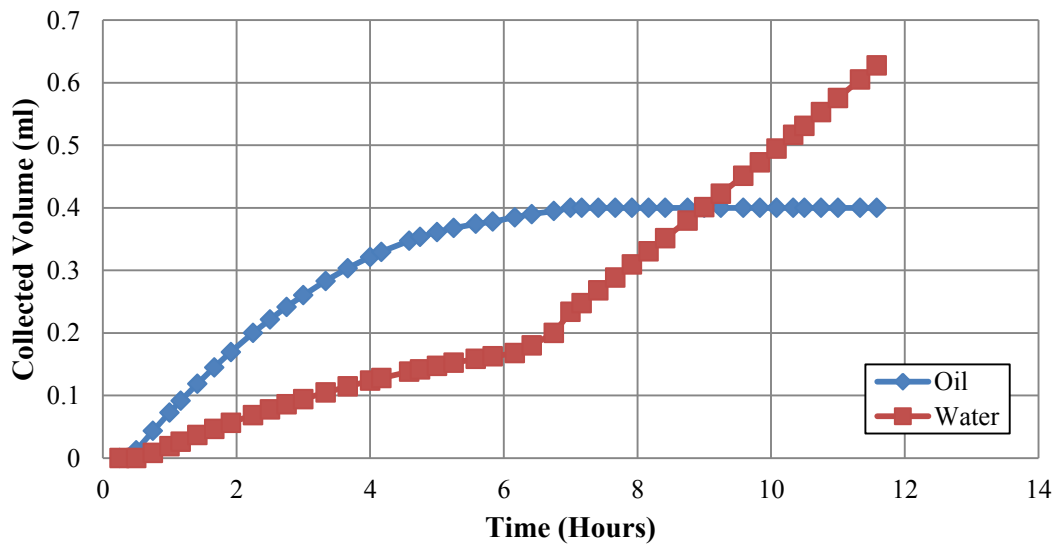


Figure 6.19: Smoothed data of the second water-flood, Bakken Shale (EBS-1).

Table 6.4 shows the in-situ fluid saturation of EBS-1 sample before and after the second water-flooding. Due to the water-flooding, oil saturation decreased from 0.43 to

0.12, and water saturation increased from 0.57 to 0.88. During the second water-flood, more oil was recovered compared to the first water-flood.

Table 6.4: In-situ fluid saturation change of the second water-flood results, Bakken Shale (EBS-1).

Status	Oil Saturation ( $S_o$ )	Water Saturation ( $S_w$ )
Before water-flooding	0.43	0.57
After water-flooding	0.12	0.88
Change	(-) 0.31	(+) 0.31

Using the smoothed experimental results, the relative permeability curves of EBS-1 from the second water-flood were calculated (Figure 6.20). The superficial velocity was 0.0042 m/d. The relative permeability of oil was slightly different during this test, and the relative permeability of water was higher than from the first water-flood results.

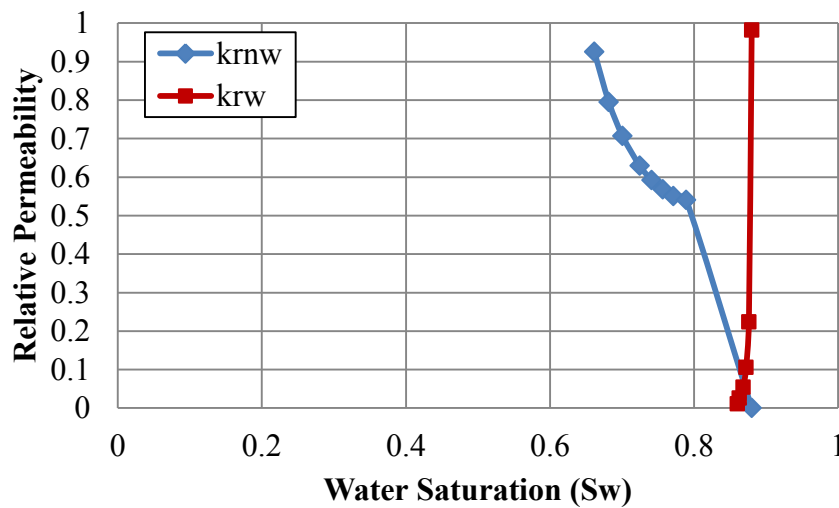


Figure 6.20: Relative permeability curve, second water-flood, Bakken Shale (EBS-1).

### Results for EBS-2 Core

Another Bakken shale sample, EBS-2, was used to measure the relative permeability and to check if the relative permeability test results were reproducible.

Figure 6.21 shows the original experimental results graph of EBS-2 from the first water-flood, and Figure 6.22 shows the smoothed experimental results. These results show a trend that is very similar to results from the first water-flooding of EBS-1.

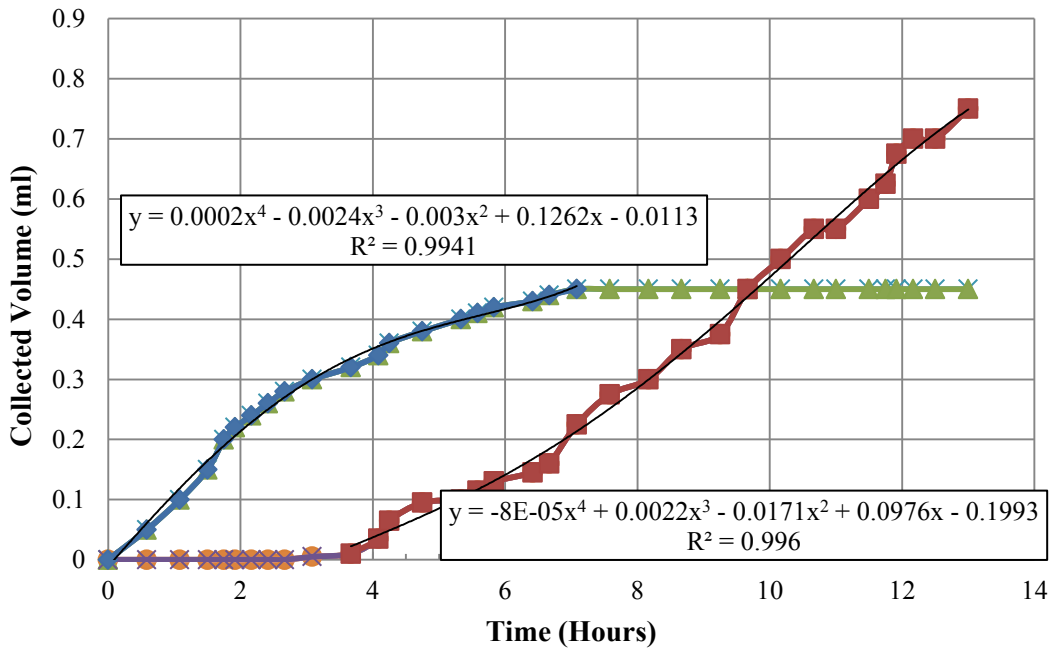


Figure 6.21: Original experimental data of the first water-flood, Bakken Shale (EBS-2).

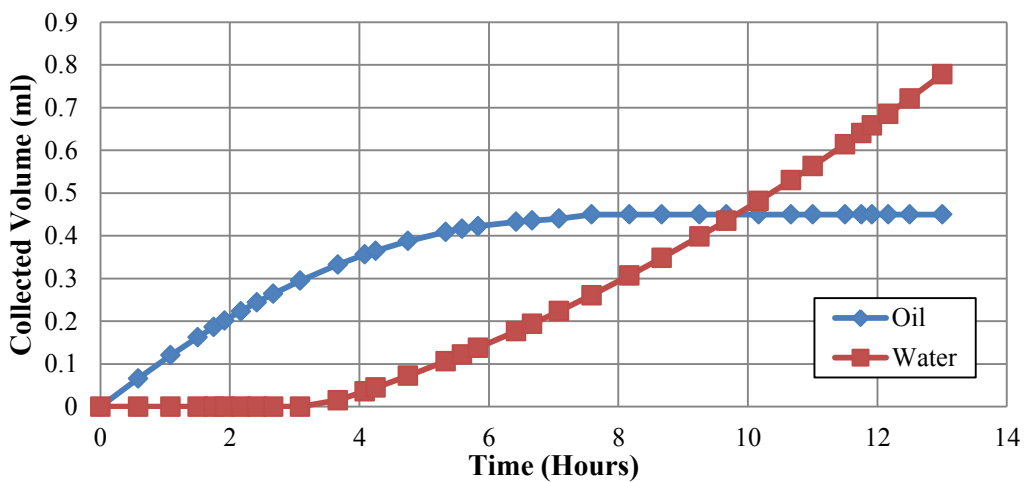


Figure 6.22: Smoothed experimental data of the first water-flood, Bakken Shale (EBS-2).

Table 6.5 shows the in-situ fluid saturation of EBS-2 sample before and after the first water-flooding. Due to the water-flooding, oil saturation was decreased from 0.49 to 0.19, and water saturation was increased from 0.51 to 0.81.

Table 6.5: In-situ fluid saturation change of the first water-flood results, Bakken Shale (EBS-2).

Status	Oil Saturation ( $S_o$ )	Water Saturation ( $S_w$ )
Before water-flooding	0.49	0.51
After water-flooding	0.19	0.81
Change	(-) 0.30	(+) 0.30

Using the above outflow results and NMR measurement, the relative permeability curve of Bakken Shale (EBS-2) at the first water-flooding was calculated (Figure 6.23). The superficial velocity was 0.00448 m/d during this experiment. The results look similar to the results obtained from EBS-1 core floods although the water relative permeability appears to be higher.

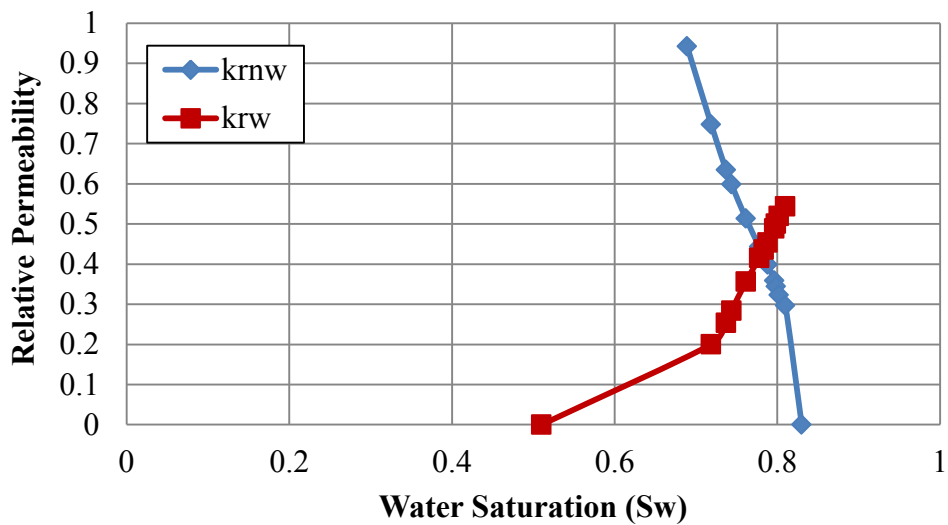


Figure 6.23: Relative permeability curve, first water-flood, Bakken Shale (EBS-2).



A second water-flood with EBS-2 was also performed to see how much difference was generated in the relative permeability. Figure 6.24 shows the outflow analysis result of EBS-2 from the second water-flood. Figure 6.25 shows the smoothed version of the experimental results using the trend line of Figure 6.24.

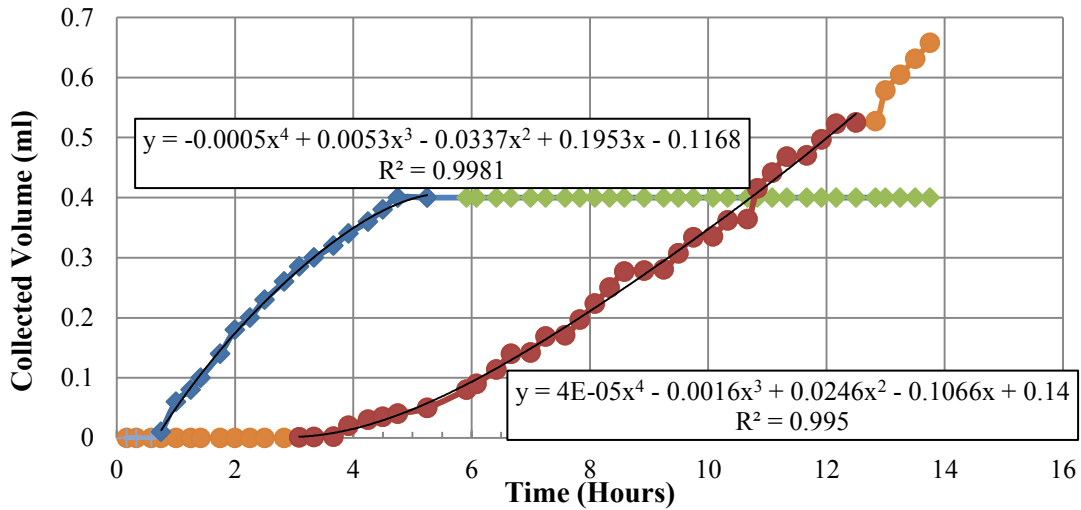


Figure 6.24: Original experimental data of the second water-flood, Bakken Shale (EBS-2).

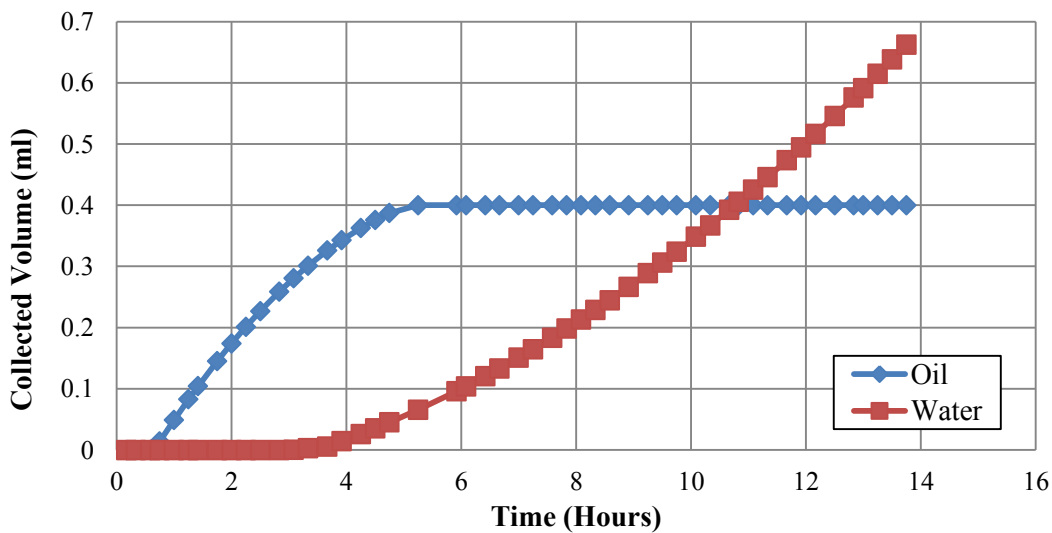


Figure 6.25: Smoothed experimental data of the second water-flood, Bakken Shale (EBS-2).

Table 6.6 shows the in-situ fluid saturation of EBS-2 sample before and after the second water-flood. Due to the water-flood, oil saturation was decreased from 0.49 to 0.19, and water saturation was increased from 0.51 to 0.81.

Table 6.6: In-situ fluid saturation change of the second water-flood results, Bakken Shale (EBS-2).

Status	Oil Saturation ( $S_o$ )	Water Saturation ( $S_w$ )
Before water-flooding	0.49	0.51
After water-flooding	0.19	0.81
Change	(-) 0.30	(+) 0.30

Using the above outflow results and NMR measurements, the relative permeability curve of EBS-2 was calculated for the second water-flood (Figure 6.26). The superficial velocity was 0.0038 m/d this time. The water relative permeability this time is a lot lower. It is not clear why this difference between the first and second waterfloods exists but it is most likely related to the capillary end effect and the inability of the oil to displace the oil during the oil flood between the two waterfloods. This results in a completely different water saturation distribution in the core at the start of the two waterfloods.

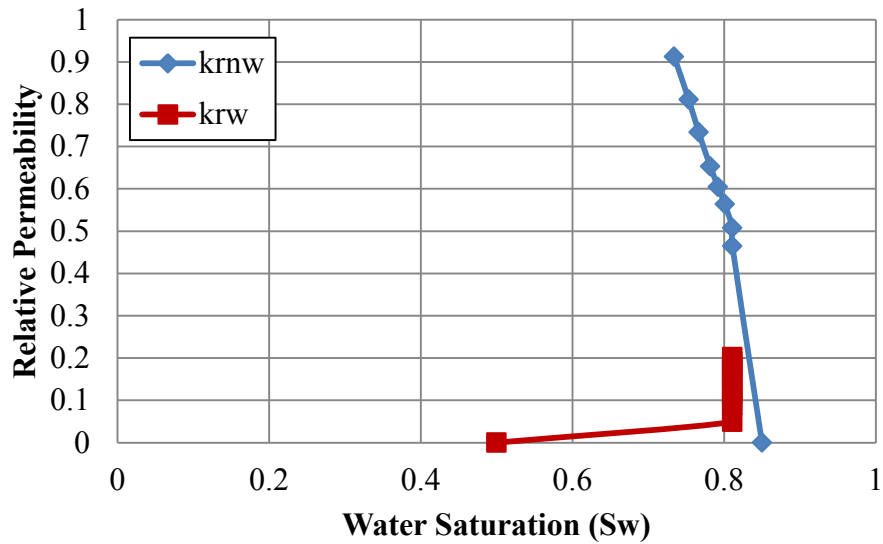


Figure 6.26: Relative permeability curve, second water-flood, Bakken Shale (EBS-2).

## 6.5 CONCLUSIONS AND FUTURE WORK

In this Chapter we present the first reported measurements of the relative permeability of preserved shale samples. An experimental protocol was developed to allow us to perform these challenging measurements. Four unsteady-state displacement tests were performed on Bakken shale samples. Figure 6.27 shows a comparison of the relative permeability results of EBS-1 and EBS-2 samples obtained from the first water-flood. The oil and water relative permeability of both samples show similar values during the whole water saturation range. The crossover point of oil and water relative permeability is around 0.75, and it means those samples are strongly water-wet. In addition, the maximum water relative permeability is lower than the maximum oil relative permeability, and this is also typical for water-wet rock (Jennings, 1957). Figure 6.28 shows a comparison of the relative permeability results for EBS-2 obtained from the first and the second water-floods. The oil relative permeability maintained a similar trend

and values during the experiments, but the relative permeability of the water changed greatly.

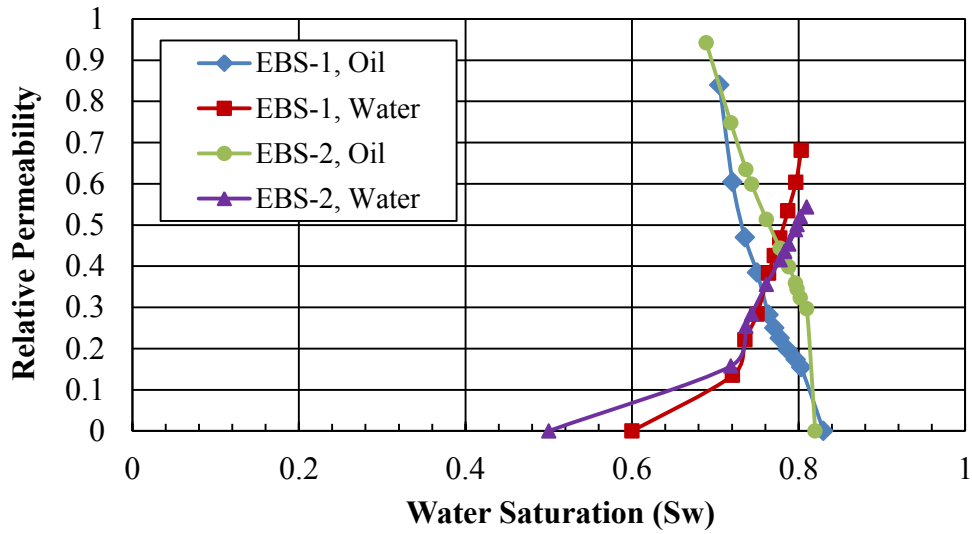


Figure 6.27: Relative permeability curve, first water-flooding, Bakken Shale (EBS-1 and EBS-2).

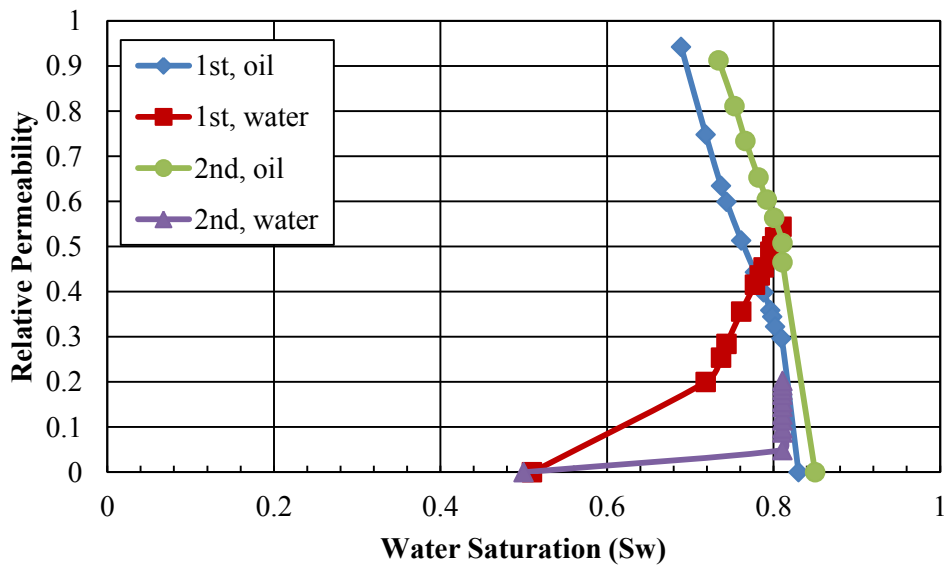


Figure 6.28: Relative permeability curve, 1st and 2nd water-flooding, Bakken Shale (EBS-2).

There are several avenues for future research that this study has opened up. First, the study provides a clear experimental path forward for measuring relative permeabilities for shale samples. Many more measurements need to be done to fully understand multi-phase flow in shales.

It also suggests that there are limitations to this study. Using the unsteady-state method, one of the limitations that is well known to exist is the capillary end effect. In low permeability samples and at low flow rates this effect is particularly important. The following avenues for future research are suggested:

1. A more detailed numerical simulation of the experiments that include the effect of capillary pressure and capillary end effects may provide some better estimates of relative permeability.
2. Conducting a NMR imaging study of the water saturation distribution in the core during the displacement would provide a direct measurement of the in-situ saturation distributions.
3. Measuring and relating capillary pressure curves to the relative permeability curves for shales would be challenging but provide a great deal of insight into multi-phase flow in shales.

## Chapter 7: Conclusions and Future Work

### 7.1 CONCLUSIONS

This study investigates the effect of shale-fluid interaction on shale petrophysical properties, particularly fluid flow properties. The main conclusions of this work are listed below.

1. Large differences in shale properties are observed to occur when measurements on preserved and un-preserved samples are compared. This includes large changes in the following properties: native shale water activity, original fluid content, density, mineralogy, water and nitrogen permeability, swelling, Brinell hardness, and P-wave and S-wave velocities.
2. Therefore, shales should be preserved at the well site and tested in the lab using only preserved samples. A standard lab procedure should be used that ensures minimum alteration of the fluid content of the shale. Failure to follow such standard procedure leads to measurements that do not reflect the “true” or in-situ properties of the shale. Instead, the measurements can be a factor of 2 or 3 different from the “true” value.
3. The pressure penetration technique (PPT) was used to measure shale permeability. The system compressibility and the hold-up volume are measured and used to validate the permeability results from the PPT test with the Darcy flow test. After new values of compressibility and hold-up volume were measured, the permeabilities from PPT and Darcy flow test show good agreement.
4. Simplified slick water which contains friction reducer is compatible with Utica shale. Polyacrylamide, used for friction reduction, reduces the shale permeability by an

order of magnitude. However, this reduction is not permanent, so if there is sufficient brine injection, the permeability recovers.

5. Silica coated nanoparticles added into water-based drilling fluids can significantly reduce water invasion into shales. For proper comparison, brine, base-mud and nanoparticle based muds are tested. A Texas gas shale, Eagle Ford shale, and Barnett shale are investigated to validate this nano-mud system. For all shale types, a large reduction in permeability is observed when a nano-mud is used. Most of tested shale samples have micro-cracks, resulting in very high initial permeability with brine. The nano-mud effectively reduces the permeability of shale samples even when they have micro-cracks in them. The permeability reduction is stable during brine flushing.
6. The mixture of nanoparticles in a base-mud provides the best shale inhibition and is likely to provide the best fluid for wellbore stability during drilling. The use of pure nanoparticle suspensions, without base-mud is not enough to block micro-cracks and other big pores. The base mud is an essential part of the formulation to prevent the water invasion.
7. Relative permeability measurements for a shale sample under confining pressure are reported for the first time.
8. A non-destructive experimental procedure has been devised to quantitatively measure water and oil saturations in cores using NMR methods.
9. A confining pressure (RPC) set-up is developed to measure relative permeability of preserved shale samples for the first time.
10. Four unsteady-state displacement tests are performed on Bakken shale samples using the RPC set-up, and relative permeability curves are reported. These curves indicate that the Bakken cores are water-wet. The crossover point of oil and water relative

permeability is around 0.75, and the maximum water relative permeability is lower than the maximum oil relative permeability.

11. The relative permeability curves obtained from two different cores are quite repeatable when the data from the first water-flood are used.
12. Repeating the water-flood on the same core after an oil flood does not provide repeatable results. This is most likely due to capillary end effects and the incomplete displacement of water by the oil flood between the two water-floods. This results in a different initial water saturation distribution in the core.
13. Based on the studies performed here, mineralogy or total clay percentage did not correlate with flow properties or fluid sensitivity. The mineralogy data may be meaningful when combined with other properties.

## **7.2 RECOMMENDATIONS FOR FUTURE WORK**

Based on observations in this study, the following recommendations are suggested for future research.

1. From the study of preservation effect on the physical properties, the importance of using preserved samples is evident. However, preserved shales are very precious and it is hard to get them in many cases. Due to the reason, many laboratories currently use outcrop samples or unpreserved samples. Methods need to be investigated to reduce the amount of core needed for conducting different lab measurements.
2. For the slick water study, only the permeability change of shales is solely studied among the various petrophysical properties. For the future work, proppant embedment, hardness change, rock corrosion, fine migration, capillary suction time



and directional swelling need to be studied. These characteristics would be very helpful to understand the interaction between fracturing fluid and organic rich shale.

3. Only one friction reducer, Polyacrylamide (DR7000), is tested in this fracturing fluid study. Many fracturing fluid additive such as clay stabilizers, cross-linked gels, and polymers and their effects on shale properties should be studied. Moreover, the effect on flow properties would also be changed if a new shale type is introduced. Other than Utica shale, Eagle Ford and Bakken shale would show different range of impact due to the slick water injection.
4. Nanoparticle based muds which act by physical plugging of pore throats are shown to be an effective shale inhibitor. There are various shale inhibitors and clay stabilizers such as ionic liquids, inorganic salts and cationic polymers that can also be evaluated. For example, inorganic salts prevent the interaction between shale and drilling fluid. More comparisons of the effectiveness of nano-muds versus other shale inhibitors are needed.
5. Nano-muds have been tested with a PPT set-up which does not have the capability of applying a confining pressure. The initial permeability with brine is very high for most of the samples due to micro-cracks. If these samples are tested under confining stress, the micro cracks can be closed and a more reliable matrix permeability can be obtained. These measurements can also be performed at reservoir conditions.
6. The relative permeability measurements on the Bakken shale cores offers hope that such measurements can be performed on other shale formations.
7. A more detailed numerical simulation of the experiments that include the effect of capillary pressure and capillary end effects may provide better estimates of relative permeability.

8. Conducting a NMR imaging study of the water saturation distribution in the core during the displacement would provide a direct measurement of the in-situ saturation distributions.
9. Measuring and relating capillary pressure curves to the relative permeability curves for shales would be challenging but provide a great deal of insight into multi-phase flow in shales.

## References

- Abrams, A. (1977, May 1). Mud Design To Minimize Rock Impairment Due To Particle Invasion. Society of Petroleum Engineers. doi:10.2118/5713-PA
- Aften, C.W. and Gabel, R.K. (1994, August 30th) Clay stabilizer. US Patent 5 342 530.
- Al-Bazali, T. M., Zhang, J., Chenevert, M. E., & Sharma, M. M. (2006, January 1). Factors Controlling the Membrane Efficiency of Shales when Interacting with Water-Based and Oil-Based Muds. SPE-100735-MS presented at International Oil & Gas Conference and Exhibition in China, 5-7 December, Beijing, China. doi:10.2118/100735-MS
- Auerbach, S.M. (2007) Handbook of Layered Materials, reprint from 2004 Edition. CRC Press, Boca Raton.
- Aviles-Alcantara, C., Guzman C., C., & Rodriguez M., A. (2000, January 1). Characterization and Synthesis of Synthetic Drilling Fluid Shale Stabilizer. SPE-59050-MS presented at SPE International Petroleum Conference and Exhibition in Mexico, 1-3 February, Villahermosa, Mexico. doi:10.2118/59050-MS
- Baker Hughes Incorporated. (2010). Wax Encapsulation Core Preservation Services, <http://www.bakerhughes.com/news-and-media/resources/brochures/wax-encapsulation-product-overview> (accessed 17 June 2013)
- Bol, G. M., Wong, S.-W., Davidson, C. J., & Woodland, D. C. (1994, June 1). Borehole Stability in Shales. Society of Petroleum Engineers. doi:10.2118/24975-PA
- Blachier, C., Michot, L., Bihannic, I., Barr`es, O., Jacquet, A., Mosquet, M. (2009) Adsorption of polyamine on clay minerals. *J. Colloid Interface Sci.* 336 (2), 599–606.
- Branch, H.I. (1988, January 12th) Shale-stabilizing drilling fluids and method for producing same. US Patent 4719 021.
- Breeden, D., Shipman, J. (2004, April 6-7). Shale Analysis for Mud Engineers. AADE-04-DF-HO-30 presented at the AADE 2004 Drilling Fluids Conference in Houston, Texas
- Browning, J., Ikonnikova, S., Gülen, G., & Tinker, S. (2013, July 1). Barnett Shale Production Outlook. Society of Petroleum Engineers. doi:10.2118/165585-PA
- Bumb, A. C., & McKee, C. R. (1988, March 1). Gas-Well Testing in the Presence of Desorption for Coalbed Methane and Devonian Shale. Society of Petroleum Engineers. doi:10.2118/15227-PA

- Cai, J., Chenevert, M. E., Sharma, M. M., & Friedheim, J. E. (2012, March 1). Decreasing Water Invasion Into Atoka Shale Using Nonmodified Silica Nanoparticles. Society of Petroleum Engineers. doi:10.2118/146979-PA
- Cao Minh, C., Crary, S. F., Zielinski, L., Liu, C., Jones, S., & Jacobsen, S. J. (2012, January 1). 2D-NMR Applications in Unconventional Reservoirs. SPE-161578-MS presented at SPE Canadian Unconventional Resources Conference, 30 October-1 November, Calgary, Alberta, Canada. doi:10.2118/161578-MS
- Chenevert, M. E. (1989, January 1). Lecture: Diffusion of Water And Ions Into Shales. International Society for Rock Mechanics.
- Chenevert, M. E., & Osisanya, S. O. (1989, September 1). Shale/Mud Inhibition Defined With Rig-Site Methods. Society of Petroleum Engineers. doi:10.2118/16054-PA
- Chenevert, M. E., & Amanullah, M. (2001, September 1). Shale Preservation and Testing Techniques for Borehole-Stability Studies. Society of Petroleum Engineers. doi:10.2118/73191-PA
- Civan, F., Rai, C. S., & Sondergeld, C. H. (2012, September 1). Determining Shale Permeability to Gas by Simultaneous Analysis of Various Pressure Tests. Society of Petroleum Engineers. doi:10.2118/144253-PA
- Craig, F.F. (1971) The Reservoir Engineering Aspects of Waterflooding, Monograph Series, SPE, Richardson, TX Vol. 3
- Crawshaw, J.P., Way, P.W., Thiercelin, M. (2002, January 9th) A method of stabilizing a wellbore wall. GB Patent 2 363 810, assigned to Sofitech NV.
- Coulombe, M. (2007, June 14th) Healing Clay, Research Matters, ASU Knowledge Enterprise Development. <https://researchmatters.asu.edu/stories/healing-clay-906>
- El-Khatib, N. (2013, April 15). New Approach for Pulse Test Analysis. SPE-164597-MS presented at North Africa Technical Conference and Exhibition, 15-17 April, Cairo, Egypt. doi:10.2118/164597-MS
- Ely, J. W., Fowler, S. L., Tiner, R. L., Aro, D. J., Sicard, Jr., G. R., & Sigman, T. A. (2014, October 27). "Slick Water Fracturing and Small Proppant" The future of stimulation or a slippery slope? SPE-170784-MS presented at SPE Annual Technical Conference and Exhibition, 27-29 October, Amsterdam, The Netherlands. doi:10.2118/170784-MS
- Fink, J. (2011, June 9) Petroleum Engineer's Guide to Oil Field Chemicals and Fluids. Gulf Professional Publishing. doi: 10.1016/B978-0-12-383844-5.00003-9
- Fischer, G.J., and Paterson, M.S. (1992) Measurement of Permeability and Storage Capacity in Rocks during Deformation at High Temperature and Pressure. Fault Mechanics and Transport Properties of Rocks. 51, 213-252.

- Gips, J., Daigle, H., & Sharma, M. (2014, August 28). Characterization of Free and Bound Fluids in Hydrocarbon Bearing Shales Using NMR and Py-GC-MS. Society of Petroleum Engineers. doi:10.15530/urtec-2014-1917686
- Goda, H. M., & Behrenbruch, P. (2004, January 1). Using a Modified Brooks-Corey Model to Study Oil-Water Relative Permeability for Diverse Pore Structures. SPE-88538-MS presented at SPE Asia Pacific Oil and Gas Conference and Exhibition, 18-20 October, Perth, Australia. doi:10.2118/88538-MS
- Halliday, W.S., Thielen, V.M (1987, May 12th) Drilling mud additive. US Patent 4 664 818, assigned to Newpark Drilling Fluid Inc.
- Hale, A.H. and van Oort, E. (1997, February 11) Efficiency of ethoxylated/propoxylated polyols with other additives to remove water from shale. US Patent 5602082.
- Hoffmann, R., Lipscomb, W.N. (1962) Theory of polyhedral molecules. i. physical factorizations of the secular equation. *J. Chem. Phys.* 36 (8), 2179–2189
- Honarpour, M., Koederitz, L.F., and Harvey, A.H. (1986) Relative Permeability of Petroleum Reservoirs, CRC Press Inc., Boca Raton, FL
- Honarpour, M., Koederitz, L. F., & Harvey, A. H. (1982, December 1). Empirical Equations for Estimating Two-Phase Relative Permeability in Consolidated Rock. Society of Petroleum Engineers. doi:10.2118/9966-PA
- Honarpour, M., & Mahmood, S. M. (1988, August 1). Relative-Permeability Measurements: An Overview. Society of Petroleum Engineers. doi:10.2118/18565-PA
- Jennings, H.Y. Jr. (1957, March). Surface Properties of Natural and Synthetic Porous Media. *Prod. Monthly* 21, No. 5, 20-24
- Ji, L., Guo, Q., Friedheim, J. E., Zhang, R., Chenevert, M. E., & Sharma, M. M. (2012, January 1). Laboratory Evaluation and Analysis of Physical Shale Inhibition of an Innovative Water-Based Drilling Fluid with Nanoparticles for Drilling Unconventional Shales. SPE-158895-MS presented at SPE Asia Pacific Oil and Gas Conference and Exhibition, 22-24 October, Perth, Australia. doi:10.2118/158895-MS
- Johnson, E. F., Bossler, D. P., & Bossler, V. O. N. (1959, January 1). Calculation of Relative Permeability from Displacement Experiments. SPE-1023-G. *Petroleum Transactions, AIME*, Vol. 216, 370-372.
- Jones, S.C. (1997) A Technique for Faster Pulse-Decay Permeability Measurements in Tight Rocks. *SPEREE* 12, 19-25
- Jones, S. C., & Roszelle, W. O. (1978, May 1). Graphical Techniques for Determining Relative Permeability From Displacement Experiments. Society of Petroleum Engineers. doi:10.2118/6045-PA

- Jung, C. M., Zhou, J., Chenevert, M. E., & Sharma, M. M. (2013, September 30). The Impact of Shale Preservation on the Petrophysical Properties of Organic-Rich Shales. SPE-166419-MS presented at SPE Annual Technical Conference and Exhibition, 30 September-2 October, New Orleans, Louisiana, USA. doi:10.2118/166419-MS
- Jung, C. M., Zhang, R., Chenevert, M., & Sharma, M. (2013, August 12). High-Performance Water-Based Mud Using Nanoparticles for Shale Reservoirs. SPE-168799-MS presented at Unconventional Resources Technology Conference, 12-14 August, Denver, Colorado, USA. doi:10.1190/URTEC2013-106
- Kamel, A. H. A., & Shah, S. N. (2009, January 1). Investigation of Flow Behavior of Slick-Water in Large Straight and Coiled Tubing. SPE-118949-MS presented at SPE Hydraulic Fracturing Technology Conference, 19-21 January, The Woodlands, Texas. doi:10.2118/118949-MS
- Khodjaa, M., Canselierb, J.P., Bergayac, F., Fourard, K., Khodjae, M., Cohautc, N. and Benmounahd, A. (2010, August). Shale problems and water-based drilling fluid optimisation in the Hassi Messaoud Algerian oil field. *Applied Clay Science*. 49, 4, 383–393. doi:10.1016/j.clay.2010.06.008
- Kubena Jr., E., Whitebay, L.E., Wingrave, J.A. (1993 May 18) Method for stabilizing boreholes. US Patent 5 211 250, assigned to Conoco Inc.
- Kumar, V., Sondergeld, C. H., & Rai, C. S. (2012, January 1). Nano to Macro Mechanical Characterization of Shale. SPE-159804-MS presented at SPE Annual Technical Conference and Exhibition, 8-10 October, San Antonio, Texas, USA. doi:10.2118/159804-MS
- Lewis, R., Singer, P., Jiang, T., Rylander, E., Sinclair, S., & Mclin, R. H. (2013, April 10). NMR T2 Distributions in the Eagle Ford Shale: Reflections on Pore Size. SPE-164554-MS presented at SPE Unconventional Resources Conference-USA, 10-12 April, The Woodlands, Texas, USA. doi:10.2118/164554-MS
- Luffel, D. L., Hopkins, C. W., & Schettler, P. D. (1993, January 1). Matrix Permeability Measurement of Gas Productive Shales. SPE-26633-MS presented at SPE Annual Technical Conference and Exhibition, 3-6 October, Houston, Texas. doi:10.2118/26633-MS
- Lal, M. (1999, January 1). Shale Stability: Drilling Fluid Interaction and Shale Strength. SPE-54356-MS presented at SPE Asia Pacific Oil and Gas Conference and Exhibition, 20-22 April, Jakarta, Indonesia. doi:10.2118/54356-MS
- Mooney, R.W., Keenan, A.G., Wood, L.A. (1952) Adsorption of water vapor by montmorillonite. II. Effect of exchangeable ions and lattice swelling as measured by X-ray diffraction. *J. Am. Chem. Soc.* 74 (6), 1371–1374.

- Montgomery, C. (2013, May 20). Fracturing Fluids. ISRM-ICHF-2013-035 presented at ISRM International Conference for Effective and Sustainable Hydraulic Fracturing, 20-22 May, Brisbane, Australia. doi:10.5772/56192
- Murray, H.H. (2007) Applied Clay Mineralogy: Occurrences, Processing, and Application of Kaolins, Bentonites, Palygorskite-Sepiolite, and Common Clays, Vol. 2. Elsevier, Amsterdam.
- Oleas, A. M., Osuji, C. E., Chenevert, M. E., & Sharma, M. M. (2010, March 1). Entrance Pressure of Oil-Based Mud Into Shale: Effect of Shale, Water Activity, and Mud Properties. Society of Petroleum Engineers. doi:10.2118/116364-PA
- Passey, Q. R., Bohacs, K., Esch, W. L., Klimentidis, R., & Sinha, S. (2010, January 1). From Oil-Prone Source Rock to Gas-Producing Shale Reservoir - Geologic and Petrophysical Characterization of Unconventional Shale Gas Reservoirs. SPE-131350-MS presented at International Oil and Gas Conference and Exhibition in China, 8-10 June, Beijing, China. doi:10.2118/131350-MS
- Patel, A.D., Stamatakis, E., Davis, E., Friedheim, J., (2007, July 31st) High performance water based drilling fluids and method of use. US Patent 7 250 390, assigned to M-I L.L.C. (Houston, TX)
- Patel, A.D., McLaurine, H.C. (1993, October 11) Drilling fluid additive and method for inhibiting hydration. CA Patent 2 088 344, assigned to M I Drilling Fluids Co.
- Peters, E. J. (2012, May 15). Advanced Petrophysics: Volume 2: Dispersion, Interfacial Phenomena/Wettability, Capillarity/Capillary Pressure, Relative Permeability. Live Oak Book Company, ISBN-10: 1936909464
- Peters, E. J., & Khataniar, S. (1987, December 1). The Effect of Instability on Relative Permeability Curves Obtained by the Dynamic-Displacement Method. Society of Petroleum Engineers. doi:10.2118/14713-PA
- Raza, S.H., Treiber, L.E., and Archer, D.L. (1968, April) Wettability of Reservoir Rocks and Its Evaluation. Prod. Monthly. 32, 4, 2-7
- Rudd, N. (1966, January 1). Pressure Decay Measurement. SPE-1604-MS presented at Fall Meeting of the Society of Petroleum Engineers of AIME, 2-5 October, Dallas. Texas. doi:10.2118/1604-MS
- Schenk, C., Pierce, B., and Demas, A., USGS Releases First Assessment of Shale Gas Resources in the Utica Shale: 38 trillion cubic feet, (2012, October, 4) [http://www.usgs.gov/newsroom/article.asp?ID=3419&from=rss\\_home#.VP-zBvnF80m](http://www.usgs.gov/newsroom/article.asp?ID=3419&from=rss_home#.VP-zBvnF80m), Accessed 2015
- Sensoy, T., Chenevert, M. E., & Sharma, M. M. (2009, January 1). Minimizing Water Invasion in Shales Using Nanoparticles. SPE-124429-MS presented at SPE Annual Technical Conference and Exhibition, 4-7 October, New Orleans, Louisiana. doi:10.2118/124429-MS

- Sharma, M. M., Chenevert, M. E., Guo, Q., Ji, L., Friedheim, J., & Zhang, R. (2012, January 1). A New Family of Nanoparticle Based Drilling Fluids. SPE-160045-MS presented at SPE Annual Technical Conference and Exhibition, 8-10 October, San Antonio, Texas, USA. doi:10.2118/160045-MS
- Sharma, M. M., Gadde, P. B., Sullivan, R., Sigal, R., Fielder, R., Copeland, D., Griffin, L., and Weijers, L. (2004, January 1). Slick Water and Hybrid Fracs in the Bossier: Some Lessons Learnt. SPE-89876-MS presented at SPE Annual Technical Conference and Exhibition, 26-29 September, Houston, Texas. doi:10.2118/89876-MS
- Shebl, M. A., Nyaaba, C., & Yalavarthi, R. (2013, March 26). Role of Detailed Reservoir Characterization and Lateral Placement on Well Performance in the Marcellus Shale Gas Reservoir. IPTC-16718-MS presented at International Petroleum Technology Conference, 26-28 March, Beijing, China. doi:10.2523/IPTC-16718-MS
- Sinha, S., Braun, E. M., Passey, Q. R., Leonardi, S. A., Wood, A. C., Zirkle, T., Boros, J.A., & Kudva, R. A. (2012, January 1). Advances in Measurement Standards and Flow Properties Measurements for Tight Rocks such as Shales. SPE-152257-MS presented at SPE/EAGE European Unconventional Resources Conference and Exhibition, 20-22 March, Vienna, Austria. doi:10.2118/152257-MS
- Simpson, J. P. (1979, May 1). A New Approach to Oil-Base Muds for Lower-Cost Drilling. Society of Petroleum Engineers. doi:10.2118/7500-PA
- Smith, C.K. and Balson, T.G. (2000, February 23rd) Shale-stabilizing additives. GB Patent 2 340 521, assigned to Sofitech NV and Dow Chemical Co.
- Steiger, R. P., & Leung, P. K. (1992, September 1). Quantitative Determination of the Mechanical Properties of Shales. Society of Petroleum Engineers. doi:10.2118/18024-PA
- Stowe, C., Bland, R.G., Clapper, D., Xiang, T., Benaissa, S. (2002, January 2nd) Water-based drilling fluids using latex additives. GB Patent 2 363 622, assigned to Baker Hughes Inc.
- Suri, A., & Sharma, M. M. (2001, January 1). Strategies for Sizing Particles in Drilling and Completion Fluids. SPE-68964-MS presented at SPE European Formation Damage Conference, 21-22 May, The Hague, Netherlands. doi:10.2118/68964-MS
- Texas Railroad Commission Production Data Query System (PDQ) (2015, February 20). [http://www.rrc.state.tx.us/media/22204/barnettshale\\_totalnaturalgas\\_day.pdf](http://www.rrc.state.tx.us/media/22204/barnettshale_totalnaturalgas_day.pdf), Accessed 2015



- Texas Railroad Commission Production Data Query System (PDQ) (2015, February 20). [http://www.rrc.state.tx.us/media/22205/barnettshale\\_oil\\_bblperday.pdf](http://www.rrc.state.tx.us/media/22205/barnettshale_oil_bblperday.pdf), Accessed 2015
- Tian, Y., Ayers, W. B., & McCain, W. D. (2013, March 26). The Eagle Ford Shale Play, South Texas: Regional Variations in Fluid Types, Hydrocarbon Production and Reservoir Properties. IPTC-16808-MS presented at International Petroleum Technology Conference , 26-28 March, Beijing, China. doi:10.2523/IPTC-16808-MS
- US Energy Information Administration, Shale Gas Glossary, [http://www.energy.gov/sites/prod/files/2013/04/f0/shale\\_gas\\_glossary.pdf](http://www.energy.gov/sites/prod/files/2013/04/f0/shale_gas_glossary.pdf), Accessed 2015
- US Energy Information Administration, Barnett shale, Ft. Worth Basin, Texas, Wells by Year of First Production and Orientation, [http://www.eia.gov/oil\\_gas/rpd/shaleusa1.pdf](http://www.eia.gov/oil_gas/rpd/shaleusa1.pdf)
- US Energy Information Administration, Today in Energy, Shale oil and shale gas resources are globally abundant (2014, January 2). <http://www.eia.gov/todayinenergy/detail.cfm?id=14431>, Accessed 2015
- US Energy Information Administration, Updates to the EIA Eagle Ford Play Maps (2014, December)<http://www.eia.gov/maps/pdf/EIA%20Eagle%20Ford%20Play%20update%2012-29-14.pdf>, Accessed 2015
- US Energy Information Administration, Review of Emerging Resources: U.S. Shale Gas and Shale Oil Plays (2011, July) <http://www.eia.gov/analysis/studies/usshalegas/pdf/usshaleplays.pdf>, Accessed 2015
- van Spronsen, E. (1982, January 1). Three-Phase Relative Permeability Measurements Using the Centrifuge Method. SPE-10688-MS presented at SPE Enhanced Oil Recovery Symposium, 4-7 April, Tulsa, Oklahoma. doi:10.2118/10688-MS
- van Oort, E. (2003, June). On the physical and chemical stability of shales. *J. Petr. Sci. Eng.* 38, 213–235. doi:10.1016/S0920-4105(03)00034-2
- Wasaki, A., & Akkutlu, I. Y. (2014, October 27). Permeability of Organic-rich Shale. Society of Petroleum Engineers. SPE-170830-MS presented at SPE Annual Technical Conference and Exhibition, 27-29 October, Amsterdam, The Netherlands. doi:10.2118/170830-MS
- Westerkamp, A., Wegner, C., Mueller, H.P. (1991, October 16th). Borehole treatment fluids with clay swelling inhibiting properties (ii) (bohrloch-behandlungsfluessigkeiten mit tonquellungsinhibierenden eigenschaften (ii)). EP Patent 451 586, assigned to Bayer AG.

- Weaver, J. D., Nguyen, P. D., & Loghry, R. (2011, January 1). Stabilizing Fracture Faces in Water-Sensitive Shale Formations. SPE-149218-MS presented at SPE Eastern Regional Meeting, 17-19 August, Columbus, Ohio, USA. doi:10.2118/149218-MS
- Winston, P.W. and Bates, D.H. (1960, January). Saturated Solutions for the Control of Humidity in Biological Research, Ecology. Vol: 41, No. 1, p. 232-237. doi:10.2307/1931961
- Wilson, M.J. and Wilson, L. (2014, April). Clay mineralogy and shale instability: an alternative conceptual analysis, Clay Minerals, Vol: 49, No. 2, p. 127-145. doi:10.1180/claymin.2014.049.2.01
- Welge, H. J. (1952, April 1). A Simplified Method for Computing Oil Recovery by Gas or Water Drive. Journal of Petroleum Technology. Vol 4. Issue 4 doi:10.2118/124-G
- Wong, R. C. K. (2001, December 1). Analysis of Swelling and Softening of Shale (Colorado Group) Near a Drilled Hole Subjected to Water Invasion. Petroleum Society of Canada. doi:10.2118/01-12-03
- Zaitoun, A., Berton, N. (1990, February) Stabilization of montmorillonite clay in porous media by highmolecular-weight polymers. In: Proceedings Volume, 9th SPE Formation Damage Contr. Symp. 155–164.
- Zhou, J., Jung, C. M., Chenevert, M. E., & Sharma, M. M. (2013, January 1). Petrophysical Characterization of Organic-Rich Shales: A New Standardized Protocol. ARMA-2013-546 presented at 47th U.S. Rock Mechanics/Geomechanics Symposium, 23-26 June, San Francisco, California.
- Zhang, J., Chenevert, M. E., AL-Bazali, T., & Sharma, M. M. (2004, January 1). A New Gravimetric - Swelling Test for Evaluating Water and Ion Uptake in Shales. Society of Petroleum Engineers. SPE-89831-MS presented at SPE Annual Technical Conference and Exhibition, 26-29 September, Houston, Texas. doi:10.2118/89831-MS